Georgia State University
ScholarWorks @ Georgia State University

Chemistry Dissertations | Department of Chemistry

12-10-2018

Characterizing the Optical and Electrochemical Properties of Monolayer-Protected Noble Metal Nanoclusters

Jonathan W. Padelford

Follow this and additional works at: https://scholarworks.gsu.edu/chemistry_diss

Recommended Citation

Padelford, Jonathan W., "Characterizing the Optical and Electrochemical Properties of Monolayer-Protected Noble Metal Nanoclusters." Dissertation, Georgia State University, 2018.
https://scholarworks.gsu.edu/chemistry_diss/157

This Dissertation is brought to you for free and open access by the Department of Chemistry at ScholarWorks @ Georgia State University. It has been accepted for inclusion in Chemistry Dissertations by an authorized administrator of ScholarWorks @ Georgia State University. For more information, please contact scholarworks@gsu.edu.

CHARACTERIZING THE OPTICAL AND ELECTROCHEMICAL PROPERTIES OF MONOLAYER-PROTECTED NOBLE METAL NANOCLUSTERS

by

JONATHAN PADELFORD

Under the Direction of Gangli Wang, PhD

ABSTRACT

Gold, silver, and other nanoclusters protected by a monolayer of monothiolate or dithiolate ligand can be synthesized into a variety of compositions and core structures depending on the type of ligand used and reaction conditions. Unique size or composition dependent physicochemical properties emerge ranging from being molecular-like to plasmonic toward bulk metal. This dissertation focuses on the characterization of optical and electrochemical and other related properties of newly synthesized and previously established Au and Ag nanoclusters. Chapter one provides an overview of the gold and silver nanoclusters including both fundamentals and applications. In chapter two, phase transfer strategy is adopted to overcome the restraints of using water as an electrochemical solvent. Redox activities in a much wider potential were resolved for newly synthesized aqueous soluble Au nanoclusters stabilized by mercaptosuccinic acid and lipoic acid (LA) and the previously reported $Au_{22}LA_{12.}$ In chapter three, spectroelectrochemistry analysis reveals unprecedented details in electronic transitions from the Au_{130}(p-MBT)$_{50}$ nanoclusters (sample obtained through the collaboration with Jin's group). An energy diagram is proposed from the combined optical and electrochemical

characterizations in reference to the ultrafast spectroscopy results. Together with the Au_{130} stabilized by a mixed mono- and di-thiolate ligand monolayer reported earlier by our group, a significant conclusion is reached that up to Au_{130}, a clear energy band gap remains corresponding to molecular energetics. Full transition to metallic will likely occur at larger sizes with appropriate lattice structures. In chapter four, a new silver nanocluster is synthesized with the lipoic acid as its protecting ligands. Optical, electrochemical, and other features were studied to characterize this new cluster. Intense absorbance features along with high but unstable luminescence were observed. Like its gold counterparts, ligand oxidation was observed by FTIR. Further mass spectrometry data is needed to propose a molecular composition.

INDEX WORDS: Au nanoclusters, monolayer-protected clusters (MPC), Electrochemistry, Near-Infrared luminescence, Phase Transfer, Electronic Transitions, Spectroelectrochemistry, Ag nanoclusters

CHARACTERIZING THE OPTICAL AND ELECTROCHEMICAL PROPERTIES OF MONOLAYER-PROTECTED NOBLE METAL NANOCLUSTERS

by

JONATHAN PADELFORD

A Dissertation Submitted in Partial Fulfillment of the Requirements for the Degree of

Doctor of Philosophy

in the College of Arts and Sciences

Georgia State University

2018

Copyright by
Jonathan Padelford
2018

CHARACTERIZING THE OPTICAL AND ELECTROCHEMICAL PROPERTIES OF MONOLAYER-PROTECTED NOBLE METAL NANOCLUSTERS

by

JONATHAN PADELFORD

Committee Chair: Gangli Wang

Committee: Markus Germann

Ning Fang

Siming Wang

Electronic Version Approved:

Office of Graduate Studies

College of Arts and Sciences

Georgia State University

December 2018

DEDICATION

I want to dedicate this dissertation to my wife (Michelle Padelford) and my parents (Jennifer Padelford and Donald Padelford). Without their love and support none of this would have been possible.

ACKNOWLEDGEMENTS

All the work was done under the guidance and support of Dr. Gangli Wang. His motivating support along with his many valuable suggestions along the way were highly beneficial to not just my research but life as a whole.

The committee members of my dissertation Professor Markus W. Germann, Professor Ning Fang, and Dr. Siming Wang are gratefully acknowledged.

I would like to thank the various staff in the Department of Chemistry, especially Dr. Zhenming Du for his help anytime I had questions regarding NMR.

Thanks, are also given to current and past members (Dr. Tarushee Ahuja, Dr. Tanyu Wang, Dr. Jie Jiang, Cecil V. Conroy, Maksim Kvetney, Warren Brown, Yan Li, Dengchao Wang, Michael Bowen, Hedi Ma, and Minh Tri Hoang Tran) in Dr. Gangli Wang's Group. Thank you for all your support throughout my time here. It was a joy working with everyone.

I acknowledge the fellowship (2015-2018) for the Brains and Behavior for supporting me through my time at Georgia State.

The financial support or my research which includes Gangli Wang startup at GSU, and National Science Foundation funding (CHE-1059022) are gratefully acknowledged.

TABLE OF CONTENTS

LIST OF TABLES

LIST OF FIGURES

LIST OF ABBREVIATIONS

Au NPs	Gold Nanoparticles
Au MPCs	Gold Monolayer-Protected Clusters
Au NCs	Gold Nanoclusters
Ag NPs	Silver Particles
Ag MPCs	Silver Monolayer-Protected Clusters
Ag NCs	Silver Nanoclusters
UV-Vis	Ultraviolet-Visible
CV	Cyclic Voltammetry
SWV	Square Wave Voltammetry
DPV	Differential Pulse Voltammetry
FT-IR	Fourier-Transform Infrared Spectroscopy
HOMO	Highest Occupied Molecular Orbital
LUMO	Lowest Unoccupied Molecular Orbital
MSA	Mercaptosuccinic Acid
LA	Lipoic Acid
TOABr	Tetraoctylammonium Bromide
TBAP	Tetrabutylammonium Perchlorate
$NaCLO_4$	Sodium Perchlorate
ACN	Acetonitrile
MWCO	Molecular Weight Cutoff
p-MBT	4-Methylbenzenethiolate
MALDI-TOF	Matrix-Assisted Laser Desorption Ionization-Time of Flight

NMR	Nuclear Magnetic Resonance
^{1}H	Proton NMR
QDL	Quantized Double-Layer Charging
DAPI	4’,6-diamidino-2-phenylindole

1 INTRODUCTION

1.1 Au NCs: Synthesis and General Characteristics

Noble metal nanoclusters, or interchangeably clusters or monolayer-protected clusters, protected by a ligand monolayer have grown to great importance over the last few decades. This is due to their well-defined optical, electrochemical, magnetic and other physical and chemical properties. These properties are often size dependent and can be changed by varying the amount of metal atoms, the number of protective ligands, or changing the protective ligand all together through controlled synthesis. With all of this it allows these clusters to be quite useful in areas of interest such as bioimaging, catalysis, energy, drug delivery, etc[1-5].

These clusters can be synthesized with a variety of metals and ligands including gold, silver, palladium as monometallic and a mixture as bimetallic clusters, with ligands ranging from thiolates, to phosphates, and even basic halides. My research specifically focused on small gold and later silver ligand protected clusters. Figure 1.1 shows a basic representation of a thiolate protected gold nanocluster. These clusters can be synthesized in a variety of ways, but the initial methods included the Brust-Schiffrin method that was reported in 1994 and 1995[6-7]. For this reaction, chloroauric acid (Au(III), $AuCl_4^-$) is first phase transferred from water to an organic solvent with the use of tetraoctylammonium bromide as a phase transfer agent. This allows the gold to be dissolved in solvents such as toluene so that it can be used in the synthesis of organic soluble clusters. The gold is then reduced from Au(III) by the addition of thiolate molecules to form Au (I)-thiolate polymers. From there a reducing agent such as sodium borohydride is used to further reduce the gold until a gold nanocluster is formed with an Au (0) core and surrounding protective ligand monolayer.

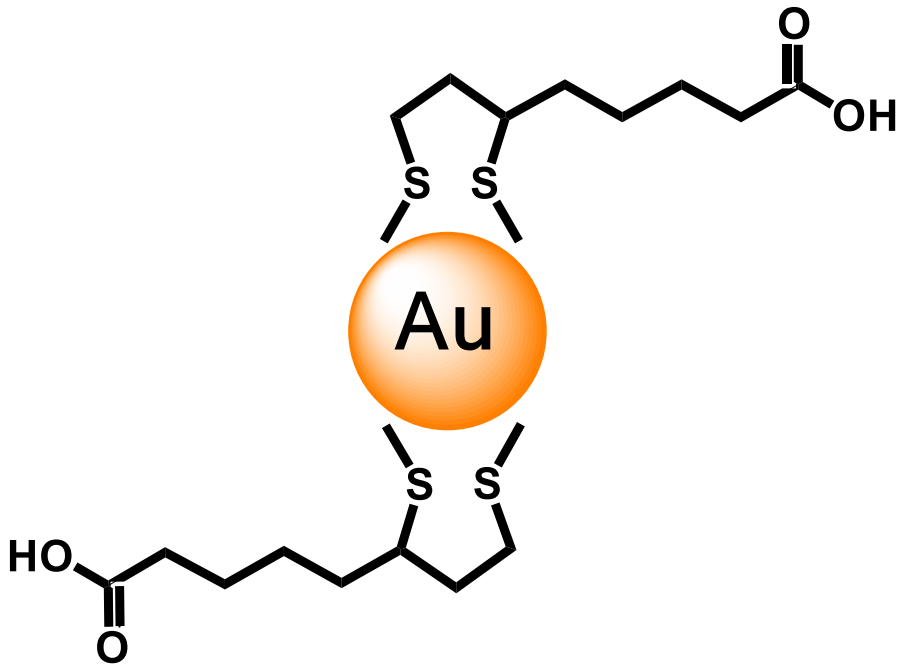

Figure 1.1. Basic representation of a di-thiolate-protected gold nanocluster. Only two ligands are sketched for clarity. The metal NCs are often described by unique compositions with discrete numbers of metal atoms and ligands.

The clusters produced during these early syntheses were relatively polydispersed with a wide range of sizes, but it gave a great starting point to further the field. From this, changing the ratios of the gold, ligand, and reducing agent along with other factors such as temperature, atmosphere, or type of ligand can easily affect the outcome of the synthesis to produce varying types and sizes of monolayer-protected gold nanoclusters. This method has also been adjusted to synthesize purely aqueous soluble gold nanoclusters. For this, the gold ($HAuCl_4$) is dissolved in nanopure water or a solvent mixture such as acetic acid/methanol, and then reduced with an aqueous soluble ligand such as lipoic acid, mercaptosuccinic acid, or glutathione. Sodium borohydride can then be used to further reduce this mixture into gold nanoclusters. Figure 1.2 shows an overall representation of synthesis of a thiolate protected gold nanocluster.

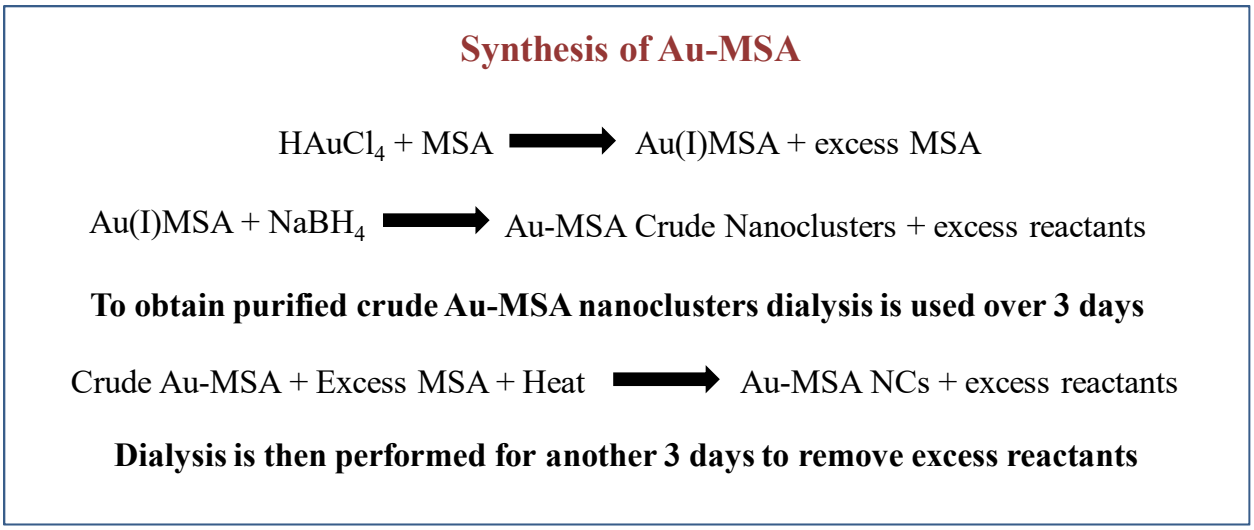

Figure 1.2. Synthesis and treatment of the Au-MSA nanoclusters. Side products such as possible disulfide etc. are omitted. The process will produce either thermodynamically stable or kinetically trapped species, or both.

Though many metals can be used in this process the most widely used is gold. Due to their incredible stability and other properties such as low cytotoxicity and high near-IR luminescence, they are useful in a variety of important applications in addition to the primary focus of the fundamental studies. Once these clusters have been synthesized a variety of experiments can be done to change or tune their properties. This includes such things as basic annealing with more of the protective ligand or even ligand exchange reactions. Exchange the ligand allows for a few possibilities. Either a new ligand can be attached to the already prepared cluster to form a protective layer with more than one types of thiols/functions, or the protective ligand monolayer can be fully exchanged to a new thiolate or other molecule. Coupling reactions can also be performed to add compounds such as polymerized PEG. This allows the cluster to be highly functionalized which in turn allows for their use in a variety of applications.

Another property of noble metal nanoclusters is their ability to form “magic number” compositions that are often highly stable with unique properties making them useful for both

basic studies and applications. Some of the "magic number" gold clusters include core sizes of $Au_{22,}$ Au_{25}, Au_{38}, Au_{104}, Au_{130}, and Au_{144}[8-11]. Recently, a new possible magic number cluster, $Au_{246,}$ was synthesized by the Jin group[12]. This cluster offered nicely defined optical features which surprisingly did not include a surface plasmon band and had highly ordered electrochemical properties including quantum double-layer charging. As of now this is one of the largest molecular-like gold nanoclusters that has been synthesized and characterized.

Many techniques are used in the characterization of gold nanoclusters including various optical spectroscopy such as UV-visible absorption and photoluminescence or luminescence, mass spectrometry, NMR, electrochemistry, electron microscopy, XPS, crystallography, and many others. The optical properties in UV-Vis-near IR spectrum range are incredibly important and for many of these clusters show distinct absorbance bands that can be correlated to their electrochemical properties. High intensity near-IR photoluminescence has also been observed with some of these clusters leading to their use in applications such as biological imaging[13]. Some bimetallic clusters have been observed with having quantum efficiency as high as 40%[14]. Figure 1.3 shows the representative optical features for a Au_{130} cluster.

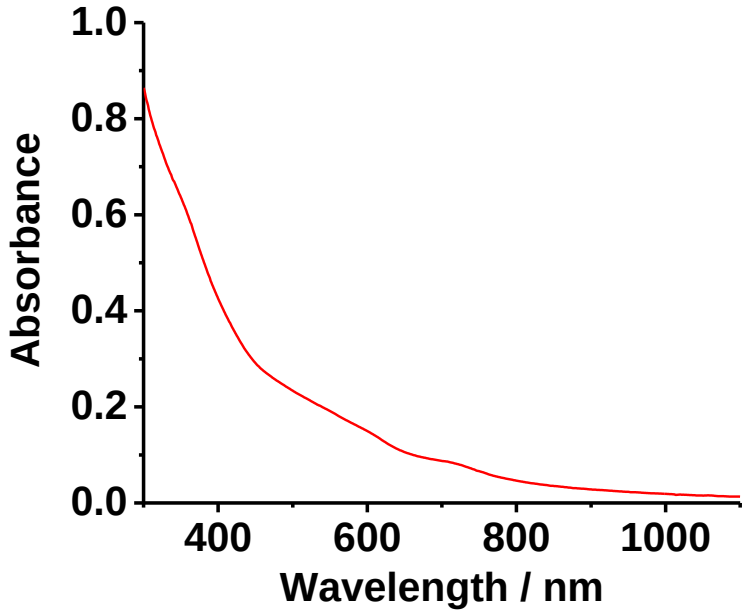

Figure 1.3. Absorbance features for the $Au_{130}(Durene\text{-}DT)_{29}(PET)_{22}$ cluster. (unpublished results)

Mass spectrometry (MS) is one of the more important techniques to elucidate the chemical composition of many of the as synthesized clusters. The main MS ionization techniques used are those of ESI, LDI, and MALDI[15-16]. For multicharged clusters the use of ESI is incredibly helpful due to its ability observe various multicharged ions. If a molecular ion cannot be observed due to being too large these multicharged species can be used to quickly determine the final chemical composition. For larger and single charged species, the use of LDI and MALDI is better suited in finding the molecular ion.

NMR Spectrometry is useful in analyzing the protective ligand monolayer though does have its drawbacks. One of the biggest issues is the ensemble measurement requires a high degree of monodispersity. If the sample is not highly monodispersed, then the result is just an average of what the spectra from all species present. The major related concern is the fact that most proton NMR spectrums have what is called the line broadening effect. This effect causes

the peaks in proton NMR to significantly broaden instead of being sharp and nicely defined and has been highly researched[17-19]. This is compounded by the things such as the size and shape of the cluster, the type of ligand that is attached to the cluster, how monodispersed it is, and how close to the gold core the proton is[20-24]. Figure 1.4 shows an example of this line broadening effect from the Au-MSA clusters. The correlations and 2D NMR, however, provide valuable information from the often broaden and shifted signals for assignment and accordingly a quantitative measure of different ligand compositions of the monolayer. In a recent work 2D NMR was used in helping to understand the oxidation occurring in the monolayer of the lipoic acid protected Au_{22}[25].

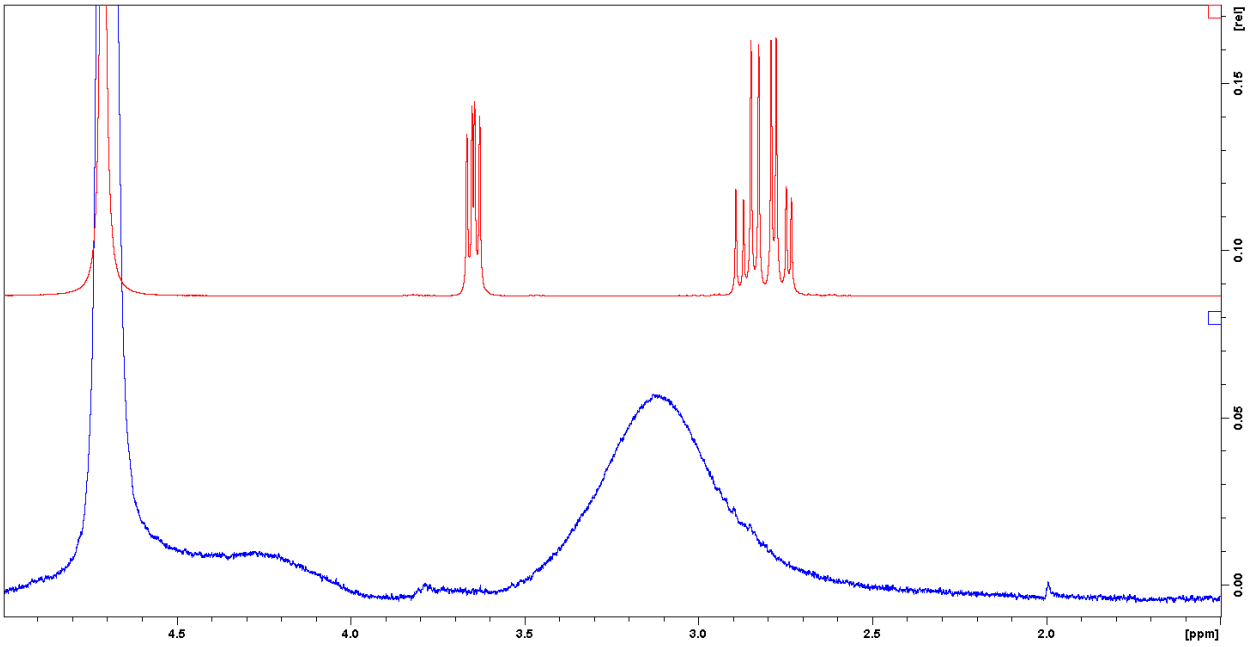

Figure 1.4. Proton NMR of the MSA ligand (Top) and Au-MSA cluster (Bottom). (unpublished results)

Electrochemical analysis of gold clusters can be of a huge importance for many things from unveiling the redox properties to evaluating size and monodispersity of the clusters. Due to

the size dependence of the electrochemical properties it is possible to determine a rough size for a cluster if proper electrochemical data is obtained. Many smaller clusters like Au_{25} and Au_{38} show distinct HOMO-LUMO spacings in the electrochemical data and medium sized clusters such as the Au_{130} and Au_{144} have size specific quantized double-layer charging features that can easily be correlated to the size of the cluster[26-31]. The electrochemical data is also useful in understanding where and why the absorbance features are observed. Using a technique called spectroelectrochemistry with the aid of electrochemical data it is possible to calculate which energy states give way to the optical features[32-34].

Two main techniques for the analysis of metal cores are transmission electron microscopy (TEM) and X-ray photoelectron spectroscopy (XPS). TEM is useful when looking at the overall gold core size. The core can be easily imaged, and this technique was used very early on to visualize the shape of various gold nanoclusters[35-38]. XPS on the other hand is useful in determining the elemental composition of the core along with the empirical formula, and the chemical and electronic state of the elements present, i.e. binding energy[39-40]. This can be incredibly useful when looking at bimetallic cores as it can help determine the ratio of the two metals in the core.

There are various categories of monolayer-protected gold nanoclusters. Molecular-like gold nanoclusters with core diameters around 1 nm or fewer than 100 gold atoms. This includes clusters such as Au_{25}, Au_{38}, and other similar sized cores. The other main category of gold nanoclusters includes clusters that behave more closely to that of bulk gold. These are large clusters with 100's of gold atoms in the core with diameter less than 2.2 nm. At even large sizes, gold surface plasmon band can be observed in the absorbance spectra at around 520 nm with little to no luminescence. There are still many applications for these clusters including cancer

treatments and other biological applications. The following sections will cover the overall characterizations of both molecular-like gold nanoclusters and a subcategory of this that includes gold nanoclusters that have a very specific electrochemical property called quantized double-layer charging which complicates the determination of energy band gap or a transition to metallic behavior.

1.2 Molecular-Like Gold Nanoclusters

Molecular-like gold nanoclusters have been heavily researched of the previous few decades. Like stated earlier this includes such clusters as the Au_{25} and Au_{38}. To help cover this topic the Au_{25} cluster will be focused on as it is one of the most highly researched clusters to date. The early work on this cluster was done by Robert Whetten and his coworkers and used glutathione as the protecting ligand. Initially it was labeled as $Au_{28}SG_{16,}$ but this was later updated once instrumental limitations had been overcome. The Murray group also synthesized and characterized a Au_{25} cluster but this one was organic soluble and used the ligand phenylethyl thiol (PET). This was unfortunately also mislabeled but this time as $Au_{38}(PET)_{24}$. In time however, advancements in ESI and other analytical techniques allowed for the correct characterization of the molecular composition. As synthetic routes became easier and advanced analytical techniques came around many of the physical and chemical properties of the Au_{25} cluster were characterized. The absorbance spectrum for the Au_{25} cluster shows distinct peaks located at 400, 450, and 670 nm though it has been noted that these features can change slightly with different charge states[41]. Figure 1.5 shows a representative absorbance spectrum for the Au_{25} cluster.

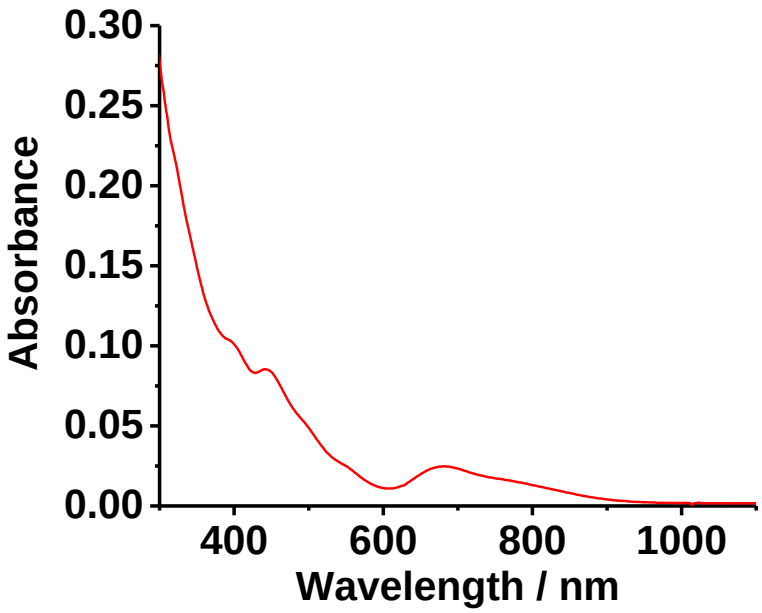

Figure 1.5. Absorbance spectra of the $Au_{25}(PET)_{18}$ cluster. (unpublished results)

The electrochemical properties of this cluster and others like it were also heavily researched[30]. For clusters of this size the defining feature is that of an observable HOMO-LUMO spacing in the voltammogram. These spacings are highly size dependent though the type of ligand attached and other factors including the solvent used during analysis can slightly affect the gap. For the Au_{25} cluster this HOMO-LUMO spacing was calculated to be 1.33 V. The electrochemical work done on this cluster also helped with concluding what the actual size of the cluster was due to the HOMO-LUMO spacing of this being different than that of the Au_{38} clusters.

Other important advancements with this cluster included some of the first crystal structures for small molecular-like gold nanoclusters. The pioneering work on crystal structures for gold nanolcusters was first done on the Au_{102} cluster[42]. This work reported on the "staple" motifs that have gone on to be used in the structure determination of many of the molecular-like

gold nanoclusters. The early structures for the Au_{25} clusters were determined by the Murray and Jin groups on both the anionic -1 and neutral species of the cluster[43-44]. These crystal structures gave way to a solid Au_{13} core with the other 12 gold atoms helping form the stable protecting monolayer. With the help of these crystal structures further predictions of the structure for other clusters including the Au_{38} have been documented and as of now have experimental support to back up these predictions[45-49].

Various other molecular like gold nanoclusters have been heavily researched in previous years including the already mentioned Au_{38} and Au_{102} clusters. Others include the Au_{13}, Au_{19}, Au_{20}, Au_{36}, Au_{40}, Au_{55}, Au_{68}, Au_{75} and the larger Au_{130} and Au_{144}[27, 50-59]. A relatively newer cluster however has been the Au_{22} cluster which has been synthesized with both glutathione and lipoic acid as the protecting ligands[60-61].

Like the Au_{25} and other molecular-like clusters the Au_{22} has its own set of distinct optical and electrochemical features. For the $Au_{22}LA_{12}$ that was synthesized by Jie Jiang et al an absorbance band at 505 nm can be observed in the spectrum[25]. This band however is dependent on the amount of oxidation the cluster has underwent either through dialysis or aging. Through FT-IR, 2D NMR, and XPS measurements it was discovered that not all the sulfur atoms on the lipoic acid are attached to gold atoms. In fact, some of the sulfur atoms go through an oxidation process to form SO_x functional groups that have interesting effects on the optical properties of the cluster. For one, the absorbance feature at 505 nm is mostly lost once the cluster is oxidized. The absorbance spectrum shows more of a featureless decay. More importantly however is the significant increase in luminescence that is observed once oxidation has occurred. An increase from 1% to 10% quantum efficiency can be observed in the luminescence spectra between the oxidized and non-oxidized species. Figure 1.6 shows the FTIR confirming the appearance of SO_x

groups on the cluster. The peaks at 1045 and 1187 cm^{-1} are like what has been observed with S=O symmetric and asymmetric stretching bands in alkysulfonic acid/sulfonate species which have peaks located at 1042 cm^{-1} and 1179 cm^{-1}.

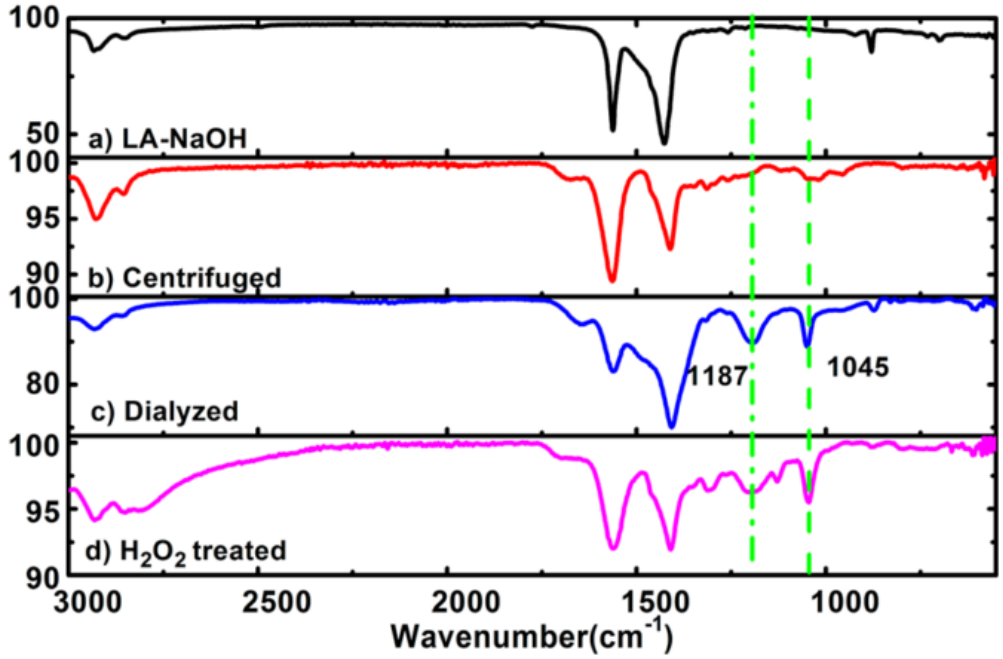

Figure 1.6. FT-IR measurements of the non-oxidized and oxidized $Au_{22}LA_{12}$ clusters. Adapted with permission from J. Phys. Chem. C 2014, 118, 20680−20687. Copyright 2014 American Chemical Society.

Further work was done by Tanyu Wang on this cluster to continue to explore its luminesce properties[62-63]. With the aid of electrochemistry, the electrochemiluminescence properties of the cluster were vastly studied with and without coreactants. By itself the $Au_{22}LA_{12}$ cluster already has significant ECL intensity. This was compounded by covalently bonding DEDA onto some of the ligands which generated an even higher signal. It was noted that the intensity of the ECL was highly pH dependent and as the pH was lowered the signal decrease significantly.

The $Au_{22}SG_{18}$ is another newly synthesized cluster that has seen incredible increases in quantum efficiency[60, 64]. The cluster in of itself has been observed with quantum efficiencies of above 10% but this was just scratching the surface. Unlike its lipoic acid variant this cluster does not undergo the oxidation that was seen when using lipoic acid as the protecting ligand. This is due to the structure difference between lipoic acid (a dithiolate) and glutathione (a monothiolate). Instead, the large increase in quantum efficiency is observed when phase transferring the cluster into organic solvents with the use of a transfer agent such as tetraoctylammonium bromide. For this particular Au_{22} studied, increases from 10% to more than 60% Q.E. This increase was affected by variables such as the organic solvent used while taking the measurement as well as which transfer agent was used. It was noted that higher dielectric constants gave way to lower Q.E. increases as well as using shorter carbon chain transfer agents. If a longer carbon chain (10 or more) was used even higher Q.E.s could be obtained. The same study also looked at the similar sized $Au_{25}SG_{18}$ and noted very similar results for the luminescence. The increases were not as substantial but a 6-fold increase in luminescence was noted.

1.3 Phase Transferring Gold Nanoclusters

This ability to phase transfer noble metal nanoclusters is a featured part of further sections of this dissertation so it is an important property to discuss. Phase transferring metals such as gold is not new as this process was done to make many of the early organic soluble clusters using the Brust-Schiffrin method. Some of the first work on phase transferring gold nanoclusters into organic solvents was done on the $Au_{25}SG_{18}$ cluster[65]. Using TOABr the cluster was quickly and completely transferred from water into toluene. An early observation was that the absorbance data in both water and toluene showed minimal changes to the peaks and overall shape of the spectrum. This is important as because of this it can be concluded that the Au_{25} core

of the cluster is unaffected by the transfer and remained intact. Due to their distinct optical properties any changes in the core would be easily observable in the absorbance measurements. Another important aspect of this transfer was how the pH would affect it. Since the glutathione has both carboxyl groups and an amine group shifts in the pH can change the overall charge associated with the clusters. Not surprisingly, the transfer was more effective at higher pHs. The transfer works because of the attraction between the negative charge on the cluster and the positive charge on the TOA^+. If the cluster is positive charged or neutral the TOA^+ would have nothing to bind to and the transfer would not proceed. This effect is studied in further detail in chapter 2.

Outside of the increases in photoluminescence, another important benefit is the fact that it allows for the use of larger potential windows during electrochemical measurements. Like stated earlier the electrochemical properties of molecular-like gold nanoclusters are an important part of the overall physicochemical properties. Unfortunately, this can be severely hindered when performing electrochemical measurements on aqueous soluble gold nanoclusters. This is in part due to the small potential window afforded by water due to water splitting occurring around +1.2 V and -1.x V. Since the potential window is narrow many redox activities that could be useful in characterizing a cluster could not be resolved before water splitting signal becomes overwhelming. Another concern is the high dielectric constant of the water that permeates and swell the protective ligand shell. This higher dielectric constant can cause broadened electrochemical features lowering the resolution of the measurements considering simple concentrate sphere model[66-68]. By transferring the cluster into an organic solvent such as acetonitrile a much larger potential window can be used and thus open the electrochemical data to being much more useful. Early electrochemical work on phase transferred clusters was done

by Kyuju Kwak et al[29]. In this study a variant of the Au_{25} cluster with (3-mercatopropyl) sulfonate as the protecting ligand was transferred and the electrochemical properties were studied and various solvent systems. Like the previous glutathione cluster, the absorbance features remained unchanged after transferring. Electrochemically, the cluster showed similar results to what had been previously reported on the Au_{25} organic soluble clusters. A main difference however was that the HOMO-LUMO spacing was solvent dependent. As increased amounts of CH_2Cl_2 were used for the measurement the HOMO-LUMO spacing went for 1.66 V to 1.39 V. The same conditions were performed on a C6-Au_{25} and this effect was not observed. It was concluded that the electrostatic field effect of the sulfonate anion was causing the redox potentials to shift. This ability to study the electrochemistry of aqueous soluble clusters in organic solvents will be further studied throughout this dissertation.

Similar to all of the smaller gold nanoclusters that have been discussed, the next group of clusters again have very distinct optical and electrochemical properties. Unlike the Au_{25} and similar sized clusters however, which exhibit HOMO-LUMO spacings, with two-electron transfer doublet peaks at each state separated by charging energy, in their electrochemical data the next group can be characterized by a much different electrochemical process called quantized double-layer charging. Generally, this is characterized by the observation of multiple oxidation or reduction peaks in the electrochemical data which are correlated to a single electron that is being added or removed from the gold core consecutively requiring relative constant charging energy and accordingly displaying uniform peak spacing.

1.4 Quantized Double-Layer Charging

The pioneering cluster which showed this distinct double-layer charging was the Au_{144} cluster that was first reported by Schaaff et al. and Chen et al[58-59]. Further work was later done to

gain an understanding of this electrochemical process[69-70]. Electrochemical data for this cluster gave way to as many as 15 oxidation states representing positive, neutral, and negative states for the cluster. Continued work on the Au_{144} cluster included simpler synthetic routes with decent yields of highly pure samples[71]. This route allowed for the synthesis of both the Au_{144} (major species) and Au_{25} (minor species) clusters to be synthesized together. Due to the differences in solubility the two clusters are easily separated by dissolving the Au_{25} in acetone. The Au_{144} cluster synthesized with this route gives way to absorbance bands at 517 and 700 nm which matches well with previous syntheses. MALDI MS data showed an observable peak at 32 kDa which was smaller than what was previously reported but this was explained by the loss of $C_6H_{13}S$- ligands while running the measurement. Electrochemically this cluster exhibited prominent QDL features with an average spacing of 0.26 V which was previously reported for the cluster.

Later work on clusters of this size gave way to many different variants showing similar features including that of the mixed-thiolate Au_{130} produced by Z. Tang et al[27]. This cluster was unique in the fact that it used both a monothiolate (phenylethyl thiolate) and dithiolate (Durene-DT) in the protective monolayer. The optical features of this cluster were distinct with 4 absorbance features occurring at 355, 490, 584, and 718 nm though it had relatively low near-IR luminescence. MALDI was used to aid in the characterization of the molecular composition. A 34 kDa peak was observed giving way to a composition of Au_{130}(Durene-DT)$_{29}$(PET)$_{22}$. Electrochemically this cluster showed the distinct quantum double-layer charging that is representative of clusters of this size. At the time 11 different QDL peaks were noted in both the oxidation and reduction scans for an average peak spacing of 0.19V and an energy gap of 0.44 V was calculated between the 5th and 6th QDL revealing an energy state below the frontier states.

This electrochemical data is represented in Figure 1.7. In the next section spectroelectrochemical techniques used to correlate the optical and electrochemical properties will be discussed.

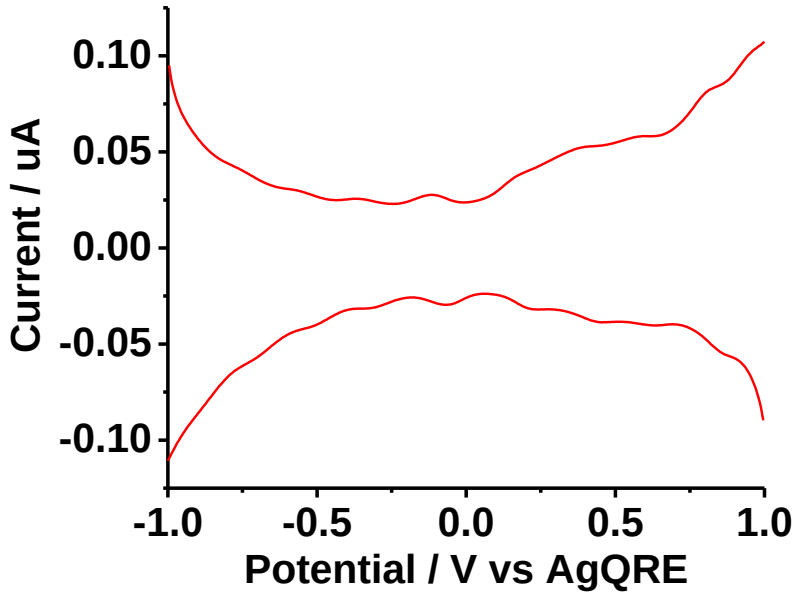

Figure 1.7. DPV of the QDL range for the Au_{130}(Durene-DT)$_{29}$(PET)$_{22}$ cluster. (unpublished results)

More recent work with clusters of this size gave way to the Au_{130}(p-MBT)$_{50}$ cluster synthesized by the Jin group[9, 72]. This was synthesized by simply changing the type of isomeric methylbenzoenethiol used during the synthesis. It was observed that three "magic number" clusters could be synthesized by switching between para-, meta-, and ortho- isomers. The ortho-isomer allowed for the synthesis of Au_{40}(o-MBT)$_{24}$. The meta- isomer was used to synthesize Au_{104}(m-MBT)$_{41}$, and the para- isomer allowed for the synthesis of Au_{130}(p-MBT)$_{50}$. Due to their synthetic conditions (high temperature and excess thiol) the final products were highly stable and monodispersed. Each sample had its own distinct absorbance features and their molecular compositions were characterized using MADLI. For the sake of discussing the quantum double-layer charging the Au_{130} will be discussed further.

Additional work was done to characterize this cluster by the Jin group including obtaining a crystal structure for the cluster. It was determined that this cluster had a four-shell crystal structure with a similar Au_{13} shell in the interior core. Outside of that a 42-gold atom shell surrounded the 13 gold atoms. The next shell housed 50 gold atoms and was surrounded by the final shell made up of the S-Au-S stable motifs using the final 25 gold atoms. The final structure closely resembles that of a barrel. Transient absorption measurements, electrochemical data, as well as a proposed energy diagram that correlates the optical data to the electrochemical data will be discussed in later chapters. As it pertains to the discussion however, well-defined QDL features are observed for the cluster with an average spacing of 0.21 V and an energy gap of 0.5 V can be calculated.

The Jin group also successfully synthesized a new $Au_{246}SR_{80}$ cluster[12]. This cluster despite its large core size was surprisingly not plasmonic and in fact had distinct molecular-like absorbance bands at 400, 460, 600, and 800 nm. Further femtosecond transient absorption measurements were performed, and the cluster was observed to have electron-phonon coupling that was independent of the pump fluence. This as well as other observations from the transient measurements suggested the cluster had a small bandgap. To help with this conclusion we collaborated with Rongchao Jin on the project to perform electrochemical studies. Square wave voltammetry showed well-defined QDL features with an average spacing of 0.15 V. An observable band gap was not seen in the measurements. It was concluded that the band gap was either 0.15 V or smaller which would go along with what was observed in the transient measurements.

1.5 Spectroelectrochemistry and Proposing Energy Diagrams

Probing the optical properties of gold nanoclusters under in-situ control of the charge states can play an important role in understand the origin of the corresponding electronic transitions. Work of this sort over the past decade has been done on various clusters including monolayer-protected gold films and different forms of the $Au_{25}SR_{18}$ cluster[34, 41, 73]. The technique of spectroelectrochemistry involves the use of an optical component with an electrochemical component. For this discussion absorbance changes after charging a cluster to different charge states will be focused on. A recent example of this kind of work is the study by Dengchao Wang et al. For this study, the Au_{130} mixed thiol cluster was used.

To perform the spectroelectrochemical measurements electrochemical data such as the potentials to drive electron transfer reactions are necessary. The measurement consisted of first holding a potential to charge the clusters within the diffuse layer on the electrode to a certain charge state (0, +1, -1) and then taking an absorbance measurement once charging is complete. Firstly, it was important to charge the cluster to the neutral charge state to obtain a baseline of the absorbance features. Afterwards selected positive or negative potentials based on voltammogram features were held to change the charge state of the cluster. Absorbance measurements were taken at each step so that a differential spectrum could be calculated. It was noted that the differences caused by changing the charge state could be reversible if the potential used would not induce chemically irreversible reactions (for example oxidation induced ligand decomposition or stripping from the cluster surface). It was observed that by oxidizing the sample the absorbance features decreased throughout the spectrum whereas most of the features increased when reducing the cluster. Also, new discrete absorption bands were observed that

were not seen in steady state measurements. This was attributed to energy transitions involving both the core and ligands.

The increasing and decreasing of the absorbance features under in-situ electrochemistry control reveals the respective energy states involved in the corresponding optical electronic transitions. An energy diagram was proposed. It was concluded that the decrease in absorbance features during oxidation was due to the removing of electrons from the frontier energy states. Removing these electrons left the states empty without electrons available to be transferred to the LUMO state. The increase in turn is due to the filling of the states during reduction. This allowed for a greater number of electrons to be transferred to the LUMO as there were more states accessible. For reference, the energy diagram proposed is in Figure 1.8

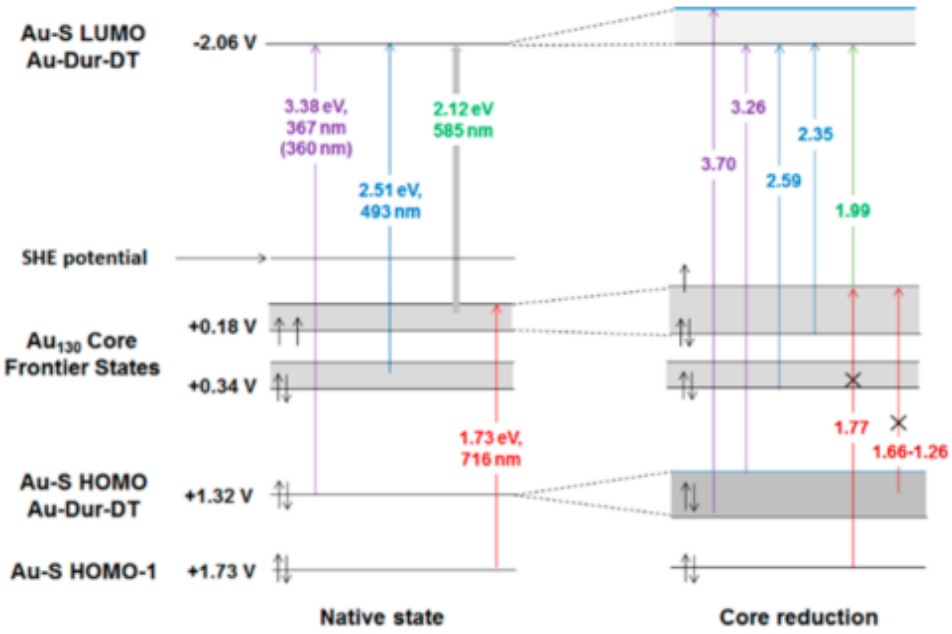

Figure 1.8. Proposed energy diagram for the Au_{130} cluster. Adapted with permission from ACS Nano. 2015. 9. 8. 8344–8351. Copyright 2015 American Chemical Society

1.6 Au NC Applications

Due to properties such as long-term stability, ability to covalently bond biocompatible molecules such as PEG or biomarkers, high near-IR luminescence, and low cytotoxicity monolayer-protected gold nanoclusters have been explored in many important biomedical applications such as biosensing, biolabeling, drug delivery systems, and cancer treatments as well as many more. The next few sections will briefly outline just a few representative examples of the research that has been undertaken in these fields.

1.6.1 AuNCs used for Biosensors and Bioimaging

Due to many of the gold nanoclusters having tunable near-IR luminescence and large stoke shifts their ability to be used as sensors or as "dyes" has been an important research topic. It is not unheard of for an aqueous soluble cluster to have a stoke shift in the range of 300-400 nm with photoluminescence, often referred as luminescence, in the range of 700 to 800 nm peak intensities with peak excitations in the 350 to 550 nm range. This is important because it allows for the use of multiple dyes in biological samples such as cells. Many organic dyes can also be excited with sources in the comparable wavelength range and their emission is nearby as the stoke shifts are usually much smaller compared to gold clusters. Due to this both a dye and nanocluster could be injected into a biological sample and with the use of filters one or both emissions can be observed. This ability was studied in detail with the Au-MSA cluster[13]. In this paper HEK293 cells were stained with both DAPI (P36391;Invitrogen) and Au-MSA clusters that had been PEGylated forming an Au-MSA-PEG cluster. Luminescence confocal microscopy was then used to view both the DAPI and pegylated clusters. By switching filters, the DAPI or clusters could be "turned off" allowing for the observation of either one. With the use of z-stack

imaging it was concluded that the clusters were absorbed into the cellular cytoplasm and even managed to get inside of the nucleus.

In an earlier study Au_{23} clusters capped with glutathione were functionalized with streptavidin with the help of EDC coupling[74]. Due to the attached streptavidin the clusters were able to stain HepG2 because the cells contained biotin. The streptavidin binds strongly with the biotin, so the cells could be easily imaged with the use of luminescence confocal microscopy. By comparing the luminescence imaging with bright field imaging and a control where the streptavidin was not attached to the cluster it was concluded that the clusters had interactions with the cells. Without the attached streptavidin no clusters were observed on the cells after washing with PBS.

As biosensors studies such as the one performed by Kwak et al showed gold nanolcusters to be quite versatile as an ionic liquid[75]. It was reported that by combining a negatively charged Au_{25} cluster with imidazolium cations a stable ionic liquid could be made with both ionic and electronic conductivity. This new liquid could then be used as a matrix for amperometric enzyme sensors designed for the detection of glucose. High electrocatalytic activity as well as substrate affinity was noted when using glucose oxidase and the clusters were observed as acting as redox mediators and electronic conductors that determined the detection sensitivity.

1.6.2 AuNCs as Catalyst

Catalysis is another area of interest that has seen much research performed with gold nanoclusters. Initially thought to be inert, particular with protecting ligands, gold nanoclusters were eventually found to be useful in the catalysis of carbon monoxide. Early success used the help of transition-metal oxides and afterwards many new ways of using gold nanoclusters to catalyze CO were discovered[76]. Heavy research on how to enhance catalytic properties such as

efficiency, selectivity, and recovery have been carried out over the last few decades. Recent studies on the topic include the interface engineering of gold nanolcusters for CO oxidation catalysis by Jin et al[77]. In this paper the $Au_{38}SR_{24}$, $Au_{36}SR_{24}$, and $Au_{25}SR_{18}$ were synthesized using different ligands with varying bulkiness (R structure). Characterizations were first performed on the as synthesized clusters including absorbance measurements and MALDI-MS to determine sample purity. In each set of clusters, the optical features were similar with only minor shifts of peak position or peak intensities. MALDI-MS results helped confirm the chemical composition of each cluster as they matched what was previously reported or showed minor differences depending on the ligand used. Once the structure had been confirmed for each cluster, CO oxidation studies were carried out to determine how well each cluster would fare. For the Au_{38} samples it was observed that the sample prepared with SCH_2CH_2Ph had higher activity than the SPh, and o-MBT variants. It was concluded that this was due to the sulfur atom not being directly connected to the aromatic ring. Having the aliphatic chain between the ring and sulfur atom allowed for less crowding at the reaction interface and enabled an enhanced catalytic activity. The Au_{36} clusters put further emphasis on the role of the interface. Regardless of the ligand used, catalytic activity was consistent leading them to believe the more important trait was the interface sites available for catalysis. Finally, the Au_{25} clusters further corroborated the Au_{38} and Au_{36} results. Steric hinderance played an important role in the results as the bulkier SCH_2CH_2Ph ligand allowed for double the catalytic activity as the 2SNap and 1Snap variants.

There are of course many other applications for monolayer-protected gold nanoclusters that have not been discussed here. These include such things as contrast agents for biomedical purposes. As more and more uniquely distinct clusters are synthesized and characterized new

uses for them with undoubtedly be researched. Their incredible physical and chemical properties allow for them to be at the forefront of highly significant research.

1.6.3 AuNPs used for Cancer Treatments and Imaging

As it is well known, cancer is a serious disease that effects millions of people every year. Improved treatments over the past few decades have insured many people have the ability to fight this disease, but there is always room for more efficient and safe routes to defeating this disease. Over the last decade or so larger monolayer-protected gold nanoparticles (not to be confused with the much smaller gold nanoclusters that have been previously discussed) have started to become of significant interest in this field and advancements in applications such as laser photothermal therapy, optical scattering microscopy and detection, drug delivery and targeting, and their innate ability to intrinsically act as therapeutic agents. Much of this research has been done on particles that exhibit surface plasmon resonance due to their sheer size and optical properties[78]. It was noted that gold nanoparticles have the ability to have incredibly large amounts of ligands/cm^2, in fact 100-1000 times higher than liposomal or polymetric nanoparticles[79], and are selective with their accumulation at tumor sights. This allows for the photothermal ablation with near-IR lasers[80-81]. As a probe, larger plasmonic gold nanoparticles become highly useful due the shear amount of scattering intensity. As noted particles on the range of 80 nm have more scattering intensity as a single unit than other probes such as Alexa Fluor dyes or Qdot 800 quantum dots[82]. Due to this and other photophysical properties the larger gold nanoobjects have many spectroscopic applications that are important in cancer research. These includes things such as two-photon luminescence imaging[83], optical coherence tomography[84], and surface enhanced Raman scattering (SERS)[85]. With their size large size plasmonic gold nanoparticles have been at the forefront as drug delivery systems. Studies by

Paciotti, and Tamarkin showed success at delivering drugs to cancer sites in mice and later clinical trials showed the ability to deliver tumor necrosis factor α (TNFα) at a dosage 3 times that was previously reported. These trials also showed little to no serious adverse side effects[86-88]. Important work on this topic has also be studied by Mirkin, Rotello, and Xia[89-91]. Obviously, this is barely skimming the top of the tremendous work done on using gold nanomaterials in the detection and treatment of various cancers.

1.7 Ag NCs: Synthesis and General Characteristics

Like their gold counterparts monolayer-protected silver nanoclusters have been the subject of much research recently. Though they have many useful and distinct properties there are some major drawbacks with silver clusters. One of the biggest concerns is their high susceptibility to oxidation in air. This can cause serious complications with the overall stability of the cluster rendering them not as useful as many of the highly stable gold nanoclusters. Another disadvantage of silver clusters is their inherent high cytotoxicity. This inability to not negatively affect biological systems limits their usefulness in many applications. Though there are several severe drawbacks this has not given them a negative perception and they have found uses in many applications.

There are various synthetic routes for making silver clusters, but many can be synthesized using the Brust-Schiffrin method or a modified version of it. This however is not the only successful synthesis technique. Another highly used technique is simply using a mortar and pestle to grind the reactants together. Once formed the clusters are extracted by dissolving them in the preferred solvent. This performed in laboratory atmosphere has been used to synthesis clusters such as the Ag_{55}, which will be discussed later[92].

Some of the earliest work on silver systems was performed by Henglein and Dickson[93-94]. There work will be discussed in greater detail in a later chapter, but briefly Henglein was able to synthesize citrate protected clusters by irradiating the silver/citrate mixture with a commercial ^{60}Co γ source. Dickson's work included the observation of single cluster fluorescent blinking with the use of luminescence microscopy. This early work helped pioneer the field and led to many important advancements in the synthesis and characterization of silver nanoclusters.

In a recent study by Xie et al[95], various monothiol ligands were used to better understand the effect the ligand had on the creation of different sized Ag clusters. It was shown that by varying the ligand (MHA, p-MBA, or GSH) clusters sizes of Ag_{25}, $Ag_{9\text{-}15}$ and Ag_{44} could be easily obtained. The MHA protected Ag_{25} clusters showed the distinct peaks around 336, 486, and 665 nm that are characteristic to this cluster. Using glutathione, absorbance measurements only showed one main feature at 480 nm which is similar to what is seen with previous Ag_{14} clusters. The Ag_{44} was made with the use of p-MBA and optically showed absorbance features at 422, 496, 548, 648, and 840 nm which had been previously reported for that core size. To further characterize these clusters ESI as performed and molecular formulas of $Ag_{25}MHA_{18}$ and $Ag_{44}(p\text{-}MBA)_{30}$, ESI on the glutathione protected cluster gave a variety of smaller compositions in the $Ag_{9\text{-}15}$ range including Ag_9SG_5, $Ag_{12}SG_8$, $Ag_{15}SG_8$, and a few others. These differences in size were concluded to be due to the various steric hinderances caused by the different size and shapes of the ligands.

Like the gold nanoclusters, various "magic number" silver clusters have been successfully synthesized. This includes clusters such as Ag_{13}, Ag_{55}, Ag_{146} and larger sizes such as Ag_{309} and Ag_{561}. Each of these clusters have their own distinct properties and applications. Of course, many other variations of silver cores have also been synthesized. The next couple sections will

summarize some of the more recent work that has been done on silver clusters as it pertains to molecular-like silver clusters and not clusters exhibiting plasmonic properties.

1.8 Molecular-Like Silver Nanoclusters

Molecular-like silver nanoclusters coming in a variety of sizes and use many of the same ligands as their gold counterparts for their protective monolayer. One such sought after cluster is that of the Ag_{55}. In a recent study performed by Pradeep et al, a successful and controlled synthesis of this cluster was carried out. Like stated earlier this synthesis was performed dry and in laboratory atmosphere. This was done by grinding the silver ($AgNO_3$) with the ligand (4-(tert-butyl) benzyl mercap-tan) together in a 1:4 ratio. This was also optimized to be done with the use of phenylethyl thiol. Once thoroughly mixed this was reduced with the addition of sodium borohydride. The clusters were extracted with toluene and then precipitated with the use of methanol which efficiently purified the newly formed Ag_{55} cluster. It was noted that stability was an issue as at room temp it would last for around 8 days. This could be increased by lowering the temperature or leaving it as a powder. Both MALDI and ESI were used to characterize the composition and it was determined to be $Ag_{55}(BBS)_{31}$. Optical properties were characterized using UV-Vis and similar features were noted between both the $Ag_{55}(BBS)_{31}$ and $Ag_{55}(PET)_{31}$ clusters.

Another cluster with a mirroring gold core is that of Ag_{25}. In a study by Bakr et al this cluster was synthesized and characterized including a full characterization of its crystal structure[96]. The synthesis was carried out by mixing $AgNO_3$ with the ligand $HSPhMe_2$. This created an insoluble Ag-thiolate precipitate. An aqueous sodium borohydride was then used to further reduce this in the presence of phosphonium bromide. It was noted that the PPh_4^+ ions

were a requirement to obtain the Ag_{25} cluster as they were negatively charged. Once purified these clusters could be dissolved in a variety of solvents such as DCM and toluene as well as many others. Optical features included distinct absorbance peaks as well as near-IR luminescence centered around 850 nm. In the absorbance spectrum it was noted that peaks like both Au_{25} as well as other silver clusters were present. The observation of a strong peak at 490 nm resembles what is seen in the Ag_{35} and Ag_{44} clusters. A broad peak at 675 is incredibly close to the peak seen with the Au_{25} variant. Other peaks below 450 nm were also like the Au_{25} cluster. MALDI and ESI was used to confirm the composition and both techniques gave way to the composition of $[Ag_{25}(SPhMe_2)_{18}]^-$. Crystal structure analysis of the cluster provided much insight as to why the Ag_{25} and Au_{25} clusters shared many similar optical properties. It was noted that like with the Au_{25} cluster and internal Ag_{13} core could be observed with the other 12 silver atoms forming the S-Ag-S motifs. A main difference however was that the 3 of these nonicosahedral atoms lied facing away from the triangular face centers. In the Au_{25} all 12 atoms nonicosahedral atoms are noted to lie at the center of the triangular faces. As stability of silver clusters is always an issue studies were carried out against a Au_{25} counterpart for comparison. Unsurprisingly the silver cluster was less stable though at lower temp it was observed that the Ag_{25} was stable for many weeks.

Additional studies performed by Bakr et al included one on the synthesis and characterization of a bi-ligand Ag_{67} cluster. At the time it was noted as being one of the largest non-superatom Ag clusters synthesized. Synthetically, this was created by mixing silver nitrate with the $HSPhMe_2$ ligand used in the making of their Ag_{25} cluster. Afterwards triphenylphosphine was added allowing for the formation of silver-thiolate-phosphine complexes. This was reduced with $NaBH_4$ and purified by methanol once this synthesis had

completed. Optical the cluster had well-defined absorbance bands (not specifically noted) and near-IR luminescence. ESI was used to determine the composition of the cluster. A 3^+ peak was noted corresponding to $[Ag_{67}(SPhMe_2)_{32}(PPh_3)_8]^{3+}$. Experimental and theoretical isotopic patterns matched validating that this composition was correct. Crystal structure data showed an overall rectangular box structure with an inner Ag_{23} core forming the "box". The rest of the silver atoms encapsulated the Ag_{23} core forming the protecting layer. Analysis of the electronic structure of the cluster gave way to a HOMO-LUMO spacing of 0.36 V and it was concluded that the cluster was electronically stable.

Other molecular-like silver clusters include the likes of Ag_{38} and Ag_{63}. Very recent work on the Ag_{38} and Ag_{63} clusters was published by Zheng et al[97]. In it, optical and crystal characterizations were carried out. Optically both clusters showed well defined and distinct features. The Ag_{38} showed peaks at 413, 507, and 563 nm with shoulders at 351, 468, 609, and 767 nm. The Ag_{63} on the other hand had peaks at 235, 415, 470, and 840 nm with only two shoulders at 368 and 530 nm. Luminescence measurements for the two clusters were not reported. The crystal structures for both clusters were cubic in nature. The Ag_{38} crystal was shown to be formed by four fcc units. These were arranged in a square fashion that shared faces and can be described as an octacapped octahedron. The Ag_{63} crystal was put together similarly but with 8 square fcc units forming a full cubic structure. Further work was noted showing the crystal structure of a Ag_{14} cluster. This represented the basic "building block" of the other two clusters as it was observed as a single square unit. With all this knowledge a prediction of a 3x3x3 cube was carried out. Calculations performed predicted that the cluster represented by this structure should be on the order of Ag_{172}.

These aforementioned examples generalize the incredible field of monolayer-protected silver or metal nanoclusters. The next section will discuss just a few representative studies on the applications that have shown the usefulness of various sized silver nanoclusters that will motivate or sustain growth....

1.9 Ag NC Applications

Like stated earlier, despite their inherent issues of relative low stability and higher cytotoxicity than gold nanoclusters, silver nanocluster have still played important roles in various applications. This includes such things as water treatment, biomedical fields, and many various industries[98-101].

A review recent on silver nanoclusters by Xie et al described usages in this fields of antimicrobials, biosensing, and bioimaging[102]. As antimicrobials silver nanolcusters have been shown to be effective on a wide spectrum of microbes. At the time the mechanism behind this however was not known. Possible mechanisms were suggested such as the damaging of membranes, destroying DNA, or the production of radicals such as reactive oxygen species. This effectiveness was also attributed to their smaller size which in result lead to higher surface to volume and more active surface atoms. This allows for a higher efficacy compared to larger particles or even their gold counterparts. In the review a report studying the effectiveness between sub 1 nm clusters versus larger nanoparticles and antibiotics showed that the smaller clusters had a much higher efficacy against Eschericia coli and Staphylococcus. In another study it was shown that the $Ag_{16}SG_9$ cluster could effectively inhibit the growth of Pseudomonas aeruginosa and had higher efficacy compared to the most effective antibiotics used at that time.

A more recent study on this application was done by Xie et al and used silver nanoclusters packed with daptomycin[103]. In this report $Ag_{16}SG_9$ clusters were synthesized and

quickly characterized to show purity. Absorbance measurements showed at 490 nm that is representative of clusters of this size. Afterwards the daptomycin was conjugated to the cluster though overall core size did not change. Optical and luminescence measurements showed consistent results verifying this. Luminescence microscopy was then used to determine the impact on the bacteria by these clusters. It was observed that the D-AgNCs were highly effective at killing and this was due to their ability to localize both cluster and daptomycin within a network to essentially double team the bacteria. Membrane damage caused by the daptomycin along with the generation of reactive oxygen species allowed for additional D-AgNCs to enter the bacteria and cause severe DNA damage.

The review mentioned above also discussed the usage of silver nanoclusters as bioimaging and biosensing. Due to many of the silver clusters having strong luminescence they are strong candidates to be used in bioimaging applications. In the review it was noted that glutathione protected silver nanoclusters had been used in the imaging of epithelial lung cancer cells. Since the clusters were in the sub nanometer range they could easily penetrate into the cells. The clusters also exhibited strong photostability and colloidal stability in a wide pH range. As biosensors a study using $Ag_{16}SG_9$ clusters was discussed. It was observed the clusters shown high selectivity and sensitivity when detecting cysteine. This detection was done by the cysteines ability to break up the clusters by strong Ag-thiol interactions. Tests on the other naturally occurring amino acids showed the clusters were unaffected by their presence.

In another study by Vosch et al, silver nanoclusters were used for the rapid detection of microRNA with the use of a DNA probe[104]. Using a particular DNA sequence (DNA-12nt-RED) as the ligand a red emitting AgNC was synthesized. This cluster had a peak luminescence 620 nm with a quantum efficiency of 32%. To this cluster, the complementary DNA sequence of

RNA-miR160 was attached to the DNA-12nt-REDsequence. Once formed the new cluster retained its high red luminescence. Testing with the microRNA sequence showed significant decreases in the luminescence intensity caused by the presence of the microRNA in the system. Control experiments using non-complementary microRNA showed less of a decrease. This was further expanded on by using whole plant endogenous RNA where when a mutant was used that was miRNA deficient, the luminescence signal generated was much higher than when the miRNA was available.

Again, this is just barely touching the surface of the many uses for silver nanoclusters. Like their gold counterparts continued research will only allow for their use in advanced biomedical techniques as well as many other applications that affect the daily life of everyone. The next four chapters will go through the work performed on both gold and silver monolayer-protected nanoclusters. The focus of this PhD work is the optical and electrochemical characterizations of a few monolayer-protected clusters and their ability to be phase transferred in organic solvents. Addition work on the electrochemical and spectroelectrochemical properties of a $Au_{130}(p\text{-}MBT)_{50}$ cluster helped correlate optical properties with their corresponding electronic transitions allowing for the proposal of an energy diagram.

2 ENABLING BETTER ELECTROCHEIMCAL ACTIVITY STUDIES OF AQUEOUS SOLUBLE AU CLUSTERS BY PHASE TRANSFER AND A CASE STUF OF LIPOIC ACID STABILIZED AU22

In stark contrast to organic systems, insight of the electrochemical properties is rather limited in aqueous for Au clusters that have received extensive research attention recently. We demonstrate phase transfer as an efficient strategy to shuttle the Au nanoclusters between aqueous and organic solvents cyclically. The ability to phase transfer the Au clusters circumvents the limitations of potential window and high dielectric constant of water for electrochemistry studies. Two types of ligand molecular structures were employed with different hydrophilicity/hydrophobicity: mercaptosuccinic acid and lipoic acid that highlights a longer hydrophobic portion and disulfide (two S- for Au bonding). The transfer efficiency was evaluated at different pHs. Additional redox activities from $Au_{22}LA_{12}$ cluster were successfully resolved that could not be seen from aqueous measurements. Reversible and controllable transfer between aqueous and organic phases is believed a generalizable approach that could enable broader applications.

2.1 Background and Strategy

Metal clusters stabilized by a monolayer of covalently attached ligands are of great interest due to their size dependent optical, electrochemical, magnetic and other properties. [4, 105-108] Strong covalent Au-S bonding in Au-thiolate clusters not just define unique compositions, $Au_xLigand_y$ or 'magic number/size' that often fulfills electron close shell structures, it also render great stability and compatibility for basic studies and applications.[109-110] Electrochemical techniques have successfully characterized the redox activity and energetics of various organic-soluble noble metal clusters.[105] However, in aqueous solutions, the narrow potential window (without triggering

solvent reactions) and the high dielectric constant (in consideration of solvent penetration into ligand monolayer) limit the electrochemical analysis of water soluble clusters.[75, 111]

Phase transfer across liquid-liquid interface is a routine practice with appropriate surfactant or counter ion species in colloidal and interfacial science. In fact, the first step in the seminal Brust-Schiffrin synthesis is to transfer the aqueous soluble $AuCl_4^-$ ions using a transfer agent tetraoctylammonium (TOA^+, bromide as counter ion) into organic phase.[112-113] Phase transfer is also shown effective in the synthesis and post-synthesis derivatization of metal clusters.[18, 114] An essential question for generalization would be what effect the transfer would have on the cluster's optical and electrochemical features. To address such question, clusters with well characterized properties are prerequisite. An ideal system is the $Au_{25}SR_{18}$ clusters in which SR can represent organic soluble ligands such as phenylethanethiol (PET or PhC2), hexanethiol (C6S) or other alkanethiols, or aqueous soluble ones such as glutathione (SG).[30, 115-119] Discrete molecular-level energy states including a 1.3-1.6 eV HOMO-LUMO gap can be resolved by electrochemical measurements in organic solvents. These electron transfer (ET) features correlate well with those distinct UV-Vis absorption bands and theoretical analysis based on density function theory calculations.[106, 115, 120] Another choice would be larger clusters in $Au_{130-146}$ range, in which the energy states are more continuum instead of molecular-like.[27, 32] Electrochemical measurements reveal multiple one-electron transfer activities, i.e. quantized double layer (QDL) or coulomb staircase charging, corresponding to continuous or degenerated energy states. [105] Neither the discrete ET in smaller clusters nor the continuum QDL charging in larger clusters could be measured in aqueous constrained to a much smaller potential window and charging energy due to higher dielectric constants. It is desirable to better understand the electrochemical property and characterize the energy diagram of those aqueous soluble clusters. On the other hand, great success

has been achieved to synthesize highly uniform clusters in organic solvents. Aqueous compatibility will greatly enhance their potentials for biomedical and sensing applications.

Phase transfer of the $Au_{25}SG_{18}$ clusters have been shown to retain the optical properties specifically the major peaks in UV-Visible absorbance.[65] Recent work on an $Au_{25}MPS_{18}$ (mercaptopropyl sulfonate) cluster revealed similar distinct Au_{25} electrochemical features seen in other organic soluble Au_{25} clusters.[29] Interestingly, the HOMO-LUMO gap of the phase transferred clusters varied with solvent polarity, but could be lined up with the previously determined HOMO-LUMO gap value for a C6-Au_{25} cluster by adjusting solvent compositions.[29] The results suggest the monolayer capacitance (permittivity) affected by combined contributions from solvent permeation and electrostatics between the counter ions with the ligand terminal groups that require further quantification. [75, 111]

In this chapter, two types of ligands were employed to establish a generalizable transfer strategy: dithiolate clusters stabilized by lipoic acid (LA)[25] and monothiolate clusters by mercaptosuccinic acid (MSA)[13]. Different monolayer hydrophilicity or hydrophobicity is defined by the ligand molecular structures. In addition to transfer aqueous soluble Au clusters into organic phase, a reversal transfer of the clusters back into aqueous phase is achieved by the selection of different counter ions. Electrostatic interactions between the deprotonated carboxylic acid and TOA^+ counterions (Br^-) for organic transfer, and reversal transfer to aqueous by Na^+ (ClO_4^-), enable the phase transfer and depend on pH and ionic strength. Electrochemical properties of $Au_{22}LA_{12}$ are resolved and reported for the first time. The oxidation of one of the two sulfur atoms in some of the LA ligands under ambient conditions over time, into SO_x as previously characterized,[25] is proposed to account for some irreversible and gradual transitions in the observed electrochemical features

2.2 Results and Discussion

2.2.1 Phase Transferring the AuNCs

The images in Figure 2.1 show the effective transfer of Au-MSA clusters, with a highly hydrophilic monolayer, from water to toluene and back to water. Au-LA clusters display similar trends (not shown). Au clusters will not transfer without TOA^+ in toluene as shown in Frame A. The gradient color is due to the surface tension-induced curvature along a distinct water-toluene interface. Frame B shows the intermediate states of the transfer in the presence of low stoichiometry TOABr after mechanical shaking/mixing. The Au-MSA clusters were completely transferred into toluene with an excess of TOABr shown in frame C. This process is readily reversed by the addition of sodium perchlorate in aqueous phase as shown in frame D. Further, the presence of excess ionic electrolytes in aqueous phase greatly inhibits the transfer efficacy into organic phase. Ionic inhibition and efficient reversal transfer are due to the high hydrophilicity of the ligand molecular structures. As rule of thumb, the co-ion in the phase transfer agents, Br^- or ClO_4^-, should be soluble in the original solvent of Au clusters to achieve charge balance during the transfer

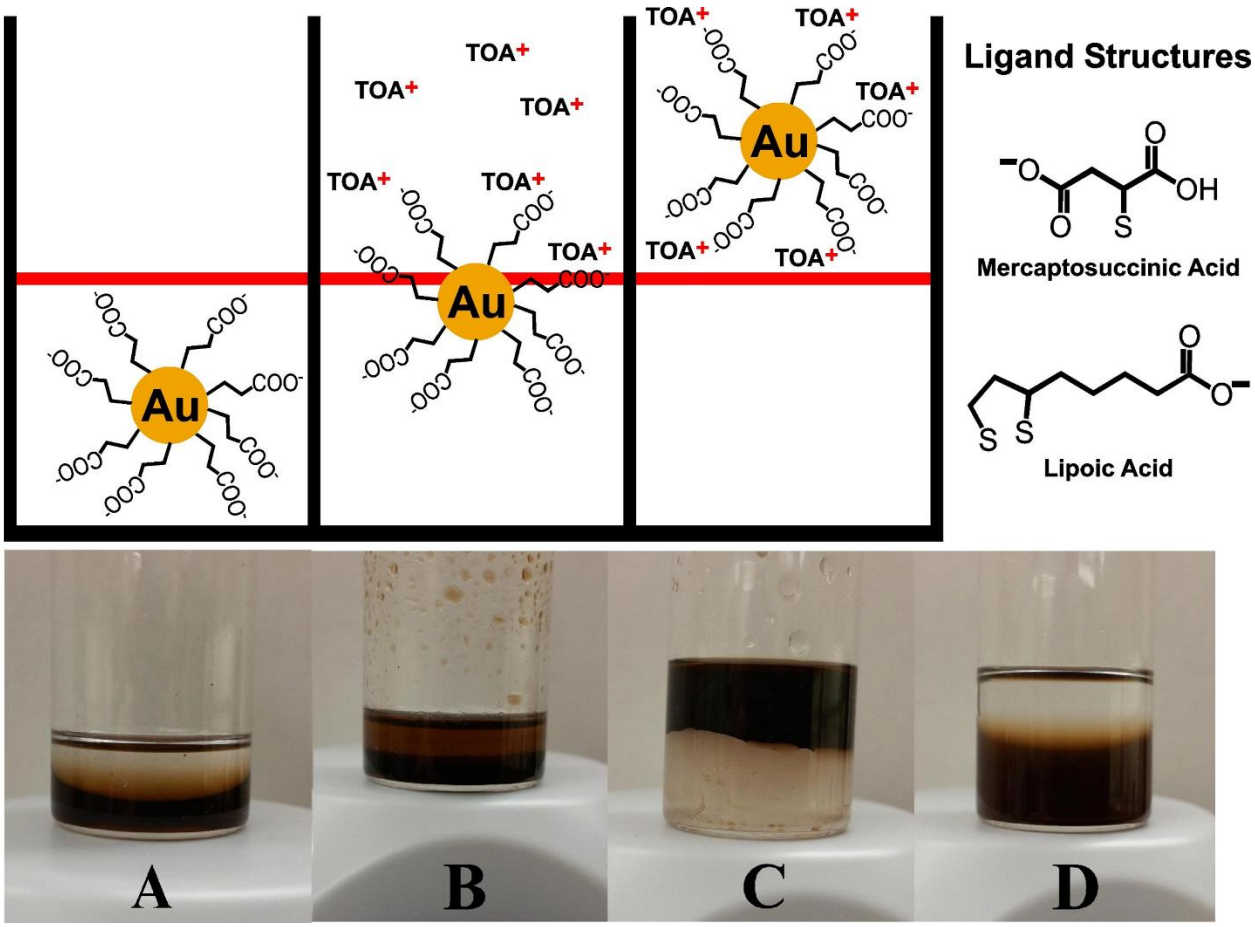

Figure 2.1. Top) Cartoon representation of the phase transfer processes and ligand molecular structures. Bottom) Experimental pictures at different stages of the phase transfer for the Au-MSA nanocluster from water to toluene and back to water. The top layer is organic (toluene) while the aqueous layer is on bottom due to density differences. Frame A: without TOABr; B: low stoichiometry TOABr added in toluene; C: Excess TOABr in organic phase; D: $NaClO_4$ added to aqueous phase.

To evaluate the essential roles of electrostatic interactions between the ligands and TOA^+, the transfer efficiency for both Au-MSA and Au-LA clusters is quantitated at different aqueous pHs. The transfer efficiency was calculated by a ratio of the cluster absorbance in toluene to the total absorbance in both toluene and water. Normalized absorption spectra in aqueous, in organic and in aqueous after the reversal transfer are provided Figure 2.2.

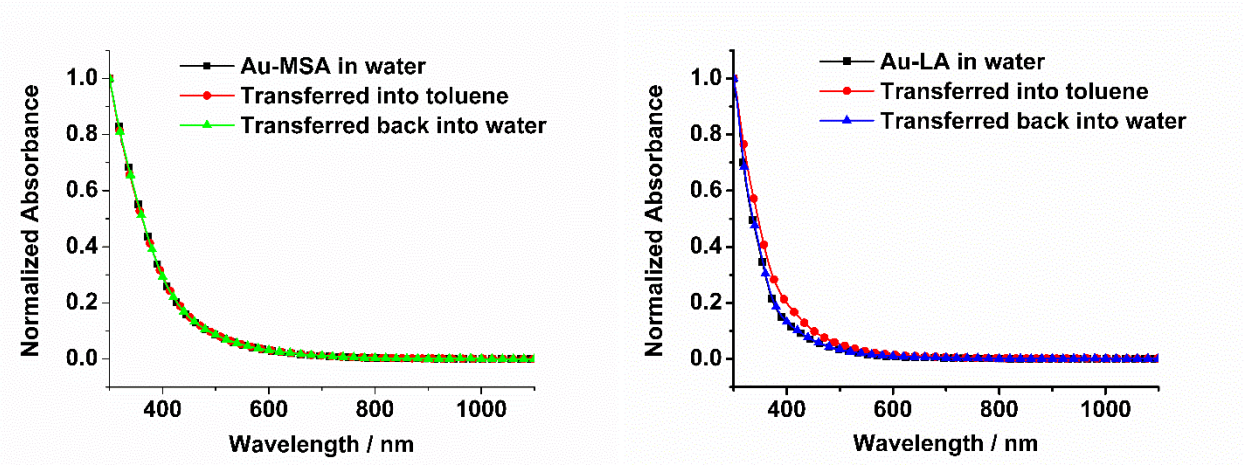

Figure 2.2. Overlayed UV-Vis spectra of Au-MSA and Au-LA clusters at different stages of the phase transfer. Spectra were normalized at 300 nm.

The Au-MSA cluster remain unchanged while there appears to be more gradual decrease in visible absorption toward longer wavelength for Au-LA clusters in organic solvent. The absorption change is postulated to the variation in the permeation of solvent/counter ions in the monolayer that requires further study.

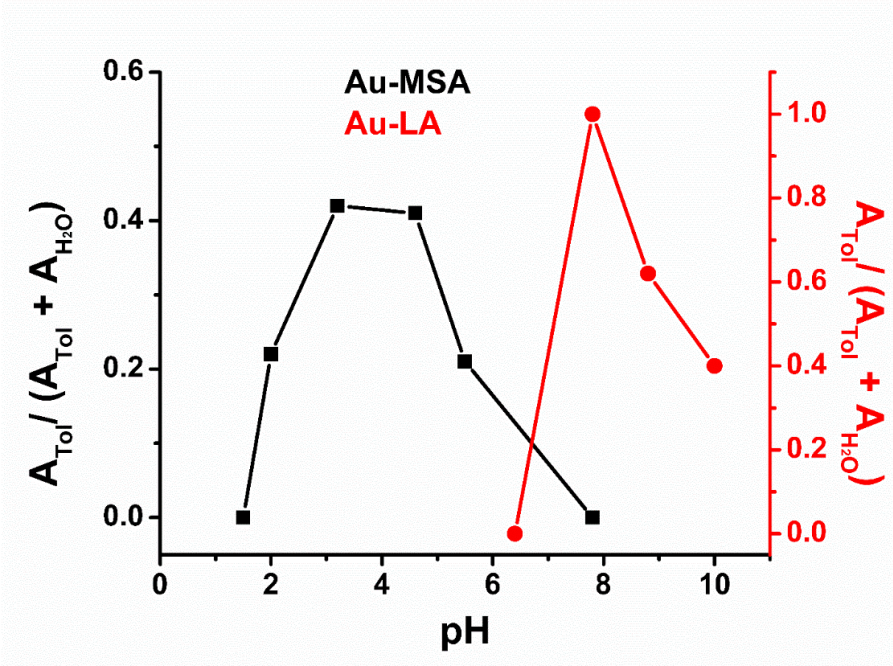

Figure 2.3. Transfer efficiency for the Au-MSA and Au-LA clusters at different pHs. Absorbance values were taken at 400 nm. The amount of TOABr used was controlled to be below or in stoichiometry to ligands (i.e. Fig. 1 B), so that the differences in transfer percentage can be resolved. Due to this the transfer effiency of the Au-MSA does not reach 100%.The pH is adjusted by the addition of either concentrated HCl or NaOH solution.

The highest transfer percentages for Au-MSA clusters are at a pH range of 3-5. The pKas of the two carboxylic acids on the MSA ligand are very close to the same range (3.3 and 4.6). It is worth mentioning that unlike free molecules with a distinct pKa, de-/protonation of ligands on clusters are known to be gradual over wide pH ranges due to surface effects.[121] If the pH of the solution is either more acidic (<2) or basic (>7), the transfer of Au-MSA to toluene does not occur. The observation suggests that the transfer is most efficient when part of the carboxylic acids in the monolayer is deprotonated. With little to no electrostatic interactions, i.e. one pH unit below pKa corresponding to 90% of the MSA ligands being protonated, transfer is suppressed due to the reduced cluster-TOA^+ interactions. When the pH is much higher than the pKa, it is possible the Au-MSA has too many charges to overcome the surface energy at the

water/toluene interface via mechanic forces to initiate contacts with the TOA^+ (middle scheme in Fig. 2.1), and thus hindering the transfer. Figure 2.4 shows the effects of transferring the Au-MSA cluster in pH 3.2, 5.5, and 7.8.

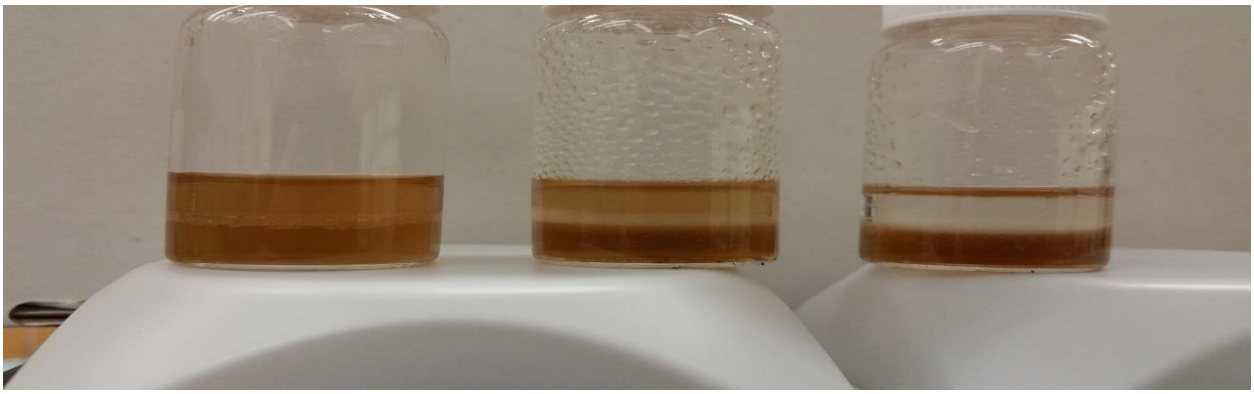

Figure 2.4. Visual representation of the amount of Au-MSA that transferred in pH 3.2 (left) 5.5 (mid) and 7.8 (right).

The transfer efficiency profile of the Au-LA clusters is highest near pH 8. This can be partially accounted for by the more basic pKa of free lipoic acid at 4.7 than MSA.[25] Another unique aspect of the LA is the hydrophobic portion which makes the overall monolayer lipophilic. The Au-LA clusters and lipoic acid itself start to precipitate in aqueous solution around pH 6 due to the protonation of LA COOH and hydrophobicity. In the presence of toluene during the transfer, significant micro/emulsion is formed at lower pH (around 6). Apparently the clusters with partially protonated LA ligands served as surfactants at water/oil interface. The loss of a clear phase boundary limits the evaluation of transfer efficiency toward more acidic pHs. Unlike Au-MSA clusters that can't be transferred at basic pHs, the hydrocarbon portion and single COO- group per ligand is clearly facilitating the transfer at more basic pH up to 10 until stability becomes a concern.[25, 111]

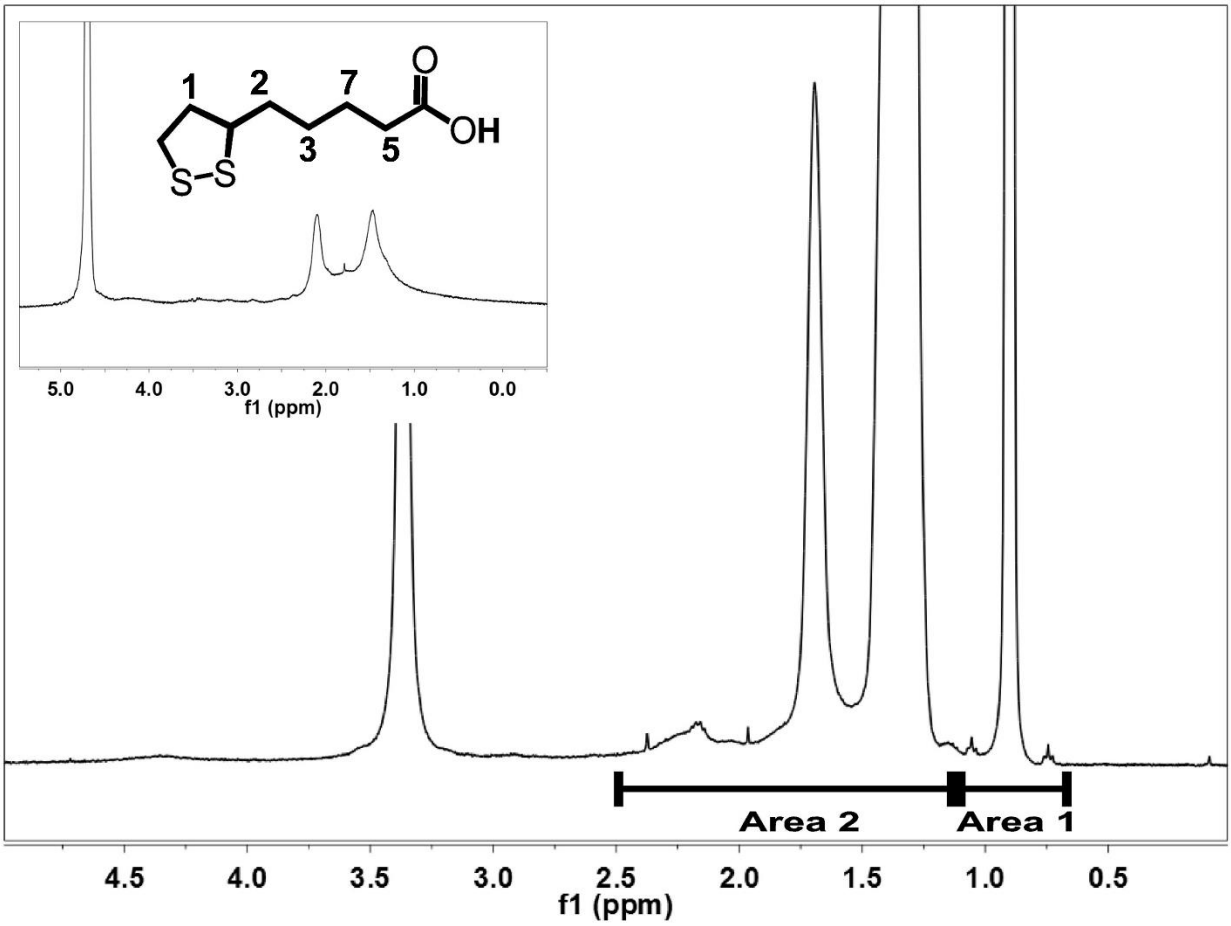

Figure 2.5. ^{1}H NMR of the Au-LA clusters in $CDCl_3$ transferred with stoichiometry ratio of TOA^+. The four major peaks are from TOA^+ (0.9, 1.3, 1.7 and 3.3 ppm). Inset is the Au-LA clusters in D_2O. Area 1 (peak at 0.9) corresponds to CH3 groups from TOA^+ (12 protons), while area two include the sum of 48 protons from TOA^+ and 10 from LA^-.

The transferred Au clusters are characterized by proton NMR (Figure 2.5). The amount of TOA^+ added during transfer was controlled to be low so that some Au-LA clusters remained in aqueous phase. In theory this allows the determination of stoichiometry ratio of charges on cluster to TOA as counter ions in organic phase. A ratio of 1: 2.7 LA ligand to TOA^+ was estimated due to 1. the overlap of high TOA signals and 2. the line broadening effects of the LA ligands on Au core, which leads to lower LA signals, the apparent higher TOA over LA is considered acceptable being within the same magnitude. Further, baseline absorbance in UV-

visible absorption suggests negligible scattering and rules out surfactant-type assembly such as micro/emulsion. Taken together, the transferred Au clusters are confirmed to form a uniform solution that is critical for the following electrochemical measurements. The MSA ligand proton peaks are completely overwhelmed by the strong TOA peaks and cannot be resolved by NMR thus not presented.

2.2.2 Electrochemistry of the Au_{22} Cluster in H_2O

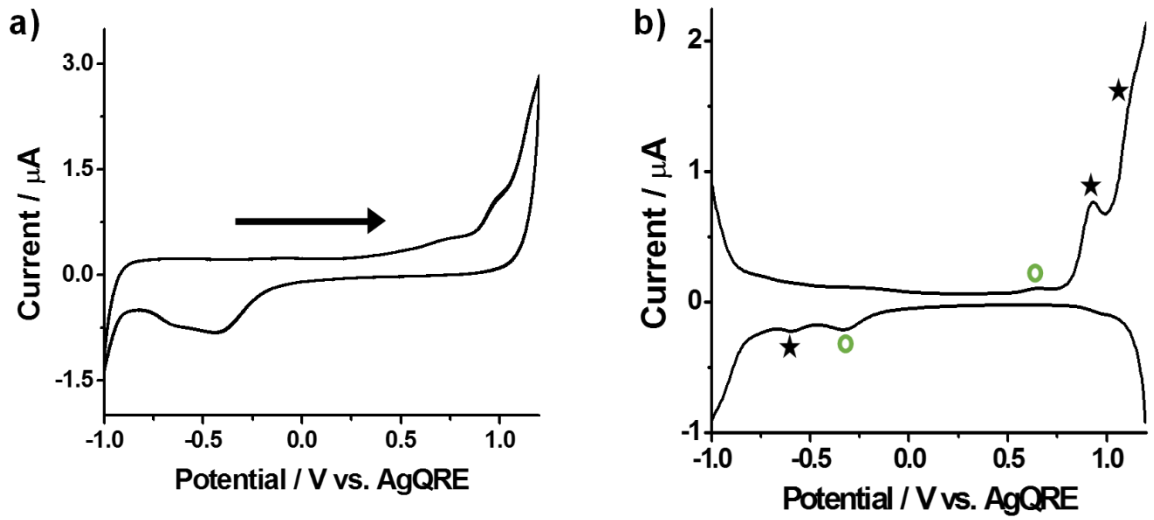

Figure 2.6. Cyclic (a) and differential pulse (b) voltammograms of the Au-LA nanocluster in water. Purging with Ar for 15-30 mins with 0.1 M $NaClO_4$ as the supporting electrolyte. A 0.2 mm platinum disk working electrode, platinum foil counter, and an Ag/AgCl wire were used for all measurements. ***Black stars indicate features attributed to the actual cluster. The green circles indicate a possible oxidation peak at around 0.65 V and a reduction peak attributed to oxygen at around -0.3 V****.*

Electrochemical properties of the Au_{22}-LA_{12} clusters before and after phase transfer is shown in Figure 2.6 and 2.7 respectively. Some redox activities can be observed within the aqueous potential window. The main features include an oxidation peak at + 0.93 V along with reduction peaks at - 0.32 V and -0.60 V. Those redox activities are clearly irreversible also

shown in CV. The reduction around -0.32 V, however, is very close to oxygen reduction even though extensive purging were performed. A HOMO-LUMO gap of 1.53 eV is obtained (+0.93 - -0.60V) accordingly. The gap is qualitatively in line with those from $Au_{25}SR_{18}$ clusters through organic measurements. An additional oxidation at + 1.13 V and a possible reduction below 1 V can be resolved in DPV that are significantly affected by background current. The intensity of the redox peaks, particularly the oxidation around + 0.66 V could vary from batch to batch and decrease over time for a given batch, which is attributed to the partial oxidation of lipoic acid on Au22 over time under ambient conditions as characterized in previous report.[25] The clusters were then purified to remove the electrolyte, phase transferred with TOABr into toluene, then dried and redissolved in appropriate organic solvent for voltammetric study.

2.2.3 Electrochemistry of the Au22 Cluster in ACN

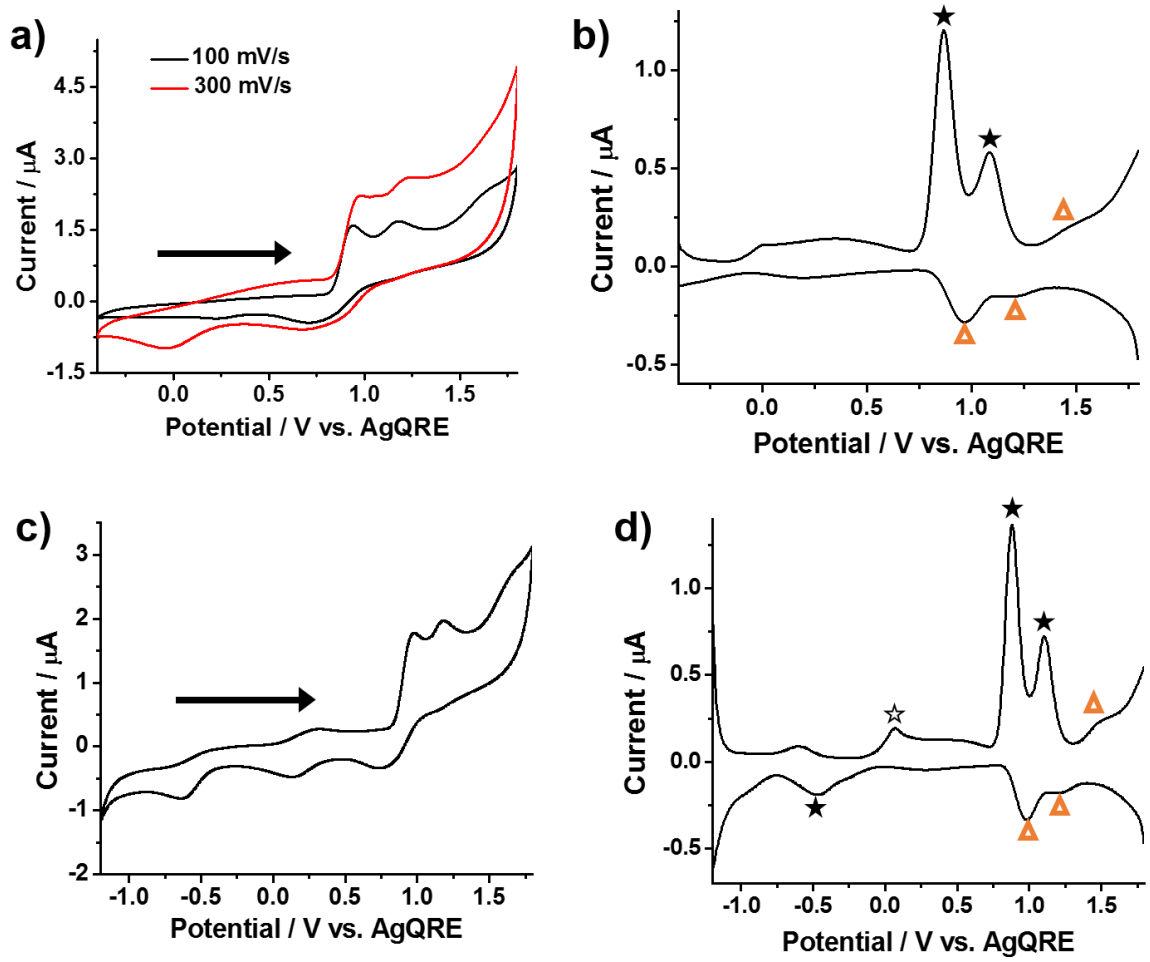

Figure 2.7. Cyclic (a, c) and differential pulse (b, d) voltammograms of phase transferred Au-LA clusters at different potential ranges. Results measured in dry acetonitrile with 0.1M TBAP as electrolyte after purging with Ar for 15-30 mins. A 0.2 mm platinum disk working electrode, platinum foil counter, and an Ag/AgCl wire were used for all measurements. ***Orange triangles represent oxidation/reduction peaks not seen in aqueous measurements.***

Rich redox activities are better resolved with the larger potential window in acetonitrile shown in Figure 2.7. A pair of oxidation peaks at 0.868 V and 1.088 V resembles the HOMO state of molecular clusters. The peak spacing corresponds to a charging energy of 0.22 eV which is slightly smaller than Au_{25} with PET or C6 monolayer at comparable core sizes. The result is expected considering the sparser ligand coverage and thus thinner monolayer based on

concentric sphere capacitance model. No redox activity was observed if the potential window were limited within about -0.3 V to +0.6 V (Figure 2.8).

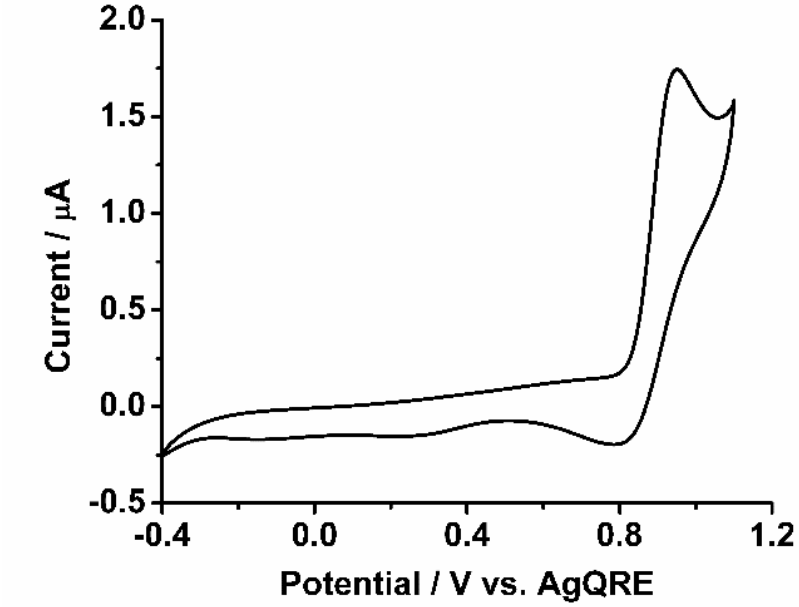

Figure 2.8. Cyclic voltammogram of phase transferred $Au_{22}LA_{12}$ clusters from -0.4 V to 1.1 V. Results measured in dry acetonitrile with 0.1M TBAP as electrolyte with purging with Ar for 15-30 mins. A 0.2 mm platinum disk working electrode, platinum foil counter, and an Ag/AgCl wire were used.

However, if scanned to higher potentials (i.e. beyond +1V or -1V), additional redox activities can be observed in this range, particularly the reduction peak in panel c and oxidation peak in panel d near 0 V. They are attributed to the reversal processes after the corresponding irreversible ET activity at higher potentials (i.e. beyond ±1V. See Figure 2.8 and 2.9). The oxidative desorption feature at around 0.17 V is better illustrated in the square wave voltammograms in Figure 2.9. The peak is more prominent after the -1.2 V reduction and disappears if the reduction is limited to -0.4 V.

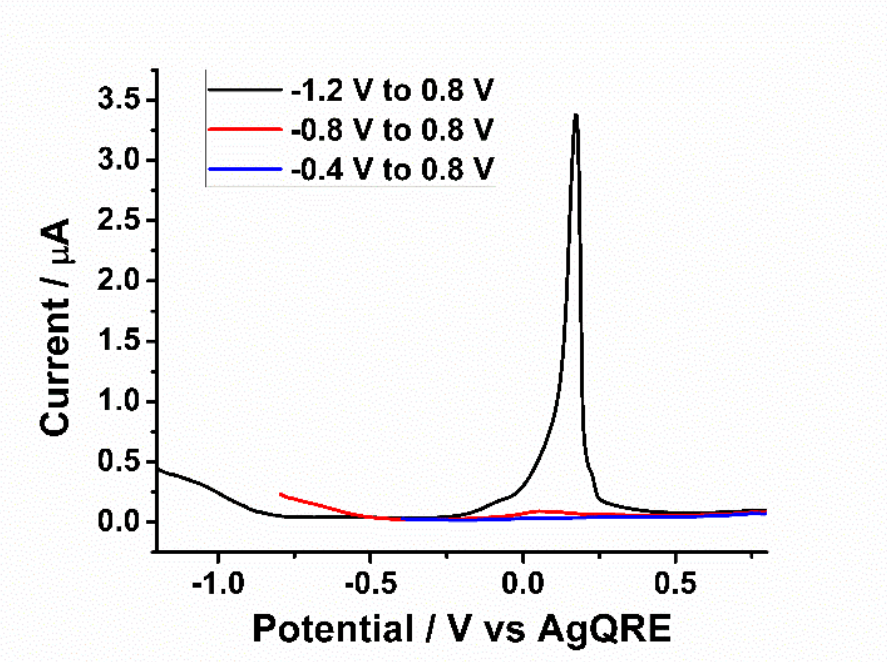

Figure 2.9. Comparison of square wave voltammograms of the phase transferred $Au_{22}LA_{12}$ clusters in acetonitrile. Results measured in dry acetonitrile with 0.1M TBAP as electrolyte with purging with Ar for 15-30 mins. A 0.2 mm platinum disk working electrode, platinum foil counter, and an Ag/AgCl wire were used.

The HOMO-LUMO gap of the $Au_{22}LA_{12}$ clusters in acetonitrile is determined to be 1.34 eV (+0.87 to -0.47). Figure 2.10 illustrates the reduction to a LUMO state that is independent of pre-existing oxidation step. Those features around 0 V corresponding to the reversal processes indicate the stability of the redox products at different charge states. Specifically, in panel a, a reversal reduction peak near 0 V approaches comparable current amplitudes to the one around 0.8 V at higher scan rates, which is about half of the first oxidation peak current. The results suggest a relaxation process after the +0.87 V oxidation. Interestingly, the reduction peak at –0.47 V has a current amplitude that is also about half of the first oxidation peak. The results suggest the Au_{22} being an anion species, so that a 2e oxidation does not require a charging energy. There appears to be two degenerated HOMO orbitals that split upon further oxidation, which corresponds to the second oxidation peak at 1.09 V and another one at 1.48 V. Two

reversal reductions can be observed at 1.22 V and 0.97 V suggesting quarsi-to-irreversible processes that might involve chemical or structure changes to be determined in future studies. The disappearance of the reduction around zero in DPV (slower) that is better resolved in CV at a faster scan rate further suggest an irreversible change of the oxidized clusters. Again, more negative potentials are avoided because the oxidation features near 0 V shown in panel c&d would intensify presumably due to either instability or poor solubility upon further reduction. Better synthesis and isolation to obtain more uniform clusters are underway to better characterize this new dithiolate Au clusters.

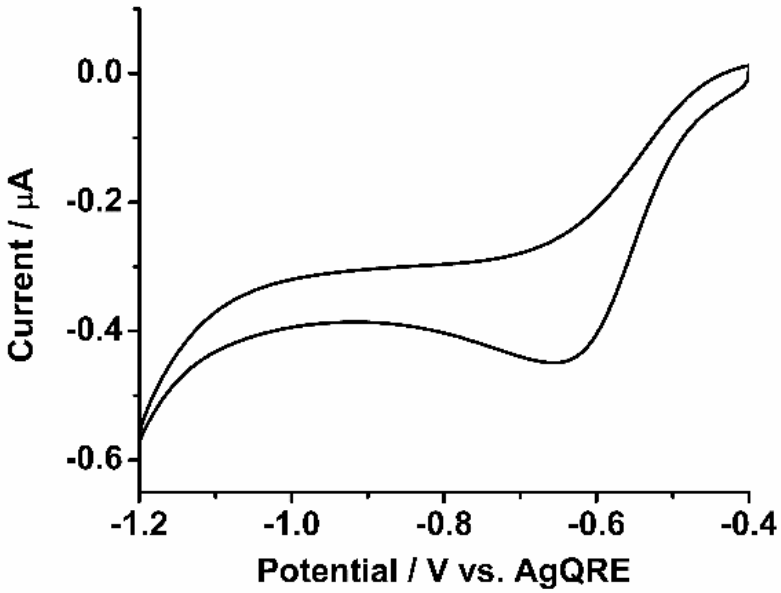

Figure 2.10. Cyclic voltammogram of phase transferred $Au_{22}LA_{12}$ clusters in acetonitrile from -1.2 V to -0.4 V Results measured in dry acetonitrile with 0.1M TBAP as electrolyte with purging with Ar for 15-30 mins. A 0.2 mm platinum disk working electrode, platinum foil counter, and an Ag/AgCl wire were used.

2.3 Experimental

2.3.1 Chemicals

All chemicals (99% or higher) were purchased from Aldrich. Toluene was purchased from Fisher-Science, and nanopure water was produced in-house (>18 Mcm-1).

2.3.2 Instruments

UV-Vis spectra were recorded with a Shimadzu UV-1700 spectrophotometer. NMR spectra were collected with a Bruker NMR 400 MHz spectrometer. Electrochemical measurements were performed on a CH Instruments (CHI 750C) with Picoamp booster in Faraday Cage. The solution was generally purged over 15-30 mins with Ar prior to electrochemical measurements. The potential of the AgQRE (0.22 V vs. SHE) was calibrated periodically by measuring the ferrocene (Fc+/Fc) redox peak at 0.48 V.

2.3.3 Au-MSA Synthesis

Synthesis followed a previously published report on the Au-MSA nanoclusters.[13] Briefly, $HAuCl_4$ was dissolved in 10 mL of a 1:6 mixture of acetic acid and methanol and mixed with a 20x MSA solution dissolved in 10 mL of the acetic acid and methanol. The mixture was stirred until turning colorless. The solution was then placed into an ice bath until the temperature equilibrates. Next a freshly prepared ice cold solution of 20x $NaBH_4$ in 10 mL of nanopure water was quickly added under rapid stirring causing the solution to quickly turn dark. After 3 hours the solution was rotavaped and purified by dialysis for 3 days using snakeskin dialysis tubing (3500 MWCO, Thermo Scientific). Once purified the sample was annealed with 10x MSA for 24 hours at 50^{o}C under mild stirring. The final product was then purified using the previous method.

2.3.4 $Au_{22}LA_{12}$ Synthesis

Synthesis followed a previously report on Au-LA nanolcusters.[11] Lipoic acid was first dissolved in water at a slightly basic pH due to solubility issues. The lipoic acids solution was then mixed with $HAuCl_4$ for a final mole ratio of 3:1 lipoic acid to gold. Additional NaOH was then added to adjust the final solution pH to 11 and stirred for 4 hours. A 2x solution of $NaBH_4$ was then quickly added at room temperature and the reaction was allowed to react for 20 hours. The crude clusters were then purified with dialysis for 3 days using the snakeskin dialysis tubing.

2.3.5 Phase Transfer

During a typical transfer of the clusters, an approximate stoichiometry amount of TOABr was used so there would be no significant excess TOA^+ in solution when performing future electrochemical experiments or ^1H NMR. A mild shaking was sufficient for Au-MSA transfers while centrifuge was necessary to re-establish the phase boundary in the transfer of Au-LA clusters.

2.4 Summary

In summary, phase transfer between aqueous and organic phase is achieved by adopting appropriate pH and reagent with solvent-compatible co-ions and counter-ions using two types of Au clusters. For the Au-MSA clusters featuring highly hydrophilic monolayer, a pH of 3-5 has the greatest transfer efficiency that is close to ligand pKa. The Au clusters with a lipoic acid monolayer, more lipophilic with a terminal COOH group and a hydrocarbon chain, are best transferred under basic pH. Microemulsion formation at acidic pH and cluster stability at more basic conditions are limiting factors for the transfer. CV and DPV analysis suggest the $Au_{22}LA_{12}$ clusters to be anionic and have a HOMO-LUMO gap of 1.34 eV in acetonitrile. A 0.22 eV charging energy is measured after the third electron oxidation that splits the degenerated HOMO

orbitals. Further improvement in the synthesis and isolation is needed to better characterize the cluster itself and those irreversible electrochemical activities.

This chapter is adapted with permission from ChemElectroChem, 2016, 3, 1201-1205. Copyright 2016 John Wiley and Sons.

3 ELECTRONIC TRANSITIONS IN HIGHLY SYMMETRIC AU130 NANOCLUSTERS BY SPECTROELECTROCHEMISTRY AND ULTRAFAST SPECTROSCOPY

Rich and discrete energy states in gold nanoclusters enable different combinations of electronic transitions and correspondingly electrochemical and optical properties for a variety of applications. The impacts on those electronic transitions by the emergence and magnitude/alignment of a band gap and by the contributions from different atomic/molecular orbitals require further study. Au nanoclusters with 130 core Au atoms are of the interest in this report because they are at the transition size regime where a small, yet well-defined band gap can be resolved along with continuous quantized frontier core orbitals. Here, electrochemical analysis is combined with UV-visible-near Infrared optical measurements to unveil previously unresolved electronic transitions. Finite changes in steady-state optical absorption spectrum are captured by spectroelectrochemistry when the Au nanoclusters are charged to different states via electrolysis. Multiple previously unresolved peaks and valleys as well as isosbestic ‘points/regions’ are observed in the differential spectrum. The detailed spectral features are explained by the respective electronic transitions to those affected energy states. Key features are also well-correlated with ultrafast absorption analysis which provides additional insights such as the lifetime of the

corresponding transitions. The experimentally measured energy states and transitions could serve as references for future theoretical study to learn the respective contributions from different atomic orbitals, and importantly, to explore routes to enhance or suppress certain transition so as to modulate the corresponding electrochemical and optical properties for better applications.

3.1 Background and Strategy

Noble metal nanoclusters have been one of the principal topics in nanoscale research due to their composition/size/valence dependent optical, electrochemical, magnetic and other properties.[10] The metal core size is generally a few nanometers or less, energy diagram-wise in the transition regime from atoms/molecules to plasmonic metals.[122] The covalent nature of the stabilizing ligands with the metal cores, particularly in Au-thiolate nanoclusters, allows the elucidation of a definitive composition and the quantification of surface functional groups. It also renders them with greater long-term stability over those by physical adsorption for better applications in complex environment such as biological systems. The tunable physicochemical properties combined with the quantifiable surface functions make them applicable in fields such as bioimaging, sensing and energy along with many others.[4, 123-124] Although the unique merits of these prototypes to establish structure-property correlation are widely recognized, compelling applications enabled from the gained fundamental insights remain to be demonstrated. Further studies are needed to address basic questions such as how to improve an interested property targeting a specific application based on the unprecedented atomic precision compositions and structures elucidated.

Several Au_{130} nanoclusters have been reported stabilized by structurally-comparable thiolate ligands: an aromatic ring directly bonded to the thiol (-SH) in *p*-methylbenzenethiol (*p*-

MBT), an ethyl linker in between in phenylethanethiol (PET), and a mixture of PET and Durene-dithiol in which a CH_2 spacer separates the aromatic portion from the thiol and thus decouples the electron resonance.[9, 72, 125-127] Because the atomic orbitals of both Au and S contribute to the superatom electronic structures of the Au-thiolate nanocluster,[110] the differences among those three Au_{130} nanoclusters could reveal the impacts by the remaining ligands (other than S) on their properties. A prerequisite to tackle such a daunting problem is establishing their respective energy diagrams with fine details for comparison.

Electrochemistry and spectroscopy are major experimental tools that have captured various electronic transitions in thiolate stabilized Au nanoclusters, also referred as monolayer protected clusters in earlier literature.[105] Discrete energy states are characterized by absorption peaks in UV-vis-near infrared region, as well as redox peaks in the corresponding potential/energy window. In those Au-thiolate nanoclusters with clearly separated occupied and unoccupied orbitals/states, photoluminescence (PL) in near infrared region after ground state absorption has been found to have large Stokes shift and up to hundreds nanoseconds lifetime.[128-129] The significant research interest in the near IR PL is due in part to the merit of less spectral interference and thus potential for better bioimaging and sensing applications. Recently, the discrete energy states in Au nanoclusters are also found to enable strong electrochemiluminescence, ECL, in which luminescence is activated by electrode reactions instead of photons from a lamp or laser.[62-63, 130-132] At increased sizes yet smaller than plasmonic nanoparticles such as Au_{146}, continuous quantized double-layer (QDL) charging behaviors are characteristic electrochemical properties while near IR luminescence (both PL and ECL) diminishes associated with the decrease of the band gap.[105] Non-radiative decay pathways will affect the efficiency of the luminescence, which

will likely require the consideration of vibrational modes, both core atoms and ligands, especially in those nanoclusters with small band gaps.[133-135]

A better understanding on the energy states and the related charge/energy transfers is obviously a key to improve the properties such as ECL and PL of nanoclusters. Spectroelectrochemistry, also under electrochemical controls like ECL, measures the changes in optical absorption after an orbital/state is oxidized or reduced.[34, 44, 73, 106, 111, 136] Unlike transient optical absorption spectroscopy in which the population of electrons in different energy states is modulated by a pump laser without changing the charge of the sample, spectroelectrochemistry allows electrons or holes to be selectively introduced in an energy state by an electrode at the appropriate potentials. In the Au_{130} with mixed PET and Durene-dithiols, differential spectrum shows detailed electronic transitions otherwise inaccessible after charging to different core and ligand energy states.[32] More specifically, electron relaxations from core states after the oxidation of the ligand orbitals were clearly resolved. While spectroelectrochemistry combines steady-state optical measurements with electrochemical techniques under the conditions more relevant to i.e. ECL generation, transient optical measurements up to femtosecond resolution allow one to characterize the electron dynamics of short-lived excited states in the photoactive gold nanoclusters. The excited state absorption (ESA) and ground state bleaching (GSB) in the transient absorption spectrum as well as the decay components and lifetimes of these excited states provide valuable insights in smaller Au nanoclusters including Au_{25}, bimetallic Pd/Pt doped M_1Au_{24}, and the various larger nanoclusters. [137-143]

In this chapter, the Au_{130}(*p*-MBT)$_{50}$ nanoclusters are studied in the interest of the known core atomic structure and the simplicity of the ligand molecular structure.[72] Continuous quantized charging, toward both oxidation and reduction potentials, is separated by a 0.5 eV

electrochemical gap. The four broad steady-state absorption bands are found to involve multiple transitions from different energy states unveiled through spectroelectrochemical study. Combined with ultrafast measurements that report the lifetime of several key excited state processes, an energy diagram is proposed that successfully explains key optical features.

3.2 Results and Discussion

3.2.1 Basic Electrochemistry Features

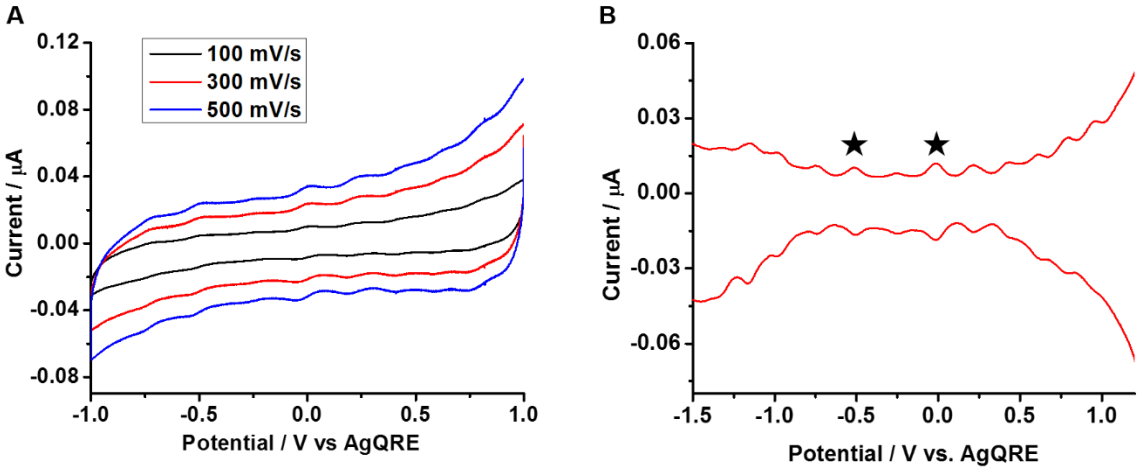

Figure 3.1. (A) Cyclic voltammograms (CV) at different scan rates and (B) square wave voltammograms (SWVs) of the Au_{130} nanocluster. The electrochemical gap is highlighted by the stars in SWV. Results measured in dry CH_2Cl_2 with 0.1M TBAP as electrolyte after purging with Ar for 15-30 min. A 0.2 mm platinum disk working, platinum wire counter, and an Ag/AgCl wire reference electrode were used for all measurements.

Well-defined QDL features are observed as shown in Figure 1. Comparable current amplitude of those redox peaks is seen in CVs at a given scan rate. A potential gap of 0.50 V, from -0.51 V to -0.01 V, is highlighted in SWV. Uniform QDL's with an average peak spacing of 0.21 V are present on both positive and negative sides of this 0.5 V potential gap. Table 3.1 summarizes the QDL peak potentials along with the spacing, i.e. charging energy (eV).

Table 3.1. Potential and peak spacing of the main QDL features of the Au_{130} cluster. The peak spacing values are calculated by subtracting the neighboring (Right-Left) values in the row

above. Highlighted peaks represent the 0.5 V band gap discussed. The open circuit potential (OCP) during the time of these measurements was 0.0 V.

Oxidation (V)	-1.32	-1.15	-0.97	-0.74	-0.51		-0.01	0.21	0.42	0.6	0.79	0.96
Peak Spacing		0.17	0.18	0.23	0.23			0.22	0.21	0.18	0.19	0.17
Reduction (V)	-1.33	-1.15	-0.97	-0.73	-0.51		-0.01	0.22	0.43	0.62	0.78	0.96
Peak Spacing		0.18	0.18	0.24	0.22			0.23	0.21	0.19	0.16	0.18

The charging energy is consistent with that from other previously published Au_{130} sized clusters with similar ligand monolayers.[32, 125] The peak separation is about 60 mV for each oxidation/reduction QDL pair in the CVs at varying scan rates shown, meaning that these processes are electrochemically reversible. A small peak is seen in the band gap, at -0.27 V between the two QDL's, but is significantly smaller than the rest of the peaks in both CV and SWV. Its weak intensity also varies in different samples and decreases over time for a given sample. Further, the open circuit potential (OCP) is found to be close to 0.0V for a freshly synthesized sample and shift to more positive over time under ambient conditions, i.e. 0.18V for the sample used in spectroelectrochemistry analysis. Accordingly, the weak peak in the gap is attributed to trace amount of impurity or Au_{130} at more oxidized charge states discussed later. The QDL features of the aged sample at different temperatures can be seen in Figure 3.2. A small potential window was used to resolve the QDL peaks with high gain/sensitivity. The band gap increased to about 0.54 V while the average peak spacing remains comparable to the room temperature one. The redox reversibility in the QDL range is further attested by the matching oxidation and reduction scans. Toward more positive potentials, a single oxidation peak at + 1.46 V is observed on top of significant background current in both CV and pulsed voltammetry measurements (not shown).

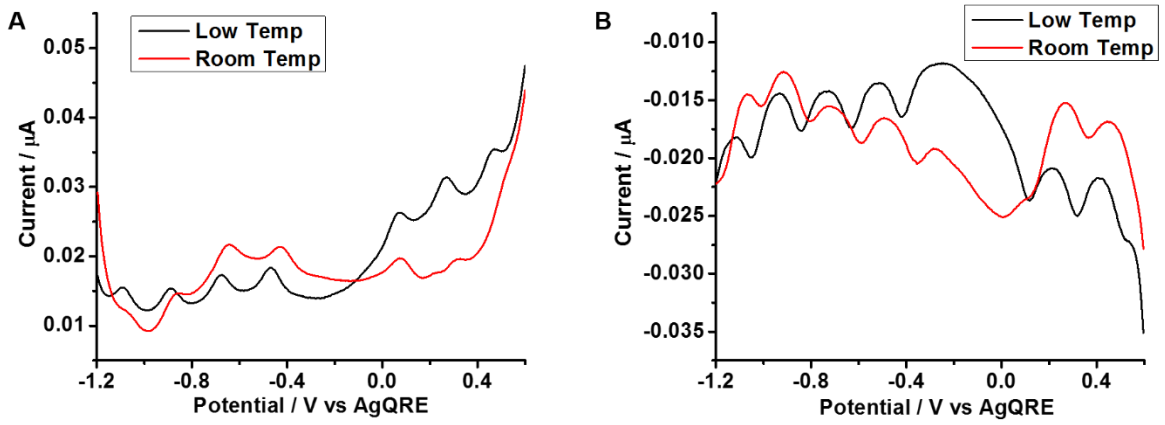

Figure 3.2. (A) DPV during oxidation of the aged Au_{130} sample. (B) DPV during reduction of the aged Au_{130} sample. Results measured with 0.1M TBAP as electrolyte with purging with Ar for 15-30 mins. A 0.2 mm platinum disk working electrode, platinum foil counter, and an Ag/AgCl wire were used. Low temperature measurements were done in a mixture of dry ice and ethanol (-72ºC). OCP during the time of these measurements was 0.18 V.

The redox activities involving ligands, especially the sulfur orbitals in Au-S bonding, are measured in mixed toluene: acetonitrile (Tol:ACN) which allows a larger potential window without significant solvent reactions. The results are included in Figure 3.3. As ultrafast spectroscopic data were collected in toluene as solvent, 10:1 Tol/ACN were used to be more consistent for comparison (a small amount of ACN is needed to dissolve electrolyte). The band gap, OCP and continuous QDL charging are consistent with those in CH_2Cl_2 and can still be measured at a smaller potential window with higher gains, albeit the features become far less defined. Toward more positive, a distinct oxidation peak around 1.4-1.5 V is clearly seen in CV. At a slightly higher scan rate, the peak shifts to more positive and the reversal reduction is better captured at around 1.0-1.1 V, indicating the irreversible nature of this oxidation process involving the Au-S bonding. In addition to the one at 1.42V corresponding to the CV feature, two oxidation peaks at around 1.20 V and 1.51 V are resolved by differential pulse voltammetry (DPV) in which the reversal reduction scan shows a very broad weak band in this potential

range, again suggesting irreversibility. On the reduction side, other than the possible residual oxygen signals around -1V (absent in CH_2Cl_2 as solvent), there is a reduction band beyond -1.9 V shown in DPV.

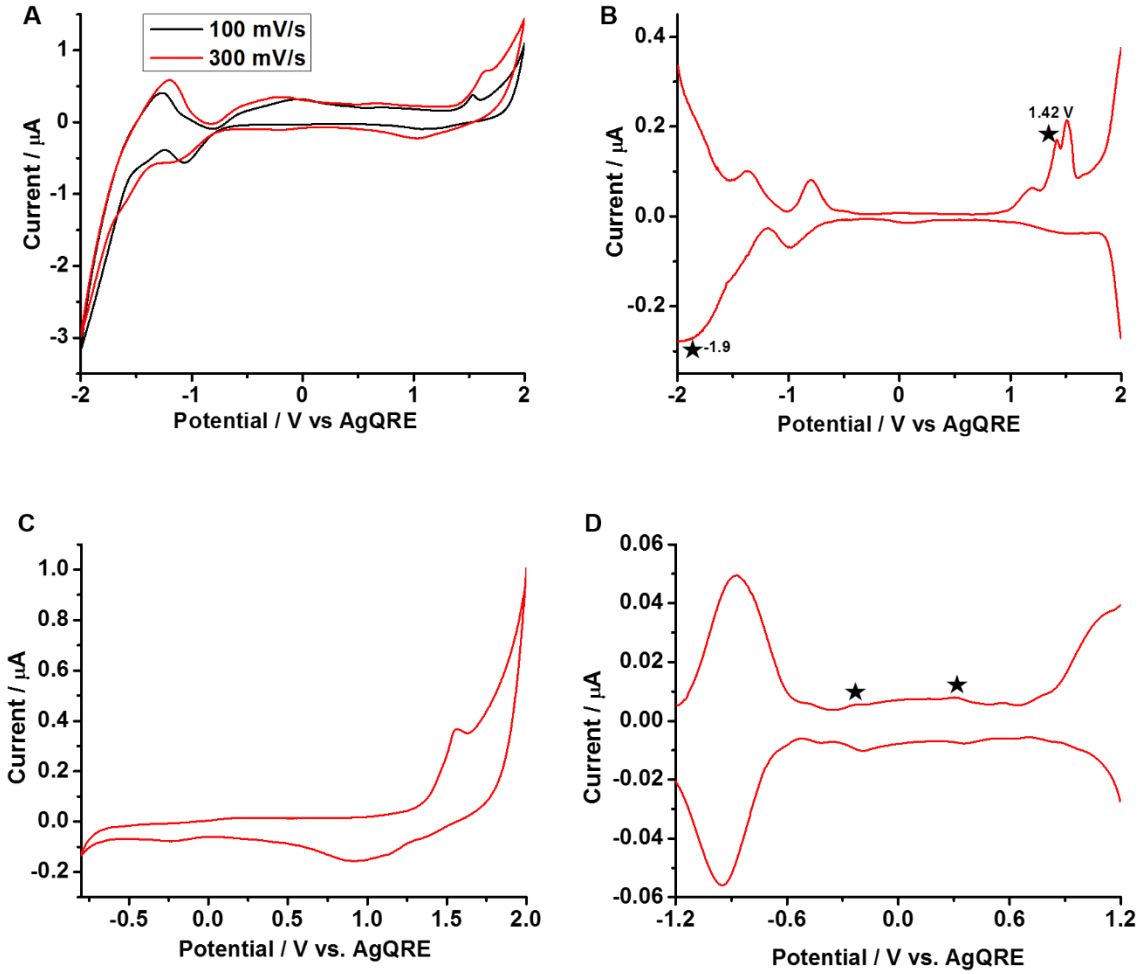

Figure 3.3. CV and DPV of Au130 nanoclusters in 10:1 Toluene:Acetonitrile. (A) and (B) scan a large potential window as overview. (C) includes a less negative potential range (-0.8V) to show the largely featureless oxidation in QDL region and the reversal reduction features around +1.0V and -0.2V. Black stars in (D) highlight the 0.5 V gap consistent with the measurement in CH_2Cl_2. Results measured with 0.1M TBAP as electrolyte with purging with Ar for 15-30 mins. A 0.2 mm platinum disk working electrode, platinum foil counter, and an Ag/AgCl wire were used. OCP during the time of these measurements was 0.18 V.

There are major differences between this highly symmetric Au_{130} with *p*-MBT ligands and the previously reported Au_{130} with a dithiolate Durene as ligands. Near IR photoluminescence is not detectable with *p*-MBT as ligands, but has been reported from the Au_{130} with Durene ligands.[127] Regarding the electrochemical properties, there is much weaker reversal reduction observed, if any around the frontier QDL states, i.e. around -0.2-0.0 volts. Further, the anodic current of the 1.42 V peak is not significantly larger than the QDL peak, for example by a factor that correlates with the number of ligands.[26] The results suggest that the remaining portion of ligands other than S atom is not involved in the electron transfers. The inertness of *p*-MBT, unlike the durene-dithiol/ates in which radical cations can be formed on Durene upon oxidation,[26] is believed to be responsible for such differences.

To demonstrate the distinct redox features at higher potentials include both Au and S contributions, i.e. Au-S, a mixture of 1:1 $HAuCl_4$:*p*-MBT was tested in the same 10:1 Tol:ACN mixed solvent system. The CV and DPV results are in Figure 3.4. Multiple redox activities can be seen because the mixture is known to contain Au(I)-thiolate polymeric complexes and disulfides.[144] After the Au(0) core formation upon reduction by $NaBH_4$, the oxidation peaks at 1.00, and 1.57 V shift and diminish in amplitude (CV). The 1.42 V state is the only detectable peak in CV for Au nanoclusters. On the reduction side, a distinct peak at -1.9 V is observed from this mixture instead of the continuous broad band beyond -1.9 V in the nanoclusters, which suggests additional interactions or overlap with other higher energy states such as those from the Au core.[145]

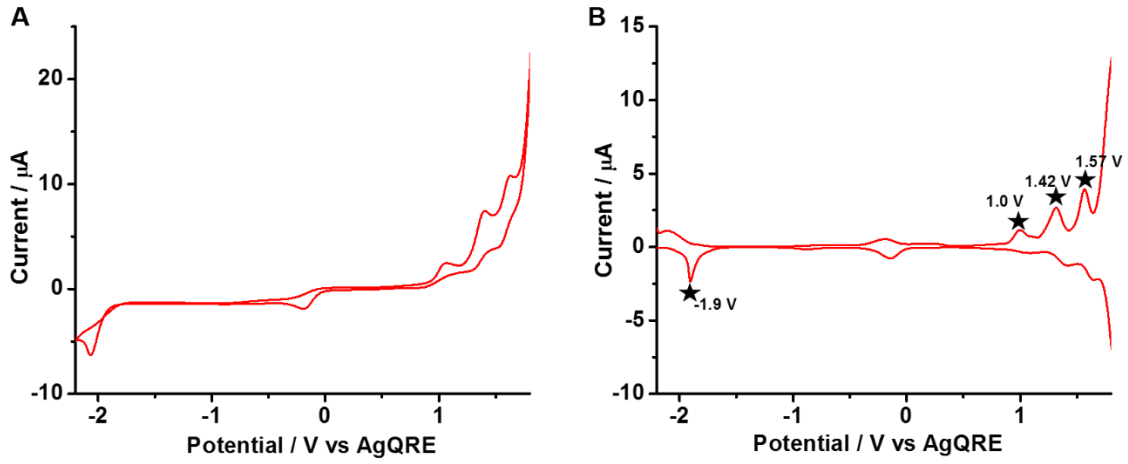

Figure 3.4. CV and DPV of the 1:1 Au:p-MBT mixture in 10:1 Toluene:Acetonitrile. Results measured with 0.1M TBAP as electrolyte after purging with Ar for 15-30 mins. A 0.2 mm platinum disk working electrode, platinum foil counter, and an Ag/AgCl wire were used.

3.2.2 Spectroelectrochemistry Features

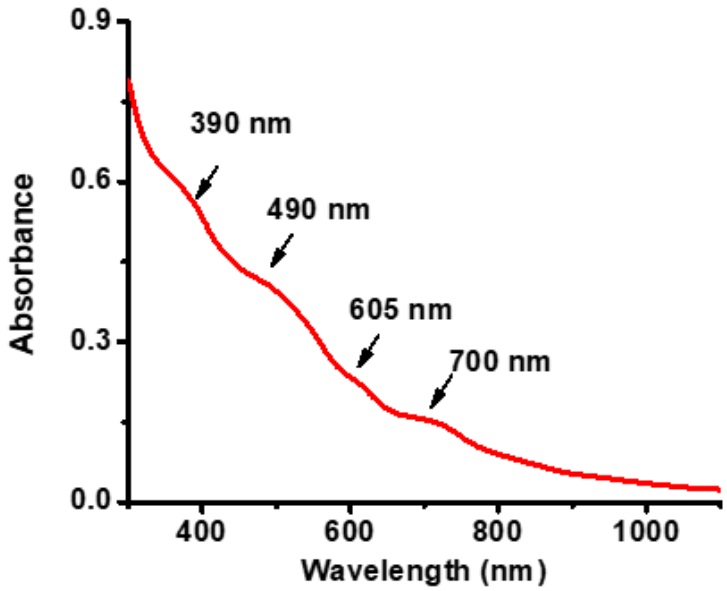

Figure 3.5. Steady-state UV-Vis spectrum of the Au_{130} cluster.

The steady-state UV-Vis spectrum of the Au_{130} nanocluster is included in Figure 3.5. The changes in absorbance after each electrolysis at those denoted potentials are plotted in Figure 3.

The dashed lines represent those four previously reported values of 390, 490, 605, and 700 nm, though each corresponds to a rather broad band/region. This report focuses on the potential range of the reversible QDL features and avoids irreversible ligand reactions. The corresponding original spectra are included in Figure 3.6 for reference. In the remaining sections, spectrum features are described in wavelength with the corresponding transition energy in electron volts (eV) in parenthesis for clarity.

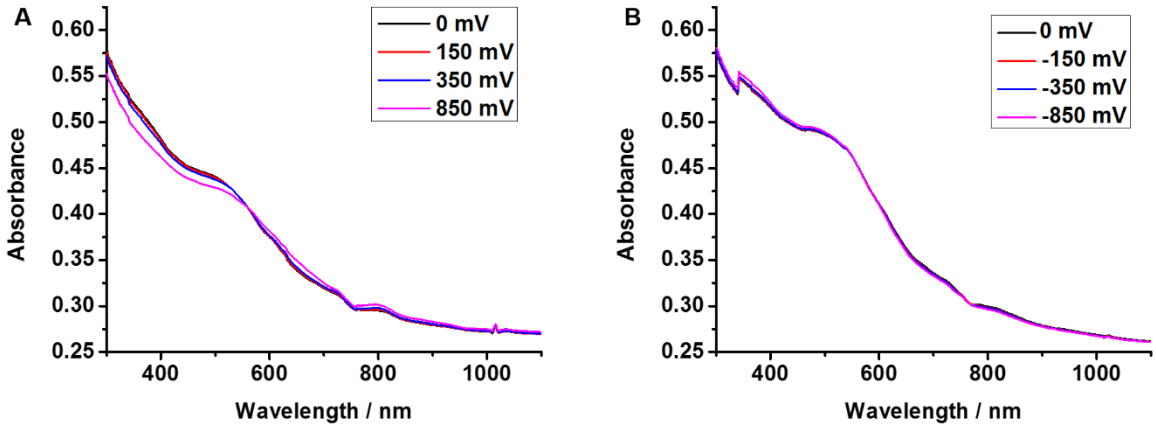

Figure 3.6. Original UV spectra measured after each electrolysis in CH_2Cl_2. The electrolysis stopped after the charging current decrease to about less than 10% original/baseline, typically 5 minutes. These spectra were used to calculate the differential spectra shown in Figure 3.7. The abrupt change at 340 nm is an artifact due to lamp switching.

Overall, reduction (top half of Figure 3.7) and oxidation (bottom half) spectra mirror each other largely. The positive and negative changes indicate the additional and suppressed absorption transitions respectively. The corresponding energy states can be determined accurately from the fine spectrum details (top axis shows eV). The first notion is that the 390 nm band includes the transitions with a max Δabs. at 371 nm (3.34 eV). For this and the steady state band at 490 nm (2.58 eV), both intensities decrease upon oxidation and increase upon reduction. An edge toward lower energy at 530 nm (2.34 eV) is determined by extrapolating the flat baselines of the first two redox/spectra in both panels. At around 560 nm (2.21 eV) a possible

isosbestic point (or zone considering possible small shift of the corresponding states under redox processes) is observed that separates the absorption decrease from the increase in oxidation panel (vice versa in reduction). The steady state band at 602 nm (2.06 eV) is in the middle of a newly observed band, max at 580 nm (2.14 eV) in the oxidation panel and another one to the red at 644 nm. Its high energy edge starts from the isosbestic point of 560 nm. Reduction appears to shift the corresponding energy states and establish an isosbestic zone till a decrease occurs from 600-620 nm. The low energy edge of this band is around 625 nm (1.98 eV), estimated from the reduction valley or the infection point in the oxidation spectrum.

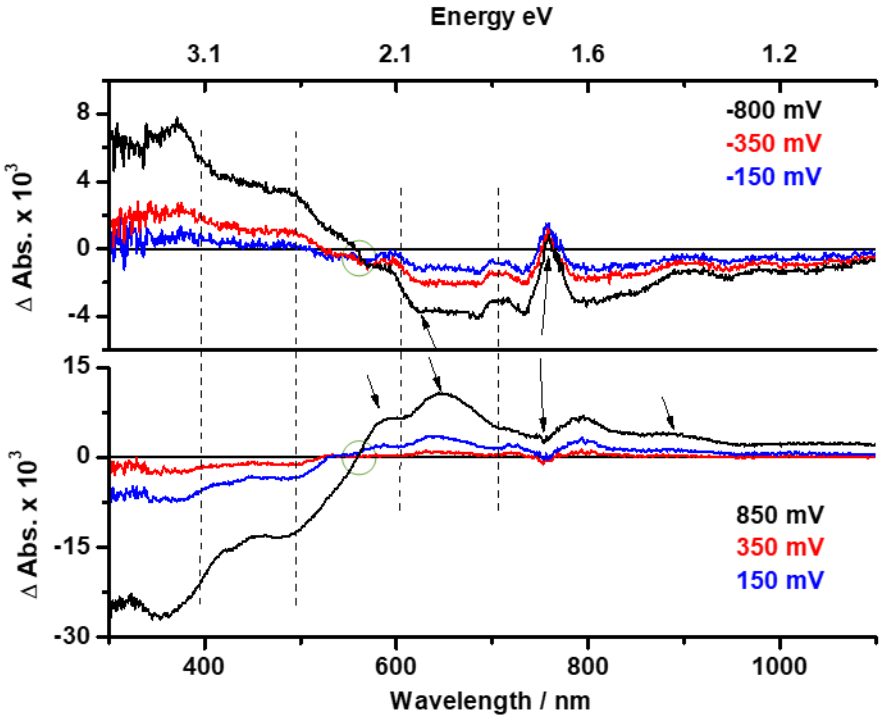

Figure 3.7. Differential spectra after electrolysis under different potentials in CH_2Cl_2. Charging to more positive and negative potentials were performed separately, using the same sample solution split into two, to avoid possible irreversible changes to accumulate over stepwise redox charging. The original spectrum was subtracted from the spectrum collected after each electrolysis. The key spectrum features remain largely unaffected using a spectrum electrolyzed at 0.0 V as baseline. The open circuit potential of this sample at the time of measurement is +0.18 V. In addition to the four ground state abs bands, the green circle at 560 nm highlights the isosbestic transition. Other arrows indicate key emerging features at 580 nm, 644 nm, 755 nm

and 885 nm. The three potentials correspond to the oxidation (+) and reduction (-) of 1/1, 2/2 and 5/4 electrons.

Toward lower energy, a peak at 644 nm (1.93 eV) increases by oxidation while reduction causes broad/flat decreases extending beyond the last steady state band at 710 nm (1.75 eV). In the reduction panel, there appears to be an increase on top of the broad decrease leading to overall unaffected area around 755 nm (1.64 eV). A decrease at the same range is observed over broad weak increase in oxidation panel. A weak band around 885 nm (1.40 eV) increases by oxidation is arguably noticeable. Due to the low absorbance values of the raw spectra and the low ΔAbs. especially at longer wavelength, the discussion is focused more on the qualitative trend and the characteristic wavelengths. One should be cautious when interpreting the absolute positive or negative signs in absorbance changes considering the possible baseline drift during the measurements, batch-to-batch sample variations and overlapping electronic transitions from different energy states. To fully compare the spectroelectrochemical data with the ultrafast results a 10:1 mixture of toluene:acetonitrile was used in later experiments. Absorbance data for this solvent system was compared to what is observed in CH_2Cl_2 in order to rule out any solvent effects. For reference this data is shown in Figure 3.8.

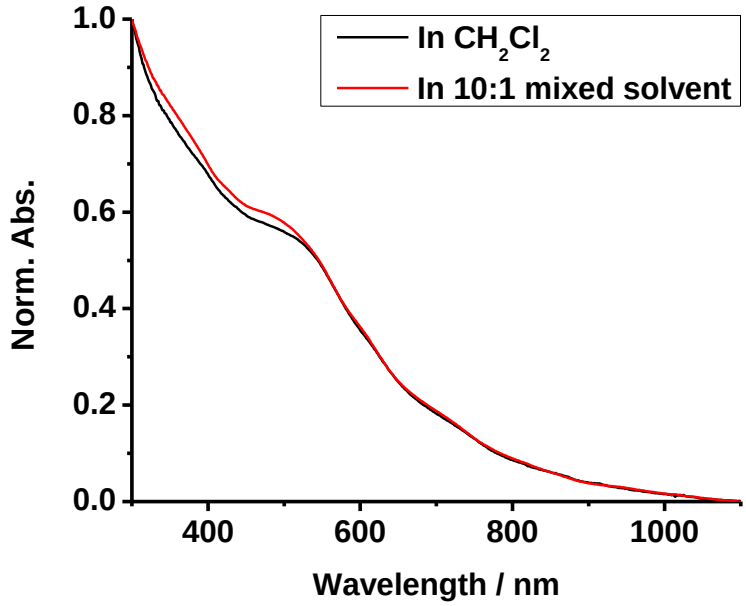

Figure 3.8. Steady state absorbance spectra in both CH_2Cl_2 and the mixed solvent system. Spectra were normalized at 300 nm.

Differential spectra collected from the same sample in mixed solvents for comparison with ultrafast results are presented in Figure 3.9 panel B. Although QDL features are less defined presumably due to solvent penetration into the monolayer, the key spectrum features are consistent with the results collected in CH_2Cl_2. A major difference is that the fine structures in the longer wavelength range in reduction panel are no longer resolved. Further, the results collected from a sample in which the weak mid-gap redox peak (around -0.27 V, Fig. 3.1) is clearly noticeable are also provided in panel A for reference. While the features in the reduction panel are limited and consistent with others, two major differences are labeled in the oxidation panel. The first is a stronger 530 nm band (more positive increases). This seems to distort or shift the isosbestic region to around 600 nm. The other one is a distinct positive band at 743 nm. For an aged sample, it appeared to redshift and broadened (more positive OCP, Fig. 3.8 A).

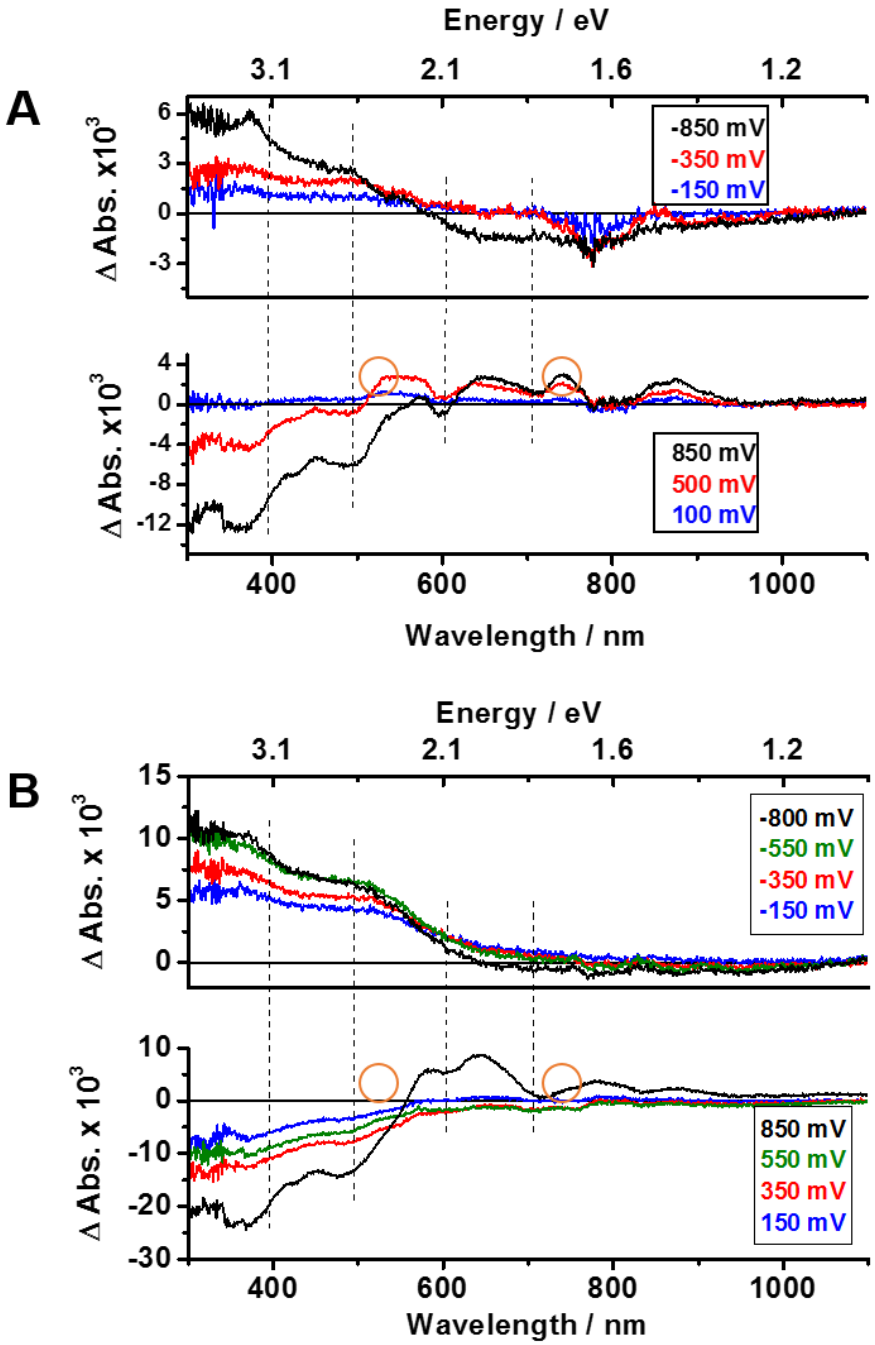

Figure 3.9. (A) Differential spectra after electrolysis in 10:1 Toluene:Acetonitrile. The OCP of the sample used in these measurements was 0.0 V. (B) Differential spectra bias after electrolysis in 10:1 Toluene:Acetonitrile. The OCP of the sample was 0.18 V (the same sample used in Figure 3.5). The orange circles highlight the major differences between the two samples.

3.2.3 Energy Diagram

Those well-resolved electronic transitions are summarized in the proposed energy diagram in Figure 3.13. The conversions between wavelength and electron volts (eV) and related energy calculations comparing the optical and electrochemical results are provided in Table 3.2.

Table 3.2. Calculations of the observed transitions in the differential spectrum in CH2Cl2. The wavelength numbers were read from Figure 3.7. The OCP of the Au NCs used in the measurements was 0.18 V. Bolded blue boxes represent the four steady state features in the UV-Vis spectrum. Calculations directly below each of these areas represent transitions that either directly affect the steady state transition or are located between that steady state and the next. Some transitions (shaded in pink) are shown twice in the table (the second is shown in italics). This is due to those transitions having possible effects on more than one steady state/region in the differential spectrum. The green shaded boxes represent the isosbestic point which splits the differential spectrum into two distinct regions of overall behavior (either overall decreasing or overall increasing with oxidation/reduction).

Differential Spectrum			Electrochemistry			Expected Changes by
(nm)	(eV)	Changes in Δ Abs.	Low E (LE, V)	High E (HE, V)	Transition (LE - HE)	Ox/Red (Inc. +; Dec. -)
371	**3.34**					SS
371	3.34		1.46	-1.90	3.36	Ox (-); Red (+)
490	**2.58**	Oxidation (-)				SS
490	2.58	Reduction (+)	0.29	-2.29	2.58	Ox (-); Red (+)
530	2.34		2.22	-0.21	2.43	Red (-)
			0.08	-2.29	2.37	Ox (-); Red (+)
560	2.21	Isosbestic Point	2.22	0.00	2.22	0
			0.29	-1.90	2.19	0
580	2.14		2.22	0.08	2.14	Ox (+); Red (-)
602	**2.06**					SS
580	*2.14*		*2.22*	*0.08*	*2.14*	*Ox (+); Red (-)*
625	1.98		0.08	-1.90	1.98	Ox (-); Red (+)
644	1.93	Oxidation (+)	2.22	0.29	1.93	Ox (+)
700	**1.75**	Reduction (-)				SS
>700	<1.75		1.46	-0.21	1.67	Red (-)
885	1.40		1.46	0.08	1.38	Ox (+); Red (-)
755	1.64	Red (+)	-0.21	-1.90	1.69	Red (+)

The wavelength numbers were read from Figure 3. The OCP of the Au NCs used in the measurements was 0.18 V. Bolded blue boxes represent the four steady state features in the UV-Vis spectrum. Calculations directly below each of these areas represent transitions that either directly affect the steady state transition or are located between that steady state and the next. Some transitions (shaded in pink) are shown twice in the table (the second is shown in italics). This is due to those transitions having possible effects on more than one steady state/region in

the differential spectrum. The green shaded boxes represent the isosbestic point which splits the differential spectrum into two distinct regions of overall behavior (either overall decreasing or overall increasing with oxidation/reduction).

The potential values on the left in Fig. 3.13 are collected from the exact Au_{130} NC sample used in spectroelectrochemical measurements (Fig. 3.7). The first QDL oxidation peak at + 0.08 V defines the frontier occupied energy states below the band gap. The frontier states above the 0.5 V gap is therefore at -0.42 V. The open circuit potential (OCP) is generally around 0.0 V for freshly synthesized samples but over time shifts slightly more positive, i.e. 0.18V herein. Consider the QDL charging energy of 0.21 V, and the as-synthesized Au_{130} NCs being neutral, the positive shift in OCP is explained by the graduate oxidation through which both neutral and positively charged species coexist. The QDL peaks shift upon oxidation slightly, notably the first oxidation peak from -0.01 V (Fig. 1) to +0.08 V. To be inclusive of data collected from samples with different extent of oxidation, or different ratio of neutral/oxidized species, an additional state separated by one charging energy of 0.21 V is added (on the right). The general assignment of those key transitions is not affected, though the specific calculations need to be adjusted accordingly. Because the rich energy states of the large Au_{130} NCs make some electronic transitions, especially toward low energy range, rather crowded, the differences at tens of milli-electron-Volts between electrochemical and spectroscopic data are believed to be acceptable. Those experimentally resolved finite differences can be employed to evaluate the coupling of vibrational states or structural relaxation in future studies. Further, since the +1.46 V oxidation in CH_2Cl_2 is reasonably close to those measured in mixed solvent (±0.05V), solvent differences are assumed insignificant in the measured potentials. The broad reduction starting at -1.90 V measured in the mixed solvent, not resolvable in CH_2Cl_2, is used in the following analysis. The numbers listed on the right indicate

the range of the corresponding states from different measurements. Additional states such as the -2.29 V and +2.22 V were not measured but back-calculated from distinct spectroelectrochemistry features: the 490 nm (=2.58 eV; + 0.29V – (-2.29V)) is further validated by i.e. 530 nm (= 2.34 eV; 0.08V – (-2.29V)); while the 580 nm (=2.14 eV + 2.22V – (+0.08V)) by the 644 nm (= 1.93 eV; + 2.22V – (0.29V)). The voltage values in parenthesis are electrochemical data.

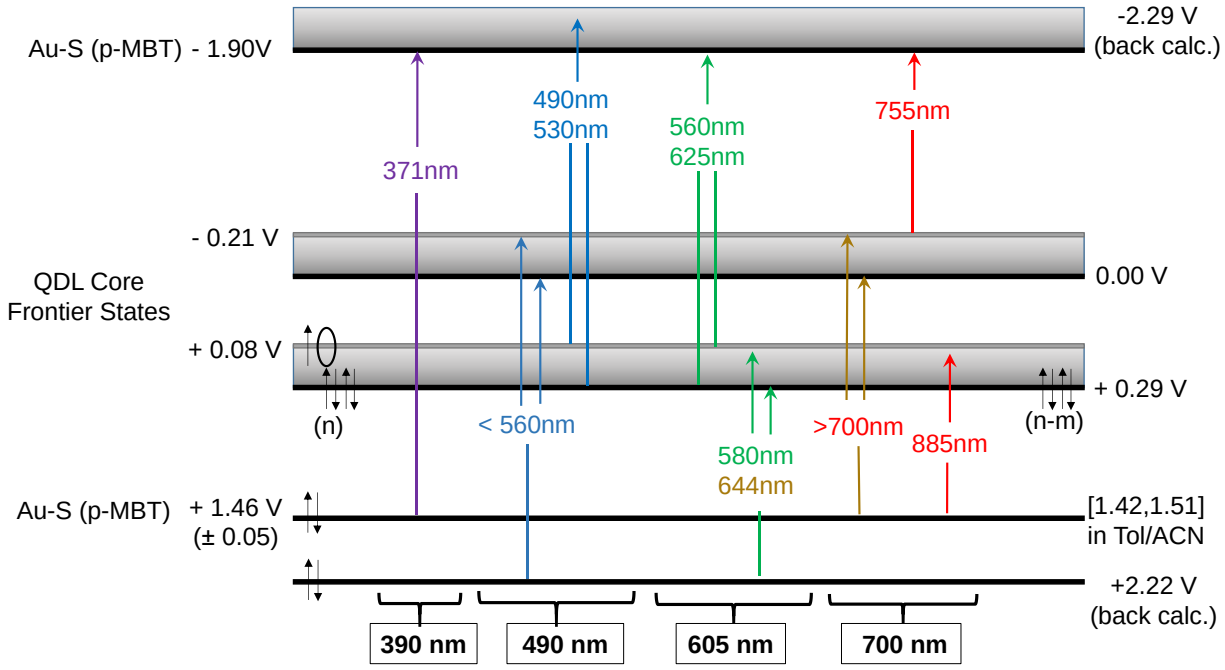

Figure 3.10. Energy diagram for the electronic transitions in Au_{130}(p-MBT) by spectroelectrochemistry. Voltage values listed on the left were directly from the electrochemical measurements (in both solvent systems), those on the right were from a combination of spectroelectrochemical and electrochemical data or back calculated as noted. Color coded wavelengths are used to show spectroelectrochemical features near the four observed steady-state optical peaks. Each wavelength (one arrow) represents a distinct spectrum feature resolved in, i.e. Fig. 3.7. Black arrows are used to represent electrons in each energy state of the freshly synthesized sample (left side) and the oxidation effect of the aged sample (right side). The grey bars in the frontier energy states represent charging energy, and the one on top corresponds to the broad continuous reduction (Fig 3.3).

The detailed structures in the differential spectra can be correlated to and retrospectively account for different combinations of electronic transitions from lower occupied to higher unoccupied orbitals. The assignment reveals that multiple transitions could partially overlap and

cause the broadening of the four native-state absorption bands. The highest energy band (<390 nm) includes the transition between the unoccupied and occupied Au-S (*p*-MBT) orbitals. The transition from highest occupied core frontier states to the states above Au-(*p*-MBT) LUMO (broad reduction band above -1.90 V, Fig. 3.3 & discussions) generates the 490 nm (2.58 eV) absorption band, which could partially overlap with the transition to the unoccupied core frontier states from lower states. The 605 nm (2.05 eV) absorption band is a unique region where the transitions both into and from the partially-occupied core frontier states overlap. The last steady state around 710 nm (1.75 eV) is mainly the transition from the Au-(*p*-MBT) HOMO to the unoccupied core frontier states.

Upon oxidation to different potentials, the electrons in the frontier states would be stepwise removed. Electron transitions from these states (+0.08, +0.29/-0.21V) should decrease, such as the 490/625 valleys in differential spectra and ultrafast GSB bands. Meanwhile, those incoming transitions from states below should increase with the additional accessible states/holes, for example 580/644/730 nm & 885 nm peaks and ESA bands. The very unique isosbestic feature at 560 nm is worth emphasizing, as it separates absorption increase toward lower energy (longer wavelength) and negative Δabs. toward higher energy upon (increasing) oxidation. It suggests that the ground state absorption here originates from the states not directly affected by the oxidation, such as the states immediate below the frontier occupied ones. Additionally, the differential changes could represent the conversion of one transition into another around this point (530/580nm: +2.22→+0.08→-2.29), which is also supported by the reduction features. The detailed assignments and calculations of those transitions are summarized in Table 3.2. Besides the direct impact on the transitions in 490/605 nm range, oxidation has indirect influences on the transitions from the lower states, i.e. +1.46 V captured by different

measurements. The broad negative Δabs. in <390 nm range could be due to the decease of electron relaxations from frontier states (GSB) after the oxidation. Unfortunately, ultrafast data in this energy range is unavailable. Related, the main transitions contributing to the 700nm band are not directly affected by oxidation, which is indicated by the ultrafast results where ESA or GSB is insignificant. The slight variations are attributed to neighboring transitions at slightly higher and lower energies.

Reduction induced features, albeit less defined or consistent among samples/solvents, can be explained similarly. Filling the frontier states (+0.08, then -0.42/-0.50) with additional electrons will reduce the transitions from the lower states to the frontier states (+0.08/-0.21, then -0.42/-0.50). Meanwhile, those additional electrons will cause the transitions to higher states to increase. This is again separated at around 560 nm or 2.21 eV. The absorption remains relatively flat up to about 600 nm due to the shift of the frontier states involved in two transitions (+2.22 to +0.08 & +0.08 to >-1.90) that partially overlap. There should be a new feature corresponding to the electrons in the newly occupied core frontier states, i.e. -0.42/-0.50 V. It is attributed to the peak at 755 nm (1.64 V) in the middle of the broad decrease due to the overwhelmingly crowed transitions in this energy range.

A limitation of the proposed energy diagram is that vibrational energy states are not considered. Both inner Au core atoms and peripheral Au-S shells would have relaxed, and different structures might be responsible for some differential spectra features. The existence of different structures can be inferred from the spectrum differences captured from a fresher (less positive OCP) sample shown in Fig. 3.9. There is a distinct band at 743 nm (1.67 eV) increases up to 5-e oxidation, which is either broader and red-shifted or absent in an aged sample. In the range between 530 nm to 625 nm range, the 530 nm edge increases and then decreases upon

further oxidation, while the absorption around 600 nm remain basically unaffected. While other features are similar between the fresher and aged samples, the finite differences in these two regions could not be explained by the redox-induced OCP changes or shift of occupied/unoccupied frontier states: one would expect a match between the spectrum from a sample with more positive OCP but lower oxidation potential, and the spectrum from a sample with less positive OCP but at higher oxidation potentials (i.e. the 850 mV spectrum in panel A vs. the 550/850 mV spectrum in panel B). There might be gradual structural changes (over days/weeks) of this Au_{130} NCs that require further study.

3.3 Experimental

3.3.1 Chemicals

All chemicals (99% or higher) were purchased from Aldrich. Toluene was purchased from Fisher-Science, and nanopure water was produced in-house (>18 MΩ cm^{-1}).

3.3.2 Instruments

UV-Vis spectra were recorded with a Shimadzu UV-1700 spectrophotometer. Electrochemical measurements were performed on a CH Instruments (CHI 750C) with Picoamp booster in a Faraday Cage. The solution was generally purged over 15-30 mins with Ar prior to electrochemical measurements. The potential of the AgQRE (0.22 V vs. SHE) was calibrated periodically by measuring the ferrocene (Fc+/Fc) redox peak at 0.48 V.

3.3.3 Synthesis of Au_{130}(p-MBT) nanoclusters and Au(p-MBT) Complexes

The Au_{130} nanoclusters were synthesized and first characterized by Jin el al[9, 72]. The initial synthesis followed the Brust–Schiffrin method with extensive size focusing performed on the as-synthesized clusters. The size focusing process was monitored by MALDI and UV-Vis and stopped once pure Au_{130} clusters had been obtained.

The complexes were synthesized as analogs or boundary features for the Au-S interface bonding in the Au_{130} nanoclusters. Similar to the synthesis of Au clusters, the $HAuCl_4$ salt was phase transferred into the toluene solvent with TOABr first. The complexes were formed by adding *p*-MBT thiol into the Au solutions (1:1 molar ratio) under rapid stirring. No purification was performed.

3.3.4 Spectroelectrochemical Measurements

Were performed in CH_2Cl_2 or mixed solvent using a previously published setup.[32] Briefly a platinum mesh working electrode was placed in the light path inside a thin cell cuvette (1 or 2mm×10mm) for in-situ spectrum recording after each bulk electrolysis. A platinum foil as counter and a Ag/AgCl wire as reference electrodes were positioned away from the mesh working, normally slightly higher in the cuvette so as not to obstruct the light path. The solution level was checked periodically to maintain consistent concentration throughout a series of measurements.

3.4 Summary

In summary, electrochemical studies are combined with steady-state and ultrafast UV-vis-near IR absorption spectroscopy to understand the electronic transitions in Au_{130}(*p*-MBT)$_{50}$ NCs. The simple ligand molecular structure of *p*-methyl-benzene-thiolate, high symmetry of the nanocluster structure determined by X-ray and NMR, make it an appealing large nanocluster to explore the transitions of energy diagram from molecular to metallic/bulk system. Reversible QDL features with an average peak spacing of 0.21 V and a gap of 0.3 V are observed. Interestingly, near IR photoluminescence is not detected from this nanocluster with a clear energy band gap which suggests more effective non-radiative decays. Oxidation and reduction of the nanocluster by electrolysis reveal multiple transitions contributing to the four broad steady-state absorption

bands. The newly resolved spectroelectrochemical features, major changes in absorption increase/decrease upon oxidation/reduction, match the ESA and GSB bands in ultrafast measurements well. Combined together, an energy diagram is proposed through which the major steady state and newly observed spectroelectrochemical transitions are successfully explained with major electronic transitions therein. Those specific energy levels and variations at tens millivolts resolution might reveal vibrational energy state coupling to be confirmed in future studies.

This chapter is adapted with permission from J. Phys. Chem. C, 2017, 121, 21217-21224. Copyright 2017 American Chemical Society.

4 STUDYING THE OPTICAL AND ELECTROCHEMICAL PROPERTIES OF THE AU-MSA AND NEWLY SYNTHESIZED AU-LA CLUSTERS IN BOTH WATER AND ORGANIC SOLVENTS

Electrochemical studies in water are limited by the small potential window before water splitting dominates the signal when performing measurements. Due to this, insights into the electrochemical properties of many aqueous soluble gold nanoclusters have been incomplete. A simple and routine work around for this is to phase transfer the cluster into organic solvents with the use of a transfer agent such as tetraoctylammonium bromide. This allows for the use of inert solvents such as dichloromethane and acetonitrile which have much larger potential windows. This chapter discusses the optical and electrochemical features for the Au-MSA and Au-LA (1:1.7) cluster in both water and in organic solvents after phase transfer. The impacts of strong oxidizing and reducing agents on the Au-LA cluster were also studied to better understand the

gradual sulfur oxidations after cluster synthesis. Optically the phase transfer does not seem to affect the absorbance or luminescence peak shape, though a substantial increase in quantum efficiency is observed after transferring. This increase in luminescence was affected by the solvent used when performing the measurements as solvents with higher dielectric constants gave way to much lower luminescence intensity. Unsurprisingly, rich redox activities were observed for the Au-MSA cluster when using organic solvents. These would have gone unnoticed in aqueous measurements due to the restricted potential window and high dielectric constant of water.

4.1 Background and Research Strategy

Monolayer protected noble metal nanoclusters have been of great importance in the research community over the past few decades in various applications including biomedical, biosensing, biological imaging, catalysis, etc. due to their rich optical, electrochemical, and other fundamental properties. Many of these clusters fall within “magic number” or specifically a combination of gold to thiolate that can offer filled electron shells along with increased stability and distinct size depended properties. For this reason, variation of the synthetic conditions could produce new clusters with new properties. Retrospectively, specific optical absorbance features can be used to determine the core size of many of these magic number clusters. Another important tool used in the characterization of metal nanoclusters is electrochemistry. For many clusters including Au_{25}, Au_{38}, Au_{130}, Au_{144}, and Au_{246} very distinct redox activities have been observed that are size depended and can be used to accurately characterize the size of the cluster. These features include HOMO-LUMO gap spacings which are usually on the scale of 1.3-1.6 V (for the molecular-like cluster such as Au_{25}), and QDL spacings for the larger clusters. Even with this knowledge there is one glaring problem when trying to use it to compare with newly

synthesized aqueous soluble gold nanoclusters. Almost all the electrochemical work has been done in organic solvents with large potential windows and lower dielectric constants. Electrochemical techniques have been largely ineffective providing limited insights when researching aqueous soluble nanoclusters due to the narrow potential window and high dielectric constant.

To get around this, the process of phase transfer can be performed on many of the aqueous soluble gold nanoclusters. There have been various works published on this process and it has been shown to be nondestructive and reversible. [64-65, 146] For the clusters previously looked at it was noted that the optical properties including the main peaks were largely unchanged and even when reversing the phase transfer no major difference between pre-transfer and reversed-transfer were observed. One major observation for the $Au_{22}SG_{18}$ cluster was that the phase transfer caused a substantial increase in Q.E. It was discovered that this enhanced Q.E. is due to the tetraoctylammonium bromide causing an increased rigidity in the gold shell. This rigidity was caused by the bulkiness of the TOA^+ which was proven by exchanging the TOA^+ with shorter chain quaternary ammonium cations. Once this exchange took place a significant drop in Q.E. was observed for cations such as tetramethylammonium. Optically, the ability to observe the clusters in organic solvents is nice but the larger potential window allowed by the solvents is where advantages can be taken.

In the previous report on Au_{22}-LA_{12} (chapter 2), the electrochemical activity of the cluster was looked at in both aqueous and organic mediums[146]. With the Au_{22}-LA_{12} cluster a HOMO-LUMO gap of 1.53 V was observed in aqueous measurements however some of the electrochemical processes could not be fully resolved. Once phase transferred, the potential is no longer limited by water, and the electrochemical features can be resolved or better defined at

more negative/positive potentials. A well-defined oxidation pair resembling what is seen with other molecular like nanoclusters could be observed. It was also noted that the HOMO-LUMO gap after transfer was 1.34 V. This is smaller than what was observed in water though this could be due to the phase transfer itself or due to the solvent.

In this chapter the previously published Au-MSA and newly synthesized Au-LA clusters are studied optically and electrochemically in both water and organic solvents after phase transfer. Optical features (absorbance and luminescence) have been reported for the Au-MSA cluster in aqueous mediums, and absorbance changes or lack thereof when phase transferred were previously reported along with the $Au_{22}LA_{12}$ cluster. Luminescence effects are studied and reported for the first time after being phase transferred along electrochemical properties including both in water and organic solvents.

4.2 Results and Discussion

4.2.1 Optical Features

The Au-MSA clusters reported were synthesized following previously published literature[13]. Briefly, $HAuCl_4$ was dissolved in a 6:1 mixture of methanol and acetic acid. This was then mixed with 15x equivalence of MSA under mild stirring. Once colorless the mixture was chilled with ice and then reduced once the temperature had equilibrated with a 20x solution of $NaBH_4$ (in similarly chilled water) under vigorous stirring. After completion the sample was rotavaped to dryness, redissolved in water, and purified using dialysis. Afterwards the solution was etched using a 10x solution of MSA at 50^{o}C for 24 hours. Aqueous optical measurements shown in Figure 4.1 match what was previously reported for this cluster[13]. The absorbance is relatively featureless through the full observable range. Broad near-IR luminescence is observed for this cluster with a peak intensity at 826 nm and a quantum efficiency of around 4. This Q.E. is

a bit weaker than previously published aqueous soluble clusters such as the $Au_{22}LA_{12}$ cluster though is still bright enough to be used in applications such as cellular imaging.[25,13]

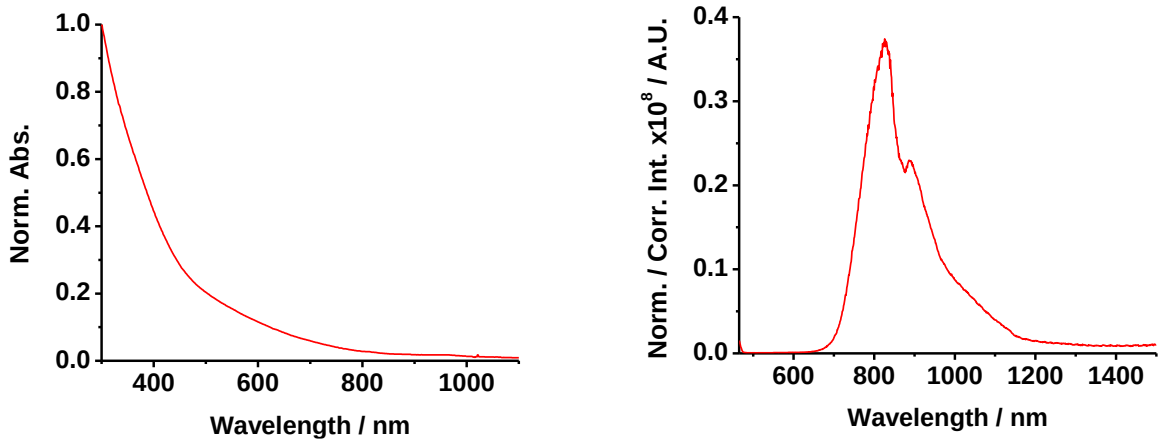

Figure 4.1. Optical Features of the Au-MSA cluster in H_2O. Normalization by the absorbance at the excitation wavelength of 400 nm was performed on the luminescence spectrum.

The Au-LA nanoclusters were synthesized following a previously reported procedure with some minor changes[25]. Briefly, $HAuCl_4$ was dissolved in 1 mL of nanopure water. A 1.7x amount of lipoic acid, w.r.t. Au and referred as 1.7X pending full characterization, was then added to 1 mL of nanopure water and NaOH was added dropwise until the lipoic acid fully dissolved. This was then added under mild stirring to the solution of $HAuCl_4$. After 4 hours of stirring a 5x solution of $NaBH_4$ was quickly added under vigorous stirring. This was allowed to react until the luminescence intensity peaked (usually around 16 hours). Afterwards, the solution was purified either by centrifuging the sample with a 3500 MWCO filter, or by using snakeskin dialysis tubing (3500 MWCO) to perform dialysis of a period of three days. Interestingly the two purification methods would lead to two types of samples. One sample (centrifuged) has nicely defined absorbance features, but in turn has very weak luminescence. The other sample (dialysis) loses the definition in the absorbance features though has a much higher luminescence intensity. These observations mirror what was seen with the $Au_{22}LA_{12}$ cluster so it reasonable to conclude

that these changes can be attributed to the oxidation of the lipoic acid attached to the clusters. These changes can be slowly observed in the centrifuged sample if left to oxidize over a few days to a week. The absorbance features will start to become less apparent and eventually disappear. The luminescence will also rise over this time though never quite reach the intensity observed for the dialysis sample. This can most likely be attributed to a small amount of annealing that the cluster is going through during dialysis. Since the dialysis does not immediately remove all of the excess thiols it is possible there are some rearrangements in the monolayer that help facilitate this large increase in luminescence. For the centrifuged sample, three distinct absorbance peaks can be observed at 505, 600, and 700 nm. A low Q.E. of around 1% was calculated for the sample. For the dialysis sample however a Q.E. of 10% was calculated. This Q.E. is similar to what was calculated for the $Au_{22}LA_{12}$ clusters. The absorbance spectrum however is relatively featureless throughout the full range. Figure 4.2 shows the absorbance and luminescence features for both the centrifuged and dialysis samples.

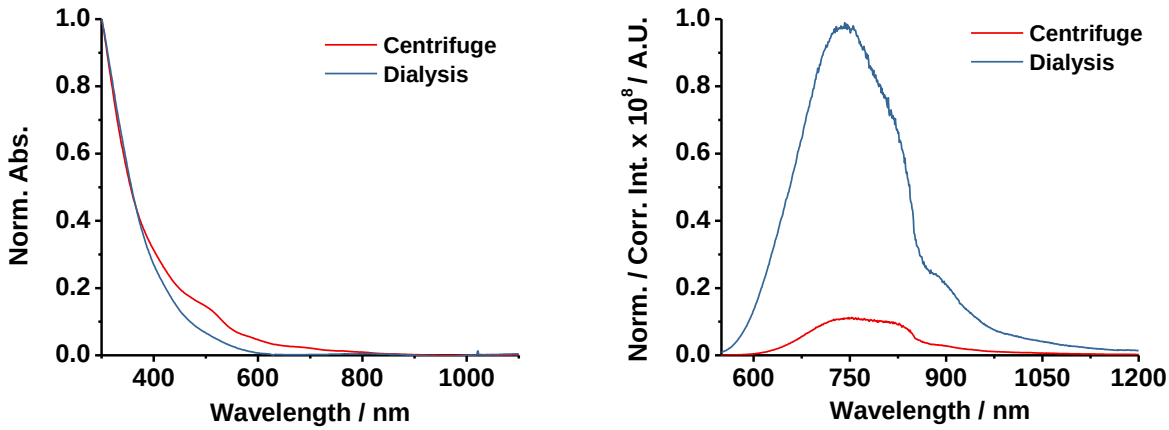

Figure 4.2. Optical features of the Au-LA Cluster in H2O. The absorbance was normalized to one at 300 nm. Luminescence spectra normalizations by the absorbance at the excitation wavelength of 400 nm were performed. Centrifuged sample measurements were taken from a freshly purified sample to avoid extensive oxidation.

In an attempt to decrease the time it takes for a centrifuged sample to oxidize and have the luminescence increase, experiments with H_2O_2 were carried out. Due to the H_2O_2 being a modest oxidative molecule small amounts of it were titrated into a unoxidized Au-LA sample to test the effects on both the gradual changes in absorbance and luminescence spectra under ambient conditions. Changes are insignificant until 1 mmol of the H_2O_2 had been titrated in. Kinetic effects were also observed. Initially, even at the 1 mmol point the absorbance spectrum does not change at all, but after 10 minutes this was rechecked and a major change in the absorbance was observed. The absorbance spectrum had a much sharper slope and overall the distinct absorbance features were less obvious. The luminescence spectrum did initially show an increase at the 1 mmol point, and after 10 minutes had increased even higher. Figure 4.3 shows the optical features at each addition of H_2O_2. Further experiments were performed with slightly higher amounts of H_2O_2 and a longer duration of time to see how this effect the features. Overall there was not huge differences when more H_2O_2 was added though if the solution was not purified the luminescence decreased nearly 100% and a gold plasmonic band was observed in the absorbance spectrum. This is not surprising due to the oxidative nature of H_2O_2.

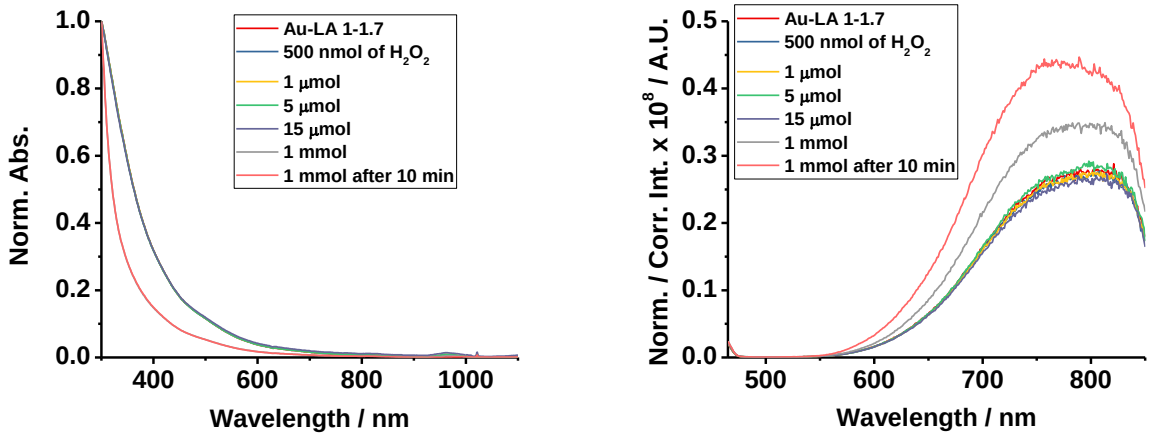

Figure 4.3. Absorbance and luminescence spectra during H_2O_2 titration. Absorbance measurements were normalized to one at 300 nm. Luminescence spectra were normalized by the absorbance at the excitation wavelength of 400 nm.

With the success of oxidizing the centrifuge sample, the reverse experiment was performed with the oxidized centrifuge sample. This time however a strong reducing agent ($NaBH_4$) was titrated in instead of H_2O_2 to determine if the distinct absorbance features observed in the unoxidized sample could be brought back by further reducing the sample. The goal is to understand whether the optical changes result from core redox states which would be reversible or the ligand/interfacial bonding which would be irreversible. The absorbance spectra showed an overall increase throughout the full range. The prominent peaks seen in the unoxidized sample did not reappear. This addition of $NaBH_4$ also had negative effects on the luminescence intensity of the sample. With each addition the luminescence decreased substantially to a point where it had fell to around 25% of the initial intensity. Further additions of $NaBH_4$ would have most likely dropped the luminescence even further. The absorbance and luminescence spectra for this titration can be found in Figure 4.4

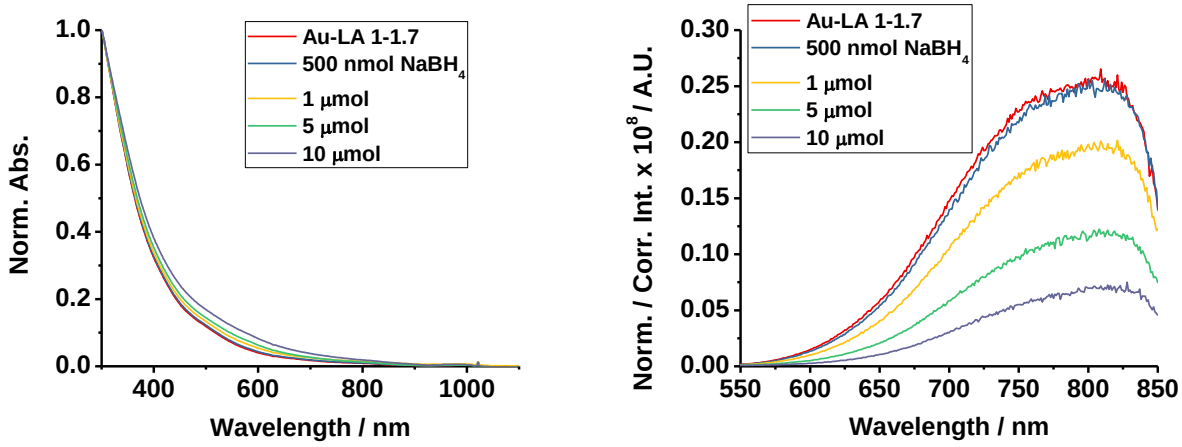

Figure 4.4. Absorbance and luminescence spectra after adding $NaBH_4$. Absorbance measurements were normalized to one at 300 nm. Luminescence spectra were normalized by the absorbance at the excitation wavelength of 400 nm.

The process of phase transferring the Au-MSA or Au-LA clusters is a relatively simple process and was previously reported[146]. Normally Au-MSA/LA clusters aqueous solution is placed in a vial along with toluene. TOABr is then added to phase transfer the cluster. A mild shaking is enough to transfer the cluster. After transferring the cluster can be dissolved in various organic solvents such as acetonitrile, toluene, and dichloromethane. One thing to note is the transfer will be much more difficult and at times impossible if there is a higher concentration/amount of salt in the aqueous sample. To mitigate this issue the sample is purified before any phase transfer. Figure 4.5 shows the absorbance and luminescence features of the phase transferred Au-MSA and Au-LA clusters.

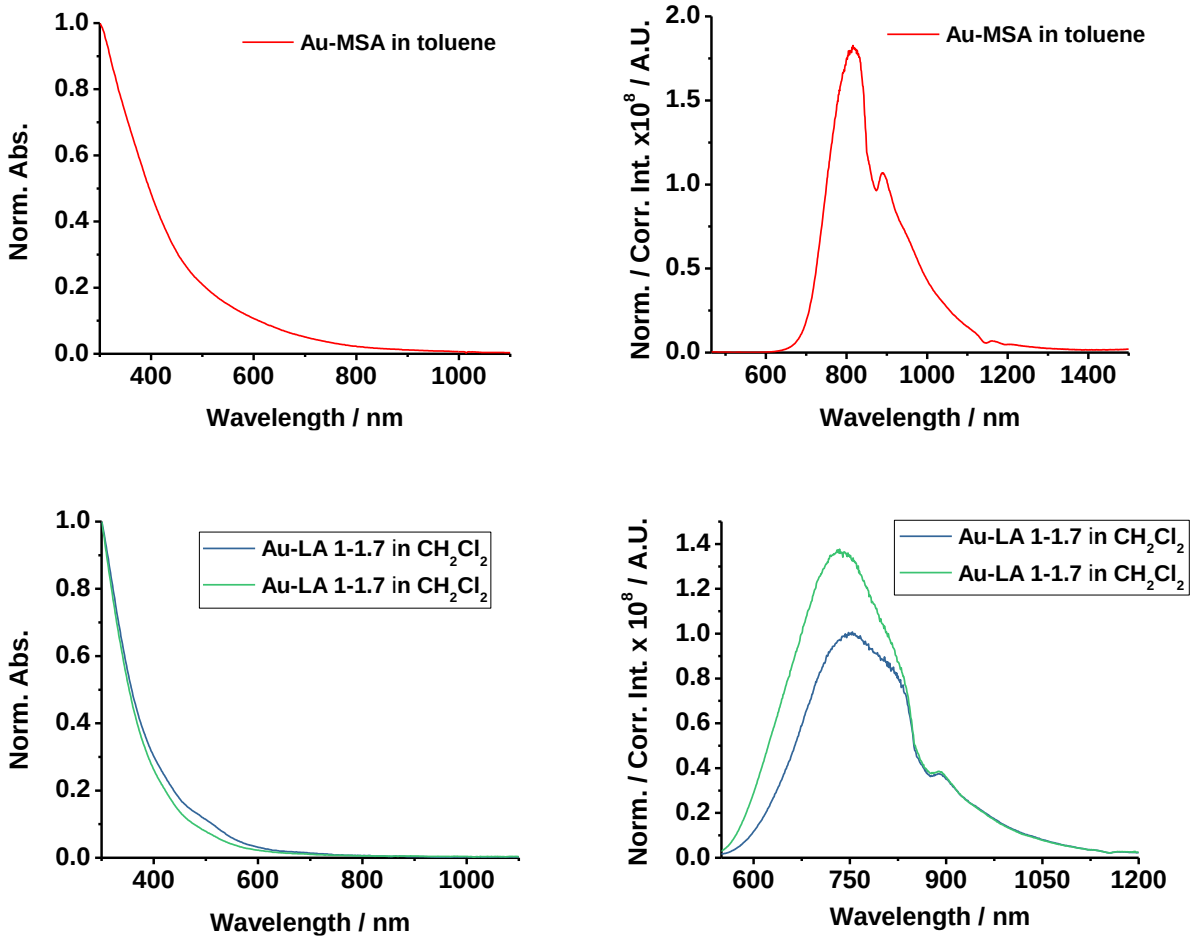

Figure 4.5. UV visible absorbance and photoluminescence spectra of the Au-MSA (top) in toluene and the Au-LA (bottom) cluster in dichloromethane. Absorbance measurements were normalized to one at 300 nm. Luminescence spectra were normalized by the absorbance at the excitation wavelength of 400 nm.

Optically, the transfer does not affect the absorbance curvature of either the Au-MSA sample or the Au-LA cluster. Like reported earlier the Au-MSA cluster still has a featureless decay over the full range with no new absorbance features being observed[146]. For the Au-LA cluster the centrifuge sample still shows the same three absorbance features 505, 600, and 700 nm, and again the dialysis sample shows just a featureless decay. Figure 4.6 shows the comparison for both the Au-MSA and Au-LA samples. Overall the steady-state absorbance

features are basically unaffected by phase transfer for all aqueous clusters tested up to date. This includes the previously reported phase transferred clusters including the $Au_{22}LA_{12}$, $Au_{22}SG_{18}$, and Au_{25} clusters[64-65, 146]. Because solvent and/or ion permeation into ligand monolayer is anticipated to affect some electrochemical properties, the basic phase transfer results will serve as baseline controls for spectroelectrochemistry and time-resolved transient analysis.

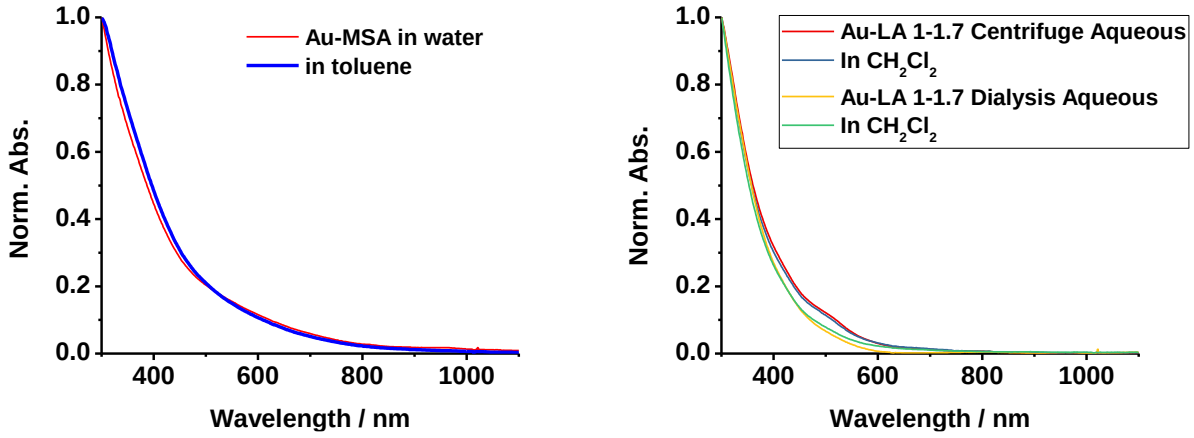

Figure 4.6. UV-Vis comparison of aqueous and phase transferred Au-MSA (Left) and Au-LA (Right). Absorbance measurements were normalized to one at 300 nm. Luminescence spectra were normalized by the absorbance at the excitation wavelength of 400 nm.

Similar to the absorbance spectra, the overall luminescence spectrum shape is unaffected by the transfer into organic solvents. The most noticeable change however is the significant increase in the quantum efficiency from 4 to 18% for the Au-MSA cluster, 1% to 10% (centrifuge) and 10% to 14% (dialysis) for the Au-LA cluster. The luminescence spectra comparing the intensity in both water and in organic solvents for the clusters are shown in Figure 4.7. The increase in luminescence for the three samples is very similar to what was observed when the previously published $Au_{22}SG_{18}$ nanocluster was phase transferred into organic solvents.[64] It was noted that this cluster showed an increase to more than 60% after being phase transferred with TOA^+. Though the MSA and lipoic acid ligands are not as bulky compared to

the glutathione attached to the Au_{22} cluster it is possible a similar rigidifying of the monolayer is occurring causing this increase in luminescence.

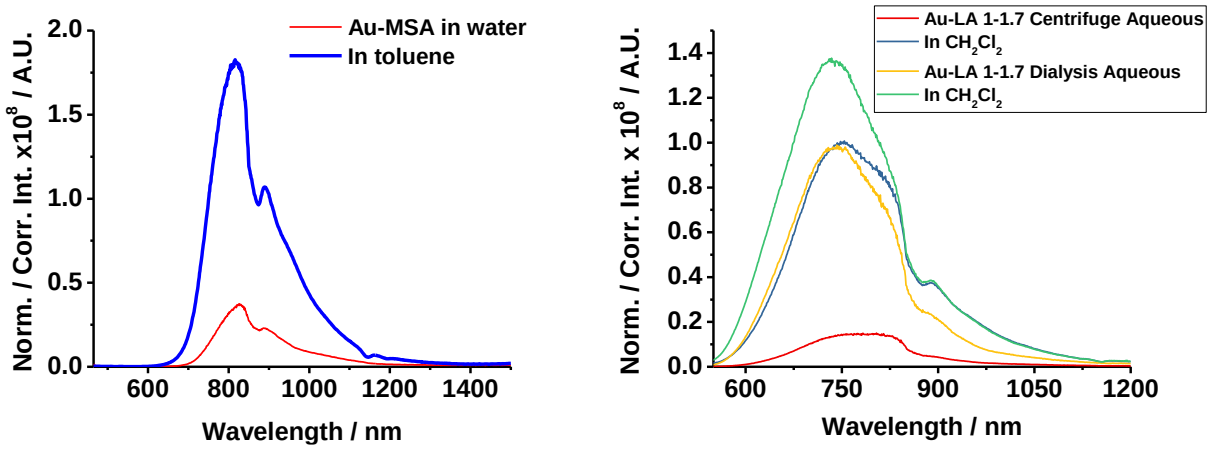

Figure 4.7. Luminescence comparison of the aqueous and phase transferred Au-MSA (Left) and Au-LA (Right). Absorbance measurements were normalized to one at 300 nm. Luminescence spectra were normalized by the absorbance at the excitation wavelength of 400 nm.

With the previously published $Au_{22}SG_{18}$ cluster, the types of organic solvents were also explored as a variable to explain this increase in luminescence. It was concluded that the increase in luminescence did in fact have some dependence on the solvent[64]. This was attributed to the differences in the dielectric constants for the various solvents. As the dielectric constant increased in the solvent the luminescence intensity decreased that is well-known in classic organic dyes. To determine the solvent effects on both the Au-MSA cluster and the oxidized Au-LA cluster, a few different solvents were checked. It was observed that regardless of the solvent the absorbance curve for the Au-MSA clusters did not change at all. Luminescence wise there were some small changes in luminescence intensity between toluene, acetonitrile, and dichloromethane, but with methanol there was a significant drop in the luminescence intensity. This is similar to what was seen with the $Au_{22}SG_{18}$ sample however one main difference is the fact the luminescence intensity did not drop much in acetonitrile. This is interesting since

acetonitrile has a higher dielectric constant than methanol, yet the luminescence only dropped slightly. Compared to glutathione, two factors might have contributed to the differences between methanol and acetonitrile: less rigid/structurally hindered ligand structures and likely stronger hydrogen bonding. Both would facilitate more significant participation of methanol into the ligand monolayer and lower the emission. Figure 4.8 shows the absorbance and luminescence spectra in the various organic solvents verses water.

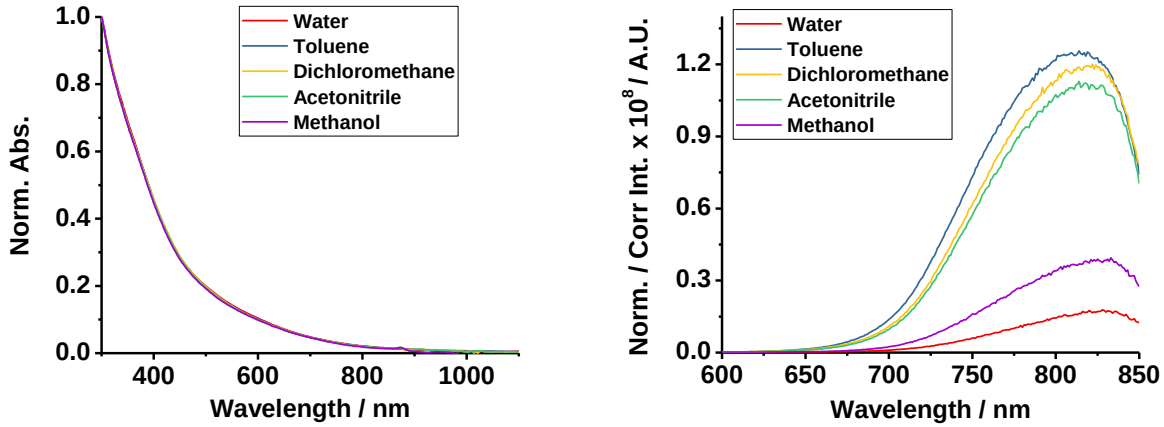

Figure 4.8. UV-Vis and luminescence spectra of the Au-MSA cluster in various organic solvents. Absorbance measurements were normalized to one at 300 nm. Luminescence spectra were normalized by the absorbance at the excitation wavelength of 400 nm.

Similar observations were made for the oxidized Au-LA cluster. Again, the absorbance curves show little to no change regardless of the solvent used for the measurement. Luminescence spectra also show a similar trend where the toluene, dichloromethane, and acetonitrile only show small differences between the luminescence intensity in each solvent. It was not until the measurement was performed in methanol did a noticeable change in luminescence intensity occur. Like with the Au-MSA cluster a drastic decrease in luminescence intensity (around 50%) is observed. Figure 4.9 shows the absorbance and luminescence spectra for the Au-LA oxidized sample. These measurements were not performed on the unoxidized

form of this clusters. It is already noted that transferring the unoxidized cluster and measuring its absorbance in CH_2Cl_2 caused little to no change, so it is unlikely that any of the other solvents would have any major effect on the absorbance. The luminescence also showed the same increase in luminescence with the initial CH_2Cl_2 measurement like the other two clusters. Any further changes in intensity should follow similar trends with what is observed for the Au-MSA and Au-LA (dialysis) sample.

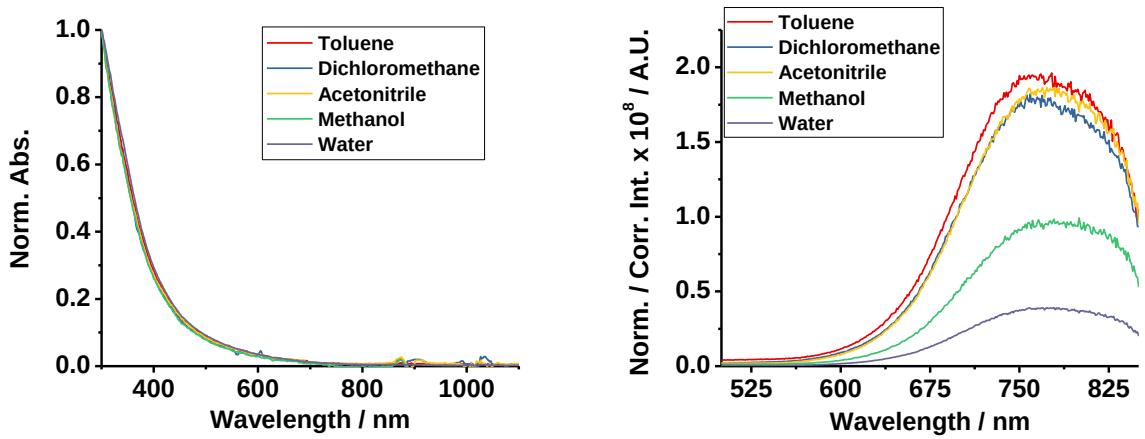

Figure 4.9. UV-Vis and luminescence spectra of the oxidized Au-LA cluster in various solvents. Absorbance measurements were normalized to one at 300 nm. Luminescence spectra were normalized by the absorbance at the excitation wavelength of 400 nm.

Further experimentation with different phase transfer agents should also be looked at with these two cluster systems. In the case of the $Au_{22}SG_{18}$ cluster it was noted that varying the carbon chain length on the transfer agent had significant effects on the increase in luminescence intensity. Longer chain lengths gave way to higher increases while shorter chain lengths gave little to no increase in luminescence intensity or for much shorter chains did not even allow for the transfer of the cluster from water to toluene. In order to obtain optical measurements using these chain lengths cation exchange reactions had to be used to replace the TOA^+ with a cation such as TMA^+. Similar issues involving tetrabutylammonium borate or tetrahexylammonium

tetrafluoroborate were observed while trying to use other quaternary ammonium salts to transfer the Au-MSA or Au-LA clusters.

4.2.2 Electrochemical Features

Electrochemical measurements are what really make the ability to phase transfer the aqueous soluble Au-MSA and Au-LA nanoclusters exciting. To get a baseline of what may be observed in the smaller potential window, cyclic voltammetry (CV) and square wave voltammetry (SWV) measurements were first performed on the samples in water. Figure 4.10 shows the CV and SWV for the Au-MSA cluster. Within the smaller potential window without significant water redox current, a few redox activities are observed. The main features include a reversible reduction feature around -0.8 V. Another pair of redox features at -0.33 V which is very close to where oxygen reduction would be seen so it is possible that the purging was not 100% successful. Other redox activity includes small oxidation features at 0.6 and 1.1 V along with reduction features at 0.22 and 0.68 V. To get around this small potential window the cluster was phase transferred and dissolved in acetonitrile so a much larger window could be used.

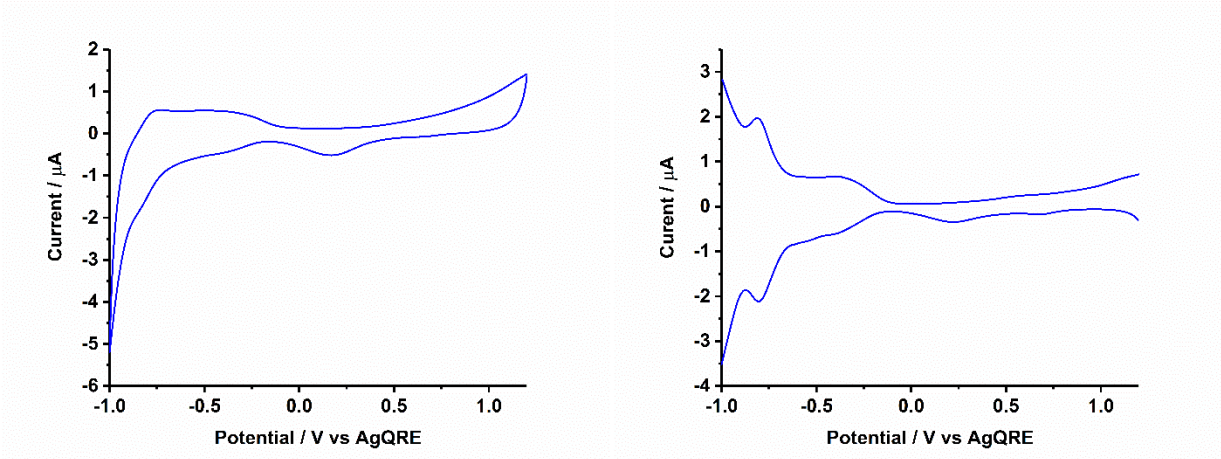

Figure 4.10. CV and SWV of the Au-MSA cluster in H_2O. Purging with Ar for 15-30 mins with 0.1 M $NaClO_4$ as the supporting electrolyte. A 0.2 mm platinum disk working electrode, platinum foil counter, and an Ag/AgCl wire were used for all measurements.

Like the previously published results on the $Au_{22}LA_{12}$ cluster, the redox activities of Au-MSA cluster are better resolved after phase transferring. Oxidation features can be observed in CV at more positive potentials, with peak values resolved by SWV at 0.90, 1.12 in oxidation scan and 1.40 V 0.90, and 1.14 V in reduction scan. The reduction features in CV have respective peaks at -1.26, -0.60 in reduction scan and -1.32, -0.62 in oxidation scan. In particular, the redox activities around 1 V are much more prevalent and this is most likely due to the fact water is no longer an issue. Assuming the peaks at 0.9 and 1.12 represent the spacing due to charging energy, the 0.22 eV is similar to what is seen with other molecular-like gold nanoclusters. The HOMO-LUMO gap however is quite a bit larger if calculated using the -1.26 reduction peak and the 0.90 V oxidation peak. This would give way to a gap of 2.16 V which is significantly larger than what has been previously seen with other molecular-like gold nanoclusters. This would suggest that the cluster is smaller than the likes of Au_{22} or Au_{25}. Figure 4.11 shows the CV and SWV of the phase transferred Au-MSA clusters.

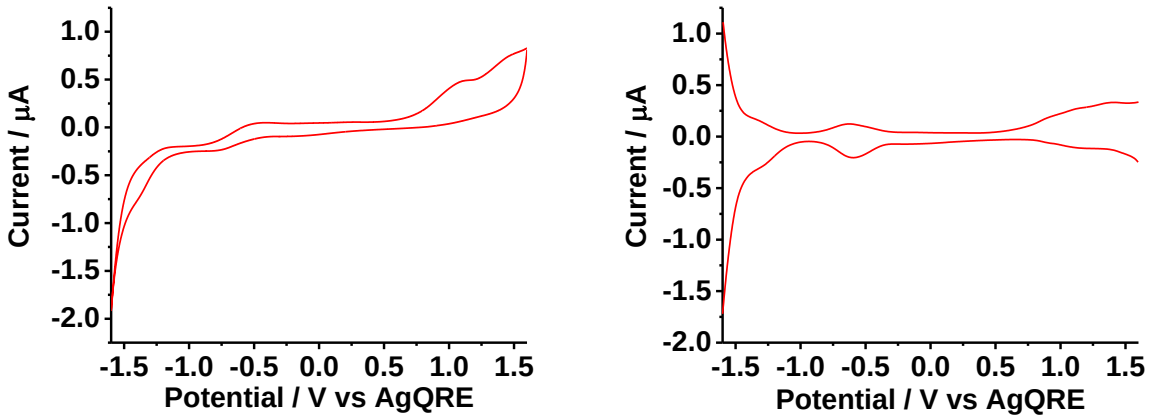

Figure 4.11. CV and SWV for the phase transferred Au-MSA clusters. Purging with Ar for 15-30 mins with 0.1 M TBAP as the supporting electrolyte. A 0.2 mm platinum disk working electrode, platinum foil counter, and an Ag/AgCl wire were used for all measurements.

A concern was that the bromine anion in the phase transfer agent TOABr was electrochemically active. A very apparent redox couple can be observed with peaks on the oxidation curve at 0.99 and 1.3 V along with peaks on the reduction curve at the same potentials. To suppress this issue a more precise phase transfer was performed whenever electrochemical measurements were going to be performed. To avoid introducing extra bromine, sub-stoichiometry amount was used so that not all of the cluster was transferred from the aqueous to organic phase. A small amount of cluster was left behind in the aqueous phase with the rationale that all the TOA^+ would be attached to the cluster and any Br^- would be in the aqueous phase. This seemed to be quite effective though a much better solution would to be to obtain a transfer agent that is not electrochemically active. Figure 4.12 shows the CV and SWV for TOABr in acetonitrile for reference.

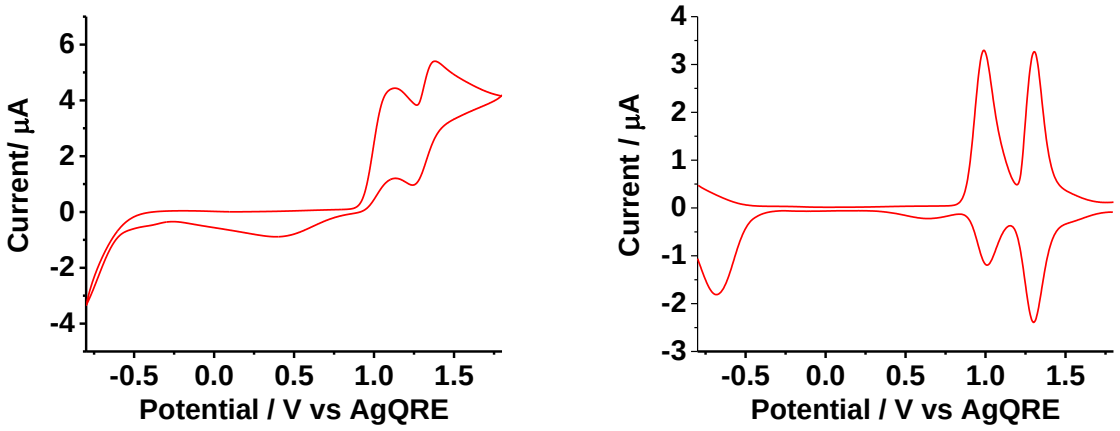

Figure 4.12. CV and SWV of the TOABr in ACN. Purging with Ar for 15-30 mins with 0.1 M TBAP as the supporting electrolyte. A 0.2 mm platinum disk working electrode, platinum foil counter, and an Ag/AgCl wire were used for all measurements.

Electrochemical measurements were performed on both the unoxidized and oxidized samples in aqueous solution. For the previous $Au_{22}LA_{12}$ sample the ligand oxidation could be see around 1.0 V so it could be expected to see something similar with this cluster due to using the

same ligand. The potential window is severely limited in water, but a few redox activities could be observed for both samples. For the unoxidized sample, a well-defined feature can be found at -0.70 V in the oxidation scan SWV, with a small shoulder at 0.84 V and what looks to be another feature at around 1.1 V though it is hard to distinguish due to significant background current from water. Assuming these two positive potential peaks are the HOMO and spacing of 260 mV can be calculated. The 0.26 eV charging energy is similar to the other molecular-like gold nanoclusters tested. In the reduction scan SWV, a defined peak at -0.75 V is observed related to the peak at -0.70 V seen in oxidation scan. This reversible electron transfer (about 60 mV splitting between ox/red) is apparent in CV despite the significant background current. The broad feature at 0.36 V that looks to have a small shoulder at 0.21 V in both CV and SWV. Using the peak at -0.75 V as LUMO, a HOMO-LUMO spacing of 1.59 V is calculated which again is in line with other clusters like the various $Au_{25}SR_{18}$. Figure 4.13 shows the cyclic voltammogram and square wave voltammogram for the unoxidized sample.

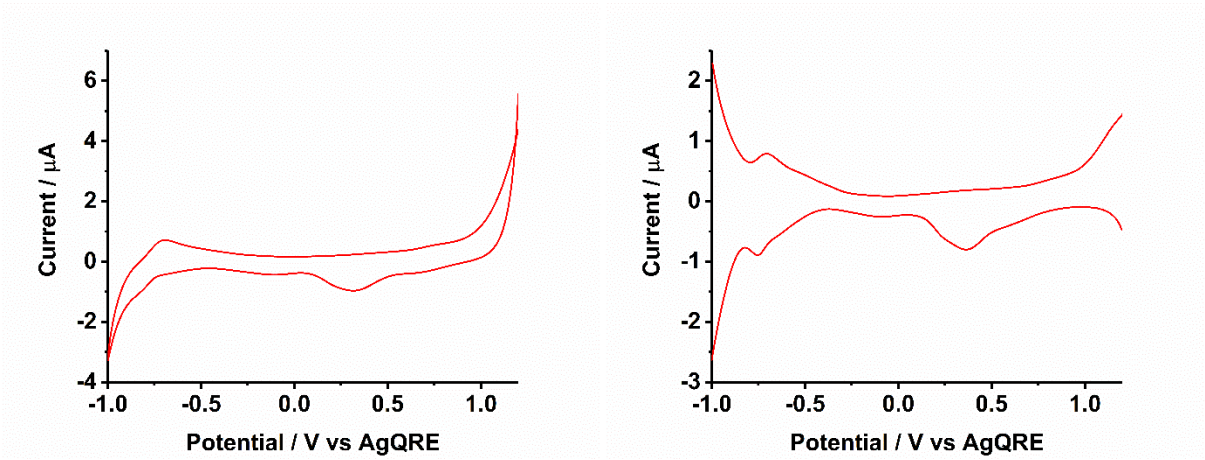

Figure 4.13. CV and SWV of the Au-LA Cluster in H_2O. Purging with Ar for 15-30 mins with 0.1 M $NaClO_4$ as the supporting electrolyte. A 0.2 mm platinum disk working electrode, platinum foil counter, and an Ag/AgCl wire were used for all measurements.

The oxidized sample shows similar features though some are slightly shifted. The defined reduction peak that was located at -0.7 V is now seen at -0.66 V in oxidation scan SWV. The small shoulder at 0.84 V is still located at the same potential though it is now much more defined. It is still possible there is an oxidation feature at around 1.1 V but again it is buried by high background current. Reduction wise the feature at -0.75 V is now located at -0.70 V. The small broad feature at -0.10 V shifted to 0.03 V and the larger broad feature that was at 0.36 V is now at 0.47 V and no longer shows the second shoulder. Overall the charging energy and HOMO (+0.84V) - LUMO (-0.70V) spacing that can be calculated are very similar compared to that of the unoxidized sample. The CV and SWV for the oxidized sample can be seen in Figure 4.14.

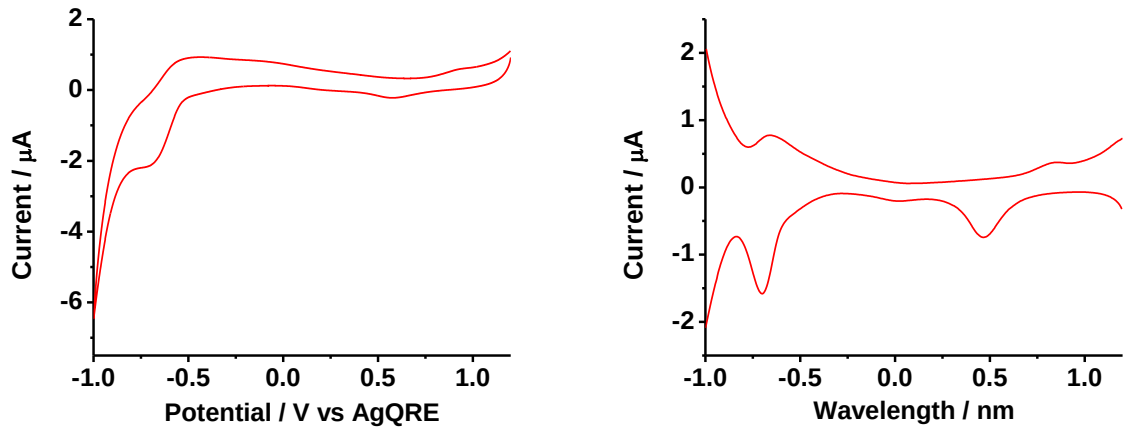

Figure 4.14. CV and SWV of the oxidized Au-LA Cluster in H_2O. Purging with Ar for 15-30 mins with 0.1 M $NaClO_4$ as the supporting electrolyte. A 0.2 mm platinum disk working electrode, platinum foil counter, and an Ag/AgCl wire were used for all measurements.

4.3 Mass Spectrometry

Previous attempts at using mass spectrometry to determine a composition of clusters in aqueous solution were not completely successful. Mostly single-charge smaller fragments were observed in the spectrum that were inconclusive to propose a possible molecular composition.

With the phase transfer capability, mass spectrometry analysis has been revisited in additional solvent systems. Figure 4.15 shows the reoccurring features that were observed when performing ESI measurements in a 50:50 water:acetonitrile mixture. Like previous attempts the main features observed are smaller fragments with the largest fragment being that of $Au_4MSA_4^-$ (1384 m/z). Apparent sodium adducts are also observed throughout the spectrum as 22 m/z spacings. This was a persistent problem to deal with regardless of purification methods used. As seen in Figure 4.15 a consistent spacing of 116 m/z is noted. This fragment m/z matches the MSA ligand without the sulfur atom, so it can be assumed we are losing the bulk of the MSA ligand and leaving a sulfur atom attached to the Au_4 fragment. This can be followed until on a Au_4S_4 fragment is left. Other fragment patterns like this can be observed throughout the lower range of the spectrum (not shown).

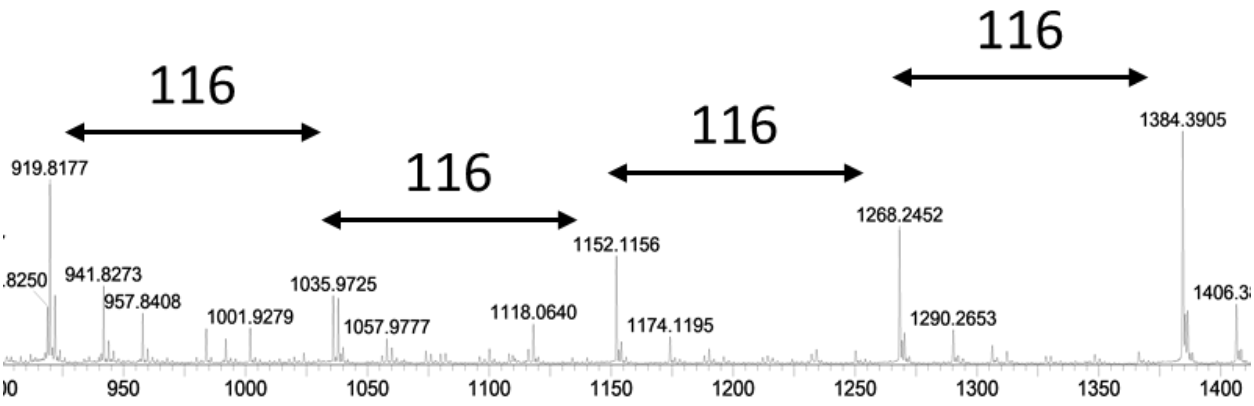

Figure 4.15. Negative mode ESI of the Au-MSA cluster in 50:50 water:acetonitrile. Concentration of the cluster was 1.5 mg/mL.

Since similar results were seen in these new attempts, the phase transferred Au-MSA clusters were analyzed to capture either molecular ion or multicharged species that could then be used to determine a molecular structure. These measurements were performed in a 50:50 mixture of dichloromethane and acetonitrile. No further electrolytes were added into the system. Figure

4.16 shows the main observed features from these attempts. Similar to the aqueous experiments small fragmentation was observed throughout the spectrum again with the largest fragment being that of $Au_4MSA_4^-$. However, a few larger fragments with a spacing of 467 m/z are observed past the $Au_4MSA_4^-$ fragment. These were calculated to be the $Au_4MSA_4TOA_1^-$, $Au_4MSA_4TOA_2^-$, $Au_4MSA_4TOA_3^-$, and $Au_4MSA_4TOA_4^-$ fragments at 1849.51, 2315.28, 2781.87, and 3548.53 respectively. Unfortunately, this is again not enough to determine a molecular composition for the cluster. Further mass spectrometry experiments including MADLI should be carried out to help determine the composition of the cluster.

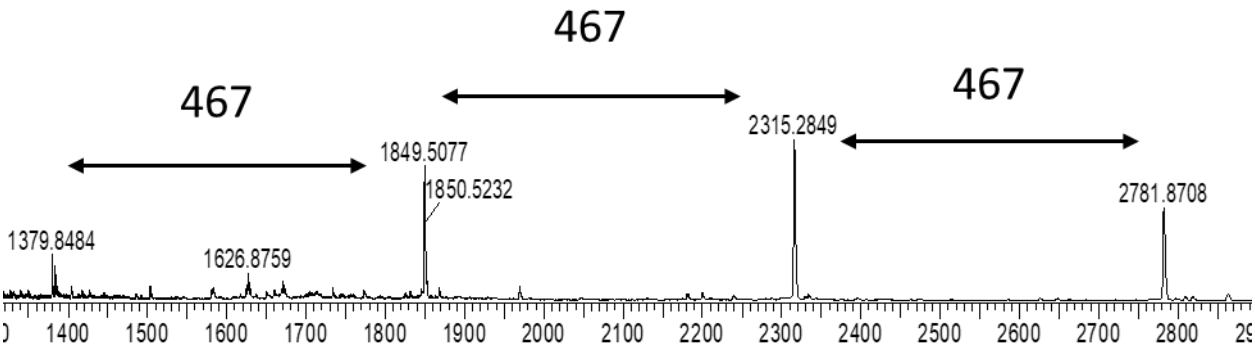

Figure 4.16. ESI of the Au-MSA cluster in 50:50 dichloromethane:acetonitrile. Sample concentration was 1.5 mg/mL.

4.4 Experimental

4.4.1 Chemicals

All chemicals (99% or higher) were purchased from Aldrich. Toluene was purchased from Fisher-Science, and nanopure water was produced in-house (>18 Mcm-1).

4.4.2 Instruments

UV-Vis spectra were recorded with a Shimadzu UV-1700 spectrophotometer. NMR spectra were collected with a Bruker NMR 400 MHz spectrometer. Electrochemical

measurements were performed on a CH Instruments (CHI 750C) with Picoamp booster in Faraday Cage. The solution was generally purged over 15-30 mins with Ar prior to electrochemical measurements. The potential of the AgQRE (0.22 V vs. SHE) was calibrated periodically by measuring the ferrocene (Fc+/Fc) redox peak at 0.48 V.

4.4.3 Au-MSA Synthesis

Synthesis followed a previously published report on the Au-MSA nanoclusters.[13] $HAuCl_4$ was first dissolved in 10 mL of a 1:6 mixture of acetic acid and methanol and mixed with a 20x MSA solution dissolved in another 10 mL of the same acetic acid and methanol mixture. The MSA was then added to the $HauCl_4$ solution and was stirred until turning colorless. The solution was then placed into an ice bath until the temperature equilibrated. Next a freshly prepared ice cold solution of 20x $NaBH_4$ in 10 mL of nanopure water was quickly added under rapid stirring causing the solution to quickly turn dark. After 3 hours the solution was rotavaped and redissvoled into 10 mL of water. The pH of the solution was then lowered to 1 with the use of concentrated HCl in order to fully protonate the smaple. Afterwards it was purified by dialysis for 3 days using snakeskin dialysis tubing (3500 MWCO, Thermo Scientific). Once purified the sample was annealed with 10x MSA for 24 hours at 50^{o}C under mild stirring. The final product was then purified using the previous method.

4.4.4 Au-LA Synthesis

Synthesis followed a previously report on Au-LA nanolcusters with some slight changes[25]. Lipoic acid was first dissolved in water at a slightly basic pH due to solubility issues. The lipoic acids solution was then mixed with $HAuCl_4$ for a final mole ratio of 1.7:1 lipoic acid to gold. This was then stirred for 4 hours. A 1x solution of $NaBH_4$ was then quickly added at room temperature and the reaction was allowed to react until the luminescence peaked. The

crude clusters were then purified by centrifuging with a 3500 MWCO filter or by performing dialysis for 3 days using the snakeskin dialysis tubing (3500 MWCO).

4.4.5 Phase Transfer

During a typical transfer of the clusters, the Au-MSA is dissolved in 1-2 mL of water. Next, 2 mL of toluene is then added on to and an approximate stoichiometry amount of TOABr is used so there would be no significant excess TOA^+ in solution when performing future electrochemical experiments or ^1H NMR. A mild shaking was sufficient to fully transfer the Au-MSA clusters. Afterwards the mixture is allowed to settle in order to re-establish the phase boundary so that it is easier to separate out the transferred clusters from the aqueous phase.

4.5 Summary

In conclusion, the optical and the electrochemical properties of Au-MSA and Au-LSA (1-1.7 ratio) clusters were studied in both the aqueous and organic solvents via phase transfer. The long carbon chains of the phase transfer agent tetraoctylammonium bromide allowed for the quick and easy transferring of the clusters into toluene. Once phase transferred the clusters could be dried and redissolved in many different organic solvents. This transfer can also be easily reveresed by adding a salt such as sodium perchlorate or potassium chloride in water and shaking with the already transferred sample in organic solvent. The process of phase transferring the cluster had little effect on the absorbance spectrum, but a significant increase in quantum efficiency from 4 to 18% for the Au-MSA and 1% to 10% (centrifuge) and 10% to 14% (dialysis) for the Au-LA. Two factors contributed to the increase: the TOA^+ helps to rigidify the gold core causing a tighter monolayer, and suppression of hydrogen bonding/solvent (with high dielectric constant) penetration into monolayer. Electrochemical data was obtained firstly in water to see what redox activites could be observed in the smaller potential window allowed by

water. For both samples there were a few redox activies observed. For the phase transferred Au-MSA sample the concern of the bromide ion being redox active is mitigated by adopting sub-stoichiometry tranfer, i.e. with less TOABr used and extra clusters un-transferred in aqueous solution. In the case of the Au-MSA aqueous electrochemical results the oxidation SWV scan showed peaks at -0.8, 0.6, and 1.1 V. Reduction SWV peaks at -0.8, -0.33, 0.22, and 0.68 were also observed. The reduction peak at -0.33 is possibly due to oxygen which would mean the purging is not 100% effective. Once phase transferred the cluster had quite a few more redox activites including peaks at -1.32 , -0.62, 0.90, 1.12, and 1.40 V in the oxidation SWV scan along with features at -1.26, -0.6, 0.9, and 1.14 V in the reduction SWV scan. For the Au-LA cluster the redox activities of the unoxidized and oxidized samples were studied. For the unoxidized sample the oxidation SWV scan had observable peaks at -0.7, 0.84, and 1.1 V with peaks at -0.75, -0.1, 0.21, and 0.36 in the reduction scan. Some slight shifts in these potentials are observed in the oxidized sample with the peaks showing up at -0.66, 0.84, and 1.1 V in the oxidation SWV scan and the reduction scan showing peak at -0.7, 0.03, and 0.47 V.

5 SYNTHESIS AND CHARACTERIZATION OF A NEWLY FORMED AG-LA NANOCLUSTER

Like their gold counterparts monolayer-protected silver nanoclusters have proven to be an important nanoscale research topic. Due to increased research in the field many new and exciting molecular-like and plasmonic clusters have been synthesized. In this chapter a newly synthesized Ag cluster is characterized optically and electrochemically. Distinct absorbance bands are present at 326, 426, and 500 with a shoulder at 640 nm. Near-IR photoluminescence is observed with a peak intensity at 675 nm. This emission is highly pH dependent and heavily

affected by oxidation. If purified by dialysis or left in open atmosphere, oxidation on the lipoic acid ligand occurs and results in the loss of observable absorbance peaks. This effect can be reduced by quickly purging the sample with argon after synthesis. This oxidation was characterized by the observation of S=O symmetric and asymmetric stretching bands in FT-IR measurements. Like its gold counterparts the cluster can be easily phase transferred into organic solvents with the use of TOABr. This transfer does not affect the core structure as the absorbance spectrum stays consistent. Electrochemically various redox features can be observed in water including a significant ligand oxidation peak. A 1.73 V HOMO-LUMO gap was calculated for the cluster. Further work including mass spectrometry is needed to fully characterize the composition of the cluster.

5.1 Background and Research Strategy

Noble metal nanoclusters have been heavily studied over the past few decades due to their unique optical and electrochemical properties and their definite compositions and structures, and the relative stability enabling their use in many applications including biosensing, drug delivery, biological imaging, and much more[147-151]. The research has focused primarily on gold nanoclusters due to their superior stability, low cytotoxicity, and high near-IR luminescence. Various "magic number" gold nanoclusters are readily made and understood including the likes of Au_{25}, Au_{38}, Au_{130}, $Au_{144,}$ and many others[12, 27, 31, 72, 74, 138, 152-153]. Silver on the other hand has taken an overall backseat to its gold counterparts though it remains an important piece of noble-metal nanocluster research. One of the major drawbacks was always its susceptibility to oxidation and therefore lack of any reliable stability, but this has changed in recent years. Another issue with many silver nanoclusters are their cytotoxicity and negative impacts on many forms of life including man plants and animals[154-157]. This however has not

stopped the usage of silver clusters in many applications including water treatment, biomedical, and many various industries[98-101].

Early work done on small fluorescent silver nanoclusters by Henglein and Dickson allowed for an increased interest in these types of noble metal clusters[93-94]. Henglein's work included a colloidal silver nanocluster protected by citrate. This was synthesized by irradiating the solution over time with a commercial ^{60}Co γ source. While irradiating the solutions a color change to yellow and the observation of a plasmon absorption band was noted. The synthesis was completed once the plasmon band had stopped increasing. Dickson on the other hand used luminescence microscopy and spectroscopy to look at the photoactivated emission for nanoscale silver oxide. It was shown that single nanoparticle blinking and emission patters could be observed but also large-scale color changes could be seen from the same nanoparticle. Their work helped to pioneer the silver nanocluster field early on and increased the interest in exploring more of what these clusters could do and be used for. Since then the field has grown by leaps and bounds and more and exciting discoveries have been made.

Several examples of stable, monodispersed Ag nanoclusters were synthesized and characterized in and around 2010 that showed these clusters are viable and can as useful as their gold counterparts including a single-stage synthesis of glutathione/captopril clusters, a superstable 25 kDa cluster, $Ag_{44}SR_{304}$ supercomplex and a ultrastable $M_4Ag_{44}(p\text{-}MBA)_{30}$ cluster [155, 158-161]. These clusters show very particular and intense absorbance spectra and relative lack of the need of size sorting leading to an easy synthesis and purification. Due to this the Ag_{44} cluster in particular reported by Anil Desireddy was one of the first Ag clusters where a complete crystal structure was determined[161]. More recently, crystal structures were determined for the Ag_{23} and Ag_{146} clusters by the Jin group[162-163]. The $Ag_{146\ cluster}$ is particularly interesting as it shows an

observable optical band gap and electron dynamics that are power-independent concluding that it is molecular-like and not something more plasmonic. Both clusters show distinct optical features including multiple absorbance peaks and in the case of the Ag_{23} cluster near-IR luminescence.

In this chapter the previous research done on gold nanoclusters with the use of lipoic acid as the protecting ligand is used in the synthesis of a new, stable silver nanocluster with distinct absorbance bands and relative high luminescence. One concern with using this ligand however was its ability to oxidize readily during purification or even just over time. This could adversely affect the silver core due to silver's own ability to oxidize readily which could decompose the cluster and cause concerns with its overall stability. Absorbance and luminesce properties were studied in both water and in organic solvents with the use of phase transferring. Like with previous samples this was assisted with the use of TOABr as the phase transfer agent. Proton NMR characterizations were used to make sure free thiols were removed after purification was performed. Due to lipoic acids ability to oxidize, FT-IR was used to determine if the ligand would be oxidized and how this oxidation could be prevented. Finally, basic electrochemical analysis was performed on the cluster to explore how the silver cluster would react differently from its gold counterparts. This again was performed in both water and organic solvents.

5.2 Results and Discussion

5.2.1 Optical Characterizations

The Ag-LA nanocluster was synthesized following a similar method previously published for the $Au_{22}LA_{12}$ cluster[25]. Briefly, $AgNO_3$ and LA (1:3 ratio) were separately dissolved in 2 mL of nanopure water. NaOH was added dropwise to the LA solution in order to get it to fully dissolve. Once dissolved it was added to the $AgNO_3$ solution and precipitates immediately formed. This was solved by adding in more NaOH dropwise until everything dissolved and a

clear solution was obtained. This was allowed to stir for 3 hours at room temperature. Afterwards a 5x solution of $NaBH_4$ was added under heavy stirring and the mixture was allowed to react for around 4.5 hours, or until the luminescence intensity peaked and leveled out. The end solution was then purified by either dialysis or by centrifugation. If centrifuged the final solution was then purged with argon and kept in the refrigerator at 4°C for storage. This was done to keep the cluster from being oxidized. Figure 5.1 shows the optical features during synthesis and after purification with dialysis.

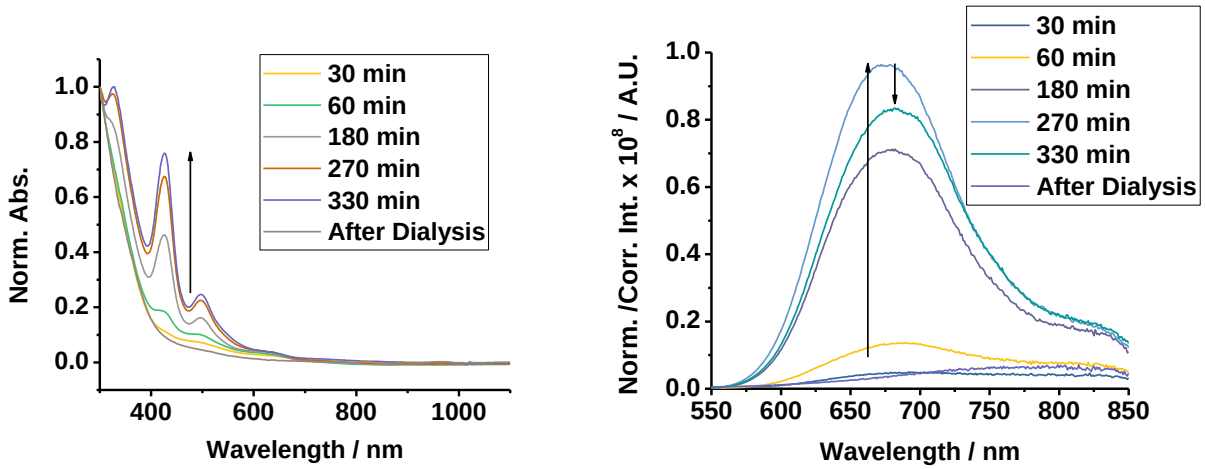

Figure 5.1. UV-Vis and Luminescence spectra for the Ag-LA cluster. Absorbance was normalized to at 300 nm and the luminescence was normalized by the absorbance value at the excitation (400 nm).

The absorbance spectrum throughout the synthesis shows the formation of three major optical bands at 326, 426, and 500 nm with a slight shoulder at 640 nm. The peaks at 426 and 500 nm and the shoulder at 640 nm occur very quickly during the synthesis (around 30 minutes) though the peak at 326 nm doesn't start to show until around 120 minutes and becomes more prominent thereafter. The luminescence observed increases during the synthesis until 270 minutes and then starts to decline afterwards. These sharp absorbance features are quite similar to what was observed with other silver clusters such as the Ag_{44} and AgSG clusters[155, 160-161]. The

peaks are at different wavelength corresponding to different electronic transition states, so it can be concluded that this new cluster is not the same as any of these clusters. Figure 5.2 shows the excitation curve for the cluster along with emission curves at each excitation peak. The excitation scan looks similar to that absorbance spectrum. This has been noted in other silver cluster systems. Overall the emission curves do not show much change other than insignificant changes in the intensity. The curve when exciting at 495 nm shows an increased initial baseline. If this were to be corrected its increase in intensity would most likely be negated and it would fall in line with the other two measurements.

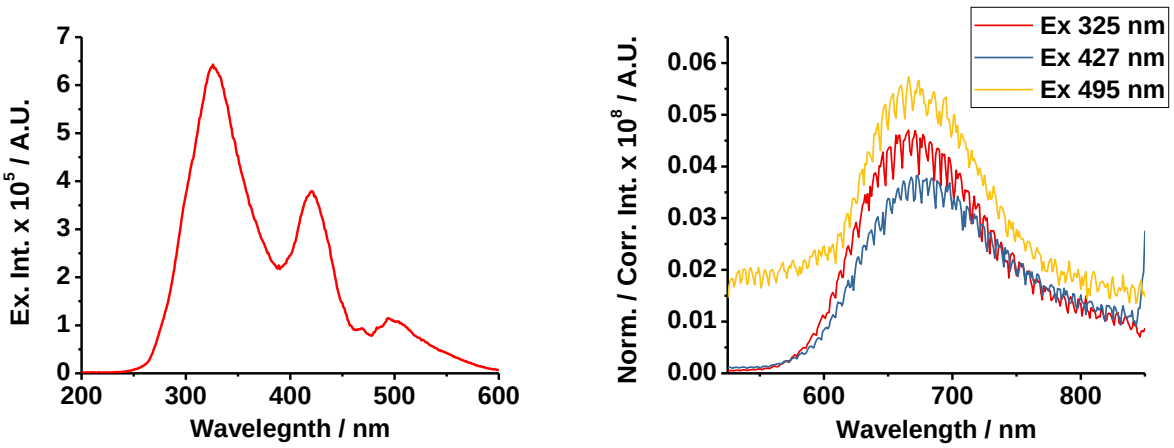

Figure 5.2. Excitation spectrum (left) and emission spectra (right) for the Ag-LA cluster. Emission spectra were normalized at each spectrum's respective excitation wavelength's absorbance value.

Figure 5.3 shows the absorbance values for each of the three main absorbance features and luminescence intensity throughout the duration of the synthesis. As seen in the figure the peaks at 327, 427, and 498 nm have a linear increase over time and may start to level off towards the end of the synthesis.

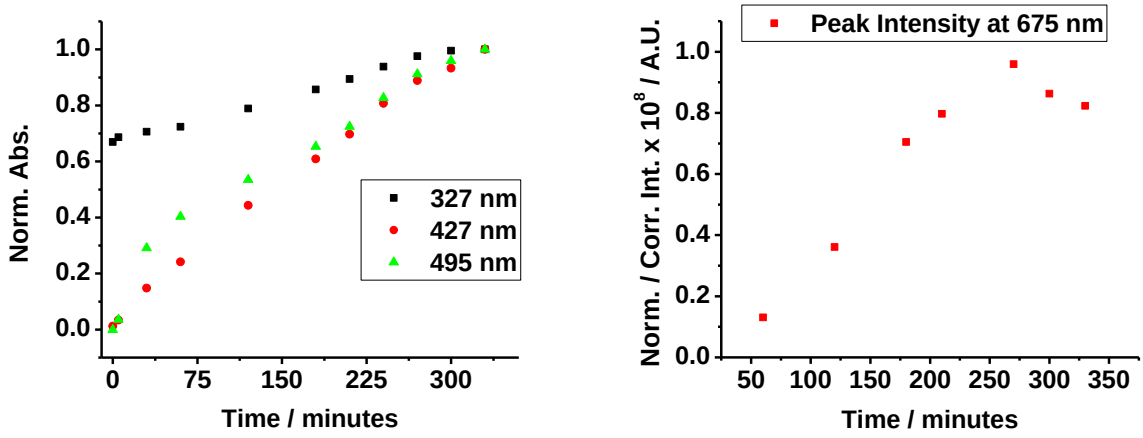

Figure 5.3. Peak absorbance and luminescence values throughout the synthesis. Absorbance values are normalized at the 330-minute peak absorbance. Luminescence was normalized at the absorbance value of the excitation wavelength (400 nm).

One major challenge is the changes in absorbance and luminescence during the purification via dialysis. All absorbance peaks and the photoluminescence diminish nearly 100%. The absorbance features becoming less apparent is not hugely surprising as both the previous $Au_{22}LA_{12}$ cluster and Au-LA (1-1.7 ratio) cluster showed a decrease in absorbance features once the sample oxidized. What was surprising was the significant decrease in luminescence intensity. With previous samples an increase of 4-5 times was seen after purification with dialysis along with the oxidation of sulfur on the LA ligands. The results suggest that the oxidation likely affects the silver core which had a negative impact on the clusters. To retain the optical features, the newly synthesized clusters were directly precipitated with methanol from the reaction mixture and then purged with argon to suppress oxygen exposure or oxidation. Figure 5.4 shows the effects of argon purging after synthesis.

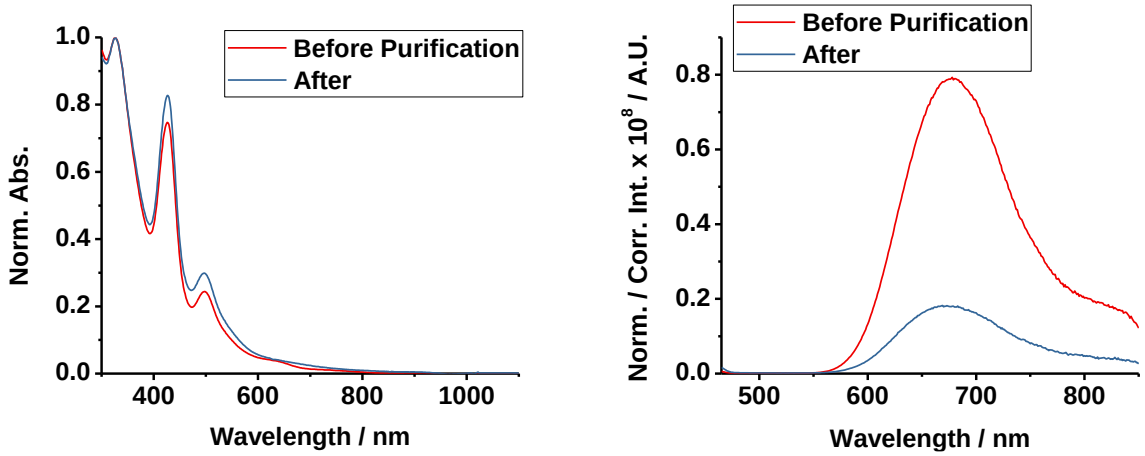

Figure 5.4. UV-Vis and Luminescence spectra after argon purging. Absorbance was normalized to at 300 nm and the luminescence was normalized by the absorbance value at the excitation (400 nm).

Purging was obviously effective but does seem to have the perfect effect of keeping the absorbance features along with keeping a higher luminescence intensity at 100%. The results strongly support the hypothesis that oxygen was the root cause that should be better controlled in future synthesis and purification. Considering the carboxylic group on the lipoic acid that affect the photoluminescence of other clusters, the optical properties were studied under pH variation. PBS buffers at different pHs were used to check the absorbance and luminescence spectra. Figure 5.5 shows the absorbance and luminescence spectra at the different pH values. The emission intensity is higher at higher pHs, about twice at pH 9.0 compared to pH 6.5. This significant increase is quite surprising as only small increases toward more basic pH have been noted with Au LA clusters. Small shifts in the luminescence peak wavelength can also be observed though they are minor. In the absorbance spectra small differences can be noted in the height of the peaks, but overall the curvature and shape are similar. In PBS pH 3.5 (results not shown), a significant increase in the baseline of the absorbance measurement corresponding to the sample precipitation in the lower pH.

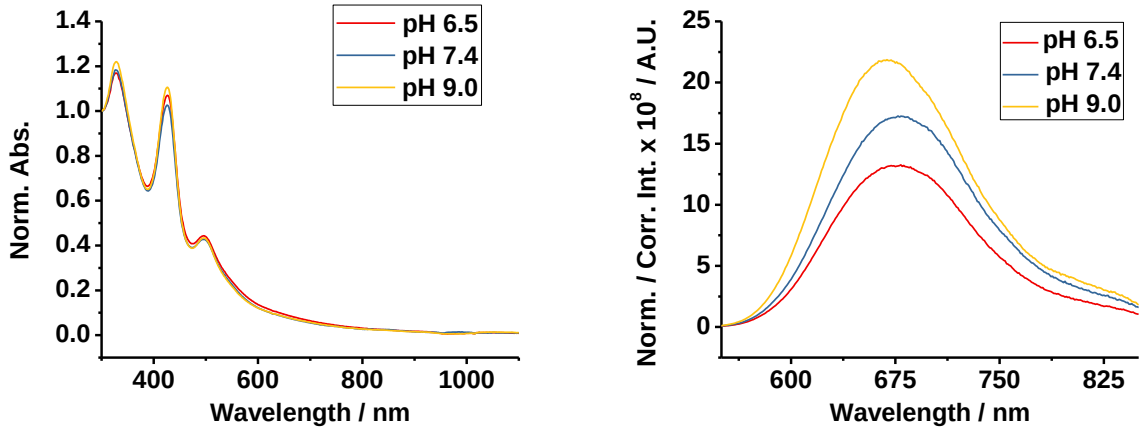

Figure 5.5. Absorbance and luminescence spectra at different pH values. Absorbance was normalized to at 300 nm and the luminescence was normalized by the absorbance value at the excitation (400 nm). Each sample was prepared by taking 50 uL of a bulk solution and diluting with 3 mL of each PBS buffer.

Like with other cluster samples the ability to phase transfer this cluster was explored to enable analysis in organic solvents. The sample was transferred similarly to all of the previous gold nanolcusters. The Ag- LA was first dissolved in water and toluene was added on top. To this 0.01 M TOABr was added in 100 uL increments until almost all of the sample was transferred. A small amount of sample was left in the aqueous phase to avoid introducing excess TOABr in the organic solution. Once the phase boundary is re-established after mixing/transfer, the organic phase was collected by pipetting away from the aqueous phase. The sample could then be dried and redissolved in various organic solvents as needed. This process took under 10 minutes, so a slight oxidation could affect future measurements. Figure 5.6 shows comparison of the absorbance and luminescence spectra in water and toluene.

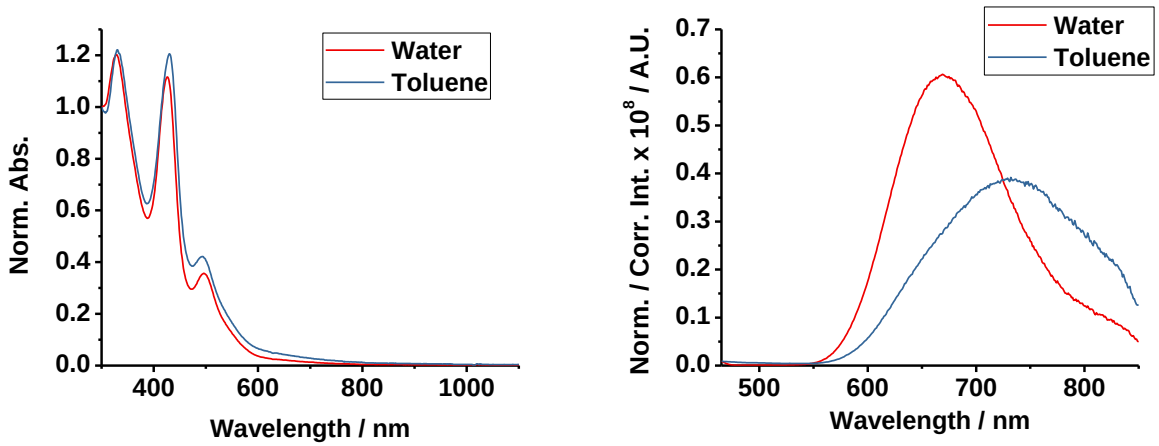

Figure 5.6. Comparison of UV-Vis and luminescence spectra in water and toluene. Absorbance was normalized to at 300 nm and the luminescence was normalized by the absorbance value at the excitation (400 nm).

The absorbance spectra of the Ag-LA clusters showed little to no change after phase transferring into toluene. This is similar to what is seen in previously transferred samples. The luminescence on the other hand is quite different compared to the transferred gold clusters. One difference is there is no major increase in luminescence intensity and in fact an overall decrease is observed. This could be due to the fact the sample may have oxidized before and during the transfer process. Also, it is possible that the silver core is not as affected by the rigidifying of the monolayer compared to the previously transferred gold clusters. The biggest difference however is the major red shift and overall broadening that is seen in the luminescence after the transfer. Little to no shift in the luminescence peak was noted in any of the gold clusters so this shift is quite interesting and requires further investigation.

5.2.2 IR Characterizations

The IR characterizations of the centrifuged sample (un/less oxidized), centrifuged sample after exposure to air over a week (oxidized), and the fully oxidized sample (over 3 days dialysis) are shown in Figure 5.7. Not surprisingly this new Ag-LA sample display similar features that

were seen with the previously published. Like with the Au_{22} sample two peaks that match up closely with the S=O symmetric and asymmetric stretching bands in alkysulfonic acid/sulfonate species (1042 cm^{-1} and 1179 cm^{-1}) show up slightly in the oxidized centrifuge sample and are apparent in the sample that underwent dialysis. For the Ag-LA sample these peaks show up at 1043 cm^{-1} and 1177 cm^{-1} and are represented by a dashed line in Figure 5.5. It can be concluded that like with the Au_{22} sample some of the sulfur atoms are being oxidized during dialysis and can slowly oxidize if the sample is used and not again purged with argon after use. The purging does seem to be effective in controlling this oxidization as the purged and sealed Ag-LA sample did not show any signs of these two features. Another concern that can be removed is if one of the sulfurs during synthesis is reduced into a thiol instead of actually attaching to the Ag core. This concern is negated by the fact that S-H stretching which would appear around 2500 cm^{-1} is not seen in the any of the IR spectrums so it can be concluded that this process is not happening. The three peaks to the left of the 1177 cm^{-1} peak (1642, 1550, and 1405 cm^{-1}) are due to carbonyl stretching and asymmetric/symmetric carboxylate stretching. Finally, the peak around 1000 cm^{-1} is related to synthetic byproducts such as boronic species or excess ligands. Most likely the sample was not fully purified before taking the measurement.

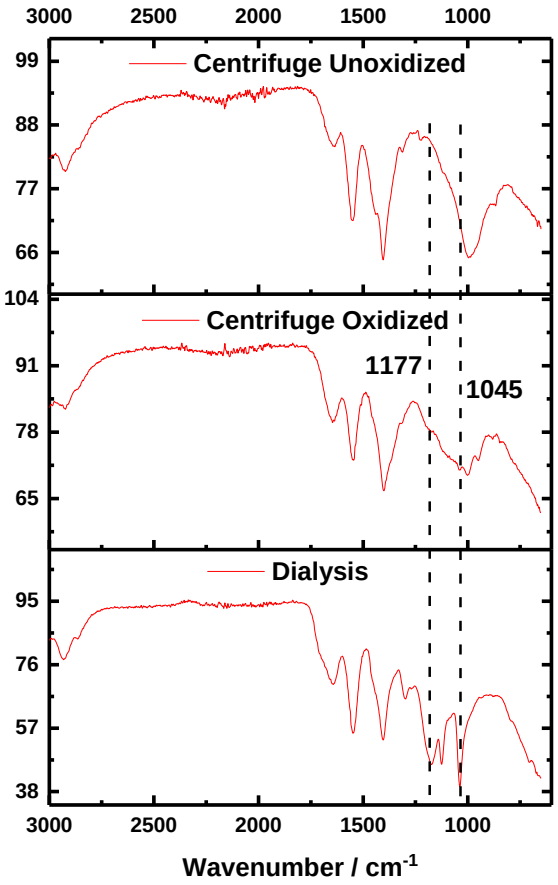

Figure 5.7. IR Spectra for the Unoxidized, Oxidized, and Dialysis Ag-LA samples.

5.2.3 Electrochemical Characterizations

Aqueous electrochemical measurements were performed on the unoxidized sample using 0.1 M $NaClO_4$ as the supporting electrolyte. A potential window of -1.2 to 1.2 V was used to avoid significant background water splitting current signal. Figure 5.8 shows the full potential range CV for the unoxidized sample. Some similar features that were observed with previous Au-LA clusters were noticeable including an obvious ligand oxidation peak. This feature was slightly shifted less positive to 0.8 V and looks to be slightly reversible as a small peak can be observed at 0.81 V in reduction scan SWV. Other features in oxidation scan SWV include peaks

at -0.82, 0.12, and a small shoulder at 1.06 V. The features at -0.93 and -0.09 in reduction scan are most likely correlated with the oxidation features at -0.82 and 0.12 V. The redox activities around zero V, irreversible oxidation in CV and the 0.12/-0.09 peaks in SWV, is postulated to be irreversible oxidation at Ag-S interface that needs to be confirmed. Using the +0.80 V oxidation and -0.93 reduction peaks, a spacing of 1.73 V can be calculated for the HOMO-LUMO spacing. This spacing is in line with a calculated optical gap using the UV-Vis measurement.

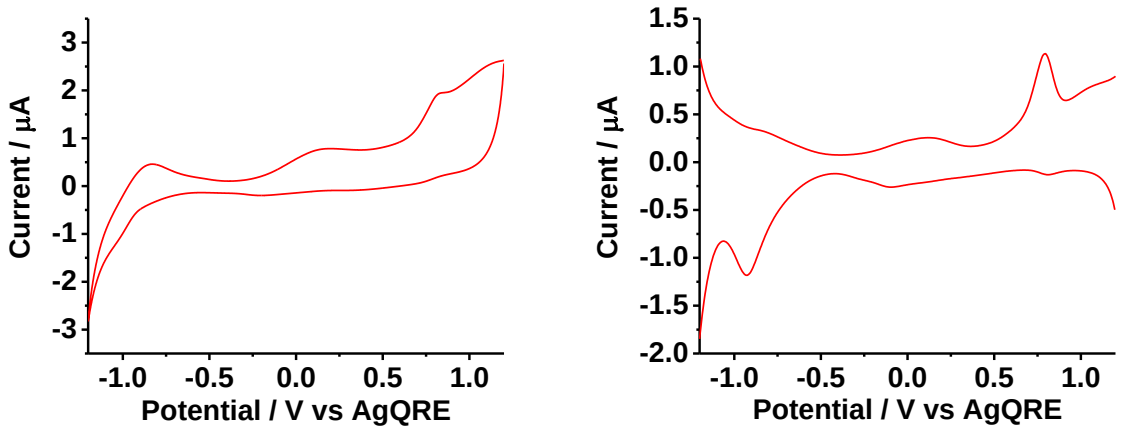

Figure 5.8. CV and SWV of the Ag-LA unoxidized cluster in water. Purging with Ar for 15-30 mins with 0.1 M $NaClO_4$ as the supporting electrolyte. A 0.2 mm platinum disk working electrode, platinum foil counter, and an Ag/AgCl wire were used for all measurements.

Measurements using a limited potential window of -1.2 to -0.4 V and -0.4 to 1.2 V respectively were also performed to see if any of the peaks relied on other oxidation/reduction processes. By limiting these potential windows, it was observed that most of the main features seem to be independent of one another. The oxidation/reduction features in the positive potential range still appear if the window is limited to -0.4 V. The redox activities in the negative potential range are still observed if the positive oxidation features are not activated though they do appear to less prominent. Figure 5.9 shows the limited window CVs for the positive and negative potential ranges.

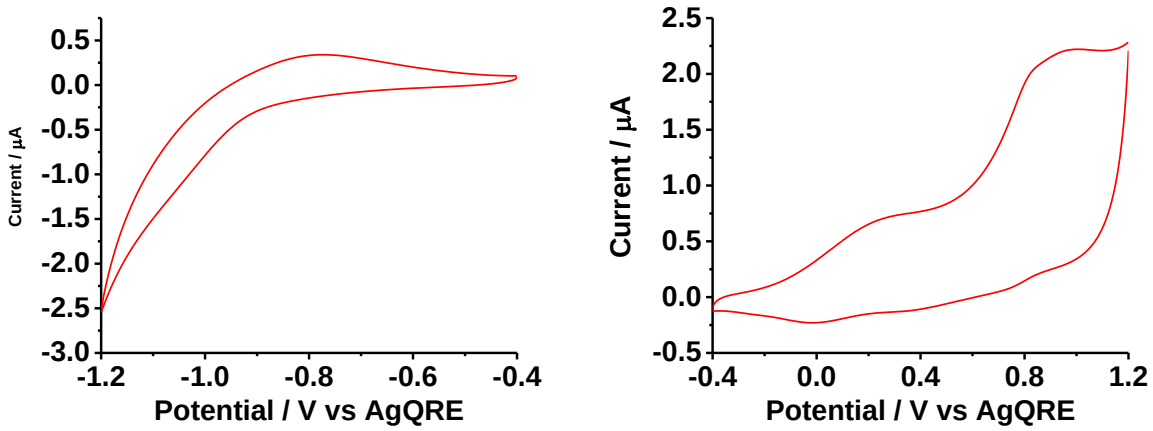

Figure 5.9. Limited potential window CVs for the Ag-LA cluster in water. Purging with Ar for 15-30 mins with 0.1 M $NaClO_4$ as the supporting electrolyte. A 0.2 mm platinum disk working electrode, platinum foil counter, and an Ag/AgCl wire were used for all measurements.

Electrochemical characterizations of the most oxidized dialysis sample are shown in Figure 5.10. The voltammograms between the unoxidized and oxidized samples are quite similar with features including a noticeable ligand oxidation feature and a noticeable reduction feature in the negative potential range. The irreversible oxidation near zero is almost absent, consistent with the pre-oxidation during purification or sample preparation. Accordingly, the reduction around -0.03 V becomes more distinct. Overall major differences in the electrochemical data was fully expected due to the previous results in the Au-LA (1-1.7 ratio) sample. For that cluster, only minor differences were noted including a slight intensity change involving the ligand oxidation peak.

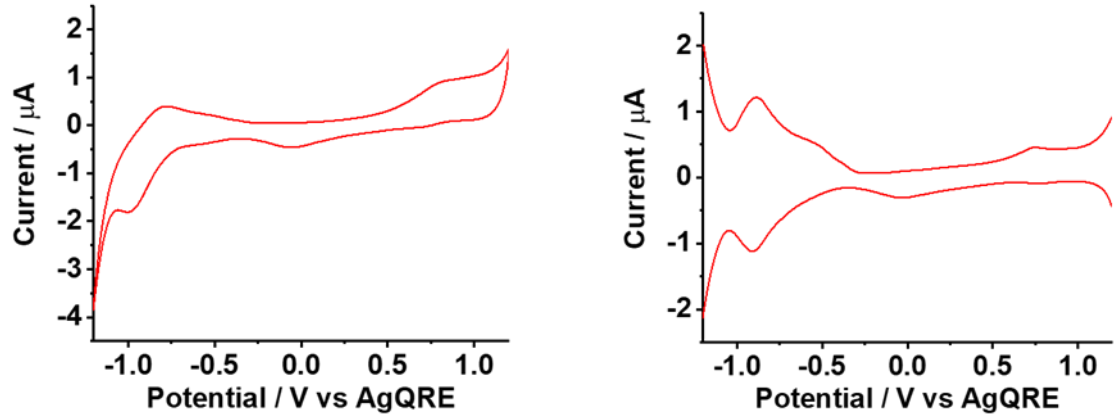

Figure 5.10. CV and SWV of the oxidized Ag-LA cluster in H_2O. Purging with Ar for 15-30 mins with 0.1 M $NaClO_4$ as the supporting electrolyte. A 0.2 mm platinum disk working electrode, platinum foil counter, and an Ag/AgCl wire were used for all measurements.

The main features in oxidation scan SWV can be observed at -0.88, -0.54, -0.37, and 0.75 V. The features in reduction scan SWV can be observed at -0.91, -0.04, and 0.76 V. A few main differences including the two new reduction features at -0.54 and -0.37 V along with the missing oxidation feature at 0.12 V and 1.06 V. The other main difference is a shift slightly less positive of the ligand oxidation. The unoxidized sample shows the peak at 0.8 V where as for the oxidized sample this peak has moved to 0.75 V for a 50 mV difference. This is not a huge shift but something to keep mind. The peak is also not as strong which is not a huge surprise since this sample should be fully oxidized at this point. This small shift also slightly effects the calculated HOMO-LUMO spacing as now it would be 1.66 V.

5.3 Experimental

5.3.1 Chemicals

All chemicals (99% or higher) were purchased from Aldrich. Toluene was purchased from Fisher-Science, and nanopure water was produced in-house (>18 Mcm-1).

5.3.2 Instruments

UV-Vis spectra were recorded with a Shimadzu UV-1700 spectrophotometer. NMR spectra were collected with a Bruker NMR 400 MHz spectrometer. Infrared spectra were acquired on a PerkinElmer Spectrum 100 FT-IR spectrometer. Electrochemical measurements were performed on a CH Instruments (CHI 750C) with Picoamp booster in Faraday Cage. The solution was generally purged over 15-30 mins with Ar prior to electrochemical measurements. The potential of the AgQRE (0.22 V vs. SHE) was calibrated periodically by measuring the ferrocene (Fc+/Fc) redox peak at 0.48 V.

5.3.3 Ag-LA Synthesis

$AgNO_3$ and LA (1:3 ratio) were separately dissolved in 2 mL of nanopure water. A 0.5 M NaOH solution was then added dropwise to the LA solution until the LA solution became clear. The LA solution was then added to the $AgNO_3$ solution and precipitates immediately formed after brief stirring. Additional 0.5 M NaOH solution was added dropwise until everything dissolved and a clear solution was obtained. This solution was mixed under mild stirring for 3-4 hours at room temperature. Next a 5x solution of $NaBH_4$ was dissolved in 2 mL of nanopure water and added under rigorous stirring. This new solution was then allowed to react until the luminescence intensity peaked and leveled out. This end solution was then purified by either dialysis or by centrifugation. In dialysis, a 3500 MWCO dialysis tubing was used for 3-4 days. The water was changed out every 4-6 hours during this time. If the sample was centrifuged the bulk solution was dried down to around 1 mL. This was then precipitated with the addition of methanol and centrifuged to pull out any excess thiols from the precipitates. This was done 3-4 times and the final precipitates were collected by dissolving in water. This final solution was

then purged with argon and stored in the fridge. This was done to keep the cluster from oxidizing and to keep the optical features as consistent as possible.

5.3.4 Phase Transfer

During a typical transfer of the clusters, the Ag-LA is dissolved in 1-2 mL of water. Next, 2 mL of toluene is added on top and an approximate stoichiometry amount of TOABr is used so there would be no significant excess TOA^+ in solution when performing future electrochemical experiments or ^1H NMR. A mild shaking was sufficient to fully transfer the Ag-LA clusters. Afterwards the mixture is allowed to settle in order to re-establish the phase boundary so that it is easier to separate out the transferred clusters from the aqueous phase.

5.4 Summary

In summary, a new Ag-LA cluster has been synthesized and its optical and electrochemical properties have been characterized. Optically it has 3 absorption peaks at 326, 426, and 500 nm with a slight shoulder at 640 nm, along with an optical band gap of xx. These features occur very quickly during the synthesis and the synthesis is stopped normally at around 4.5 hours when (immediately before) a drop in the luminescence intensity is noticed. Two purification routes have been adopted. One is by using dialysis over a period of three days. This route gives way to a significant drop in luminescence intensity as well as a total loss of the absorbance features. The loss in absorbance features can be contributed to the oxidation during dialysis as this has been noted in the previously synthesized $Au_{22}LA_{12}$ cluster. Purifying the sample with the use of centrifugation and methanol while then purging with argon afterwards is much more effective at retaining the absorbance features as well as keeping a higher luminescence intensity. This is most likely due to the suppression of gradual oxidation by oxygen. Overall the proton NMR looks very similar to that of the Au22LA12 and Au-LA (1-1.7)

clusters. IR spectra help to conclude that like with the Au clusters the lipoic acid goes through an oxidation process during dialysis. This can be concluded with the fact that bands can be observed at 1045 and 1177 cm-1 which are very similar to those seen with the S=O symmetric and asymmetric stretching bands in alkysulfonic acid/sulfonate species. Electrochemically the sample does show some redox activities throughout the potential window afforded by water. In the unoxidized sample a large ligand oxidation peak is observed along with some smaller features. As the sample is oxidized this peak does seem to decrease as shown in the oxidized samples CV and SWV. Further structural work will be needed before any compositional conclusions can be made.

6 CONCLUSIONS AND MAJOR DISCOVERIES

In conclusion, the work reported in this PhD dissertation focused on the optical and electrochemical characterizations of monolayer-protected noble metal nanoclusters. Specifically, the ability to phase transfer aqueous soluble clusters into organic solvents enables the observation under broader conditions to better understand their properties. By using TOABr as a phase transfer agent the $Au_{22}LA_{12}$, Au-MSA, Au-LA (1-1.7 ratio), and Ag-LA clusters were easily phase transferred into various organic solvents. Optically this transfer showed little to no change in the absorbance features of all of the nanoclusters. This would imply that no major core rearrangement was occurring during the phase transfer. With regards to the photoluminescence all gold clusters showed a significant increase in the emission intensity when transferred. The Ag-LA cluster was different in this regard as a slight decrease was noted though this could be due to the quick oxidation of the silver core. Another advantage given by this phase transfer is the ability to use a much large window for electrochemical analysis. Water has a very small potential window and because of this many redox activities could not be resolved. Transferring

into organic solvents such as acetonitrile increases the potential window substantially which enables the observations of redox activities that went unseen or were poorly defined in water. The one challenge is the Br^- counterion for TOA^+. This is electrochemically active, so care must be taken to ensure that it does not interfere in any measurements. Further work could be done with other transfer agents to see how they affect the optical features and if one could be used that would be electrochemically inactive.

Separately, a complete energy diagram was proposed for the Au_{130}(p-MBT)$_{40}$ cluster synthesized by the Jin group. Electrochemical analysis along with spectroelectrochemical changes were used to aid in the piecing together of where the absorbance features come from and how the various energy states are aligned. The newly resolved spectroelectrochemical features and increasing/decreasing of the steady state absorbance bands during oxidation/reduction agreed with the ESA and GSB bands observed during ultrafast measurements.

REFERENCES

1. Baker, M., Nanotechnology imaging probes: smaller and more stable. *Nat Meth* **2010,** *7* (12), 957-962.
2. Zhang, J.; Fu, Y.; Conroy, C. V.; Tang, Z.; Li, G.; Zhao, R. Y.; Wang, G., Fluorescence Intensity and Lifetime Cell Imaging with Luminescent Gold Nanoclusters. *The Journal of Physical Chemistry C* **2012,** *116* (50), 26561-26569.
3. Polavarapu, L.; Manna, M.; Xu, Q.-H., Biocompatible glutathione capped gold clusters as one- and two-photon excitation fluorescence contrast agents for live cells imaging. *Nanoscale* **2011,** *3* (2), 429-434.
4. Li, G.; Jin, R., Atomically Precise Gold Nanoclusters as New Model Catalysts. *Accounts of Chemical Research* **2013,** *46* (8), 1749-1758.
5. Treuel, L.; Jiang, X.; Nienhaus, G. U., New views on cellular uptake and trafficking of manufactured nanoparticles. *Journal of The Royal Society Interface* **2013,** *10* (82).
6. Brust, M.; Walker, M.; Bethell, D.; Schiffrin, D. J.; Whyman, R., Synthesis of thiol-derivatised gold nanoparticles in a two-phase Liquid-Liquid system. *Journal of the Chemical Society, Chemical Communications* **1994,** *0* (7), 801-802.
7. Brust, M.; Fink, J.; Bethell, D.; Schiffrin, D. J.; Kiely, C., Synthesis and reactions of functionalised gold nanoparticles. *Journal of the Chemical Society, Chemical Communications* **1995,** (16), 1655-1656.

8. Negishi, Y.; Takasugi, Y.; Sato, S.; Yao, H.; Kimura, K.; Tsukuda, T., Magic-Numbered Aun Clusters Protected by Glutathione Monolayers (n = 18, 21, 25, 28, 32, 39): Isolation and Spectroscopic Characterization. *Journal of the American Chemical Society* **2004,** *126* (21), 6518-6519.
9. Chen, Y.; Zeng, C.; Kauffman, D. R.; Jin, R., Tuning the Magic Size of Atomically Precise Gold Nanoclusters via Isomeric Methylbenzenethiols. *Nano Letters* **2015,** *15* (5), 3603-3609.
10. Jin, R.; Zeng, C.; Zhou, M.; Chen, Y., Atomically Precise Colloidal Metal Nanoclusters and Nanoparticles: Fundamentals and Opportunities. *Chemical Reviews* **2016,** *116* (18), 10346-10413.
11. Zeng, C.; Chen, Y.; Das, A.; Jin, R., Transformation Chemistry of Gold Nanoclusters: From One Stable Size to Another. *The Journal of Physical Chemistry Letters* **2015,** *6* (15), 2976-2986.
12. Jin, R.; Zhou, M.; Zeng, C.; Song, Y.; Padelford, J. W.; Wang, G.; Sfeir, M. Y.; Higaki, T., On the Non-Metallicity of 2.2 nm Au246(SR)80 Nanoclusters. *Angewandte Chemie International Edition*, n/a-n/a.
13. Conroy, C. V.; Jiang, J.; Zhang, C.; Ahuja, T.; Tang, Z.; Prickett, C. A.; Yang, J. J.; Wang, G., Enhancing near IR luminescence of thiolate Au nanoclusters by thermo treatments and heterogeneous subcellular distributions. *Nanoscale* **2014,** *6* (13), 7416-23.
14. Wang, S.; Meng, X.; Das, A.; Li, T.; Song, Y.; Cao, T.; Zhu, X.; Zhu, M.; Jin, R., A 200-fold Quantum Yield Boost in the Photoluminescence of Silver-Doped AgxAu25−x Nanoclusters: The 13 th Silver Atom Matters. *Angewandte Chemie International Edition* **2014,** *53* (9), 2376-2380.
15. Tracy, J. B.; Crowe, M. C.; Parker, J. F.; Hampe, O.; Fields-Zinna, C. A.; Dass, A.; Murray, R. W., Electrospray Ionization Mass Spectrometry of Uniform and Mixed Monolayer Nanoparticles: Au25[S(CH2)2Ph]18 and Au25[S(CH2)2Ph]18-x(SR)x. *Journal of the American Chemical Society* **2007,** *129* (51), 16209-16215.
16. Dass, A.; Stevenson, A.; Dubay, G. R.; Tracy, J. B.; Murray, R. W., Nanoparticle MALDI-TOF Mass Spectrometry without Fragmentation: Au25(SCH2CH2Ph)18 and Mixed Monolayer Au25(SCH2CH2Ph)18−x(L)x. *Journal of the American Chemical Society* **2008,** *130* (18), 5940-5946.
17. Hostetler, M. J.; Wingate, J. E.; Zhong, C.-J.; Harris, J. E.; Vachet, R. W.; Clark, M. R.; Londono, J. D.; Green, S. J.; Stokes, J. J.; Wignall, G. D.; Glish, G. L.; Porter, M. D.; Evans, N. D.; Murray, R. W., Alkanethiolate Gold Cluster Molecules with Core Diameters from 1.5 to 5.2 nm: Core and Monolayer Properties as a Function of Core Size. *Langmuir* **1998,** *14* (1), 17-30.
18. Song, Y.; Huang, T.; Murray, R. W., Heterophase Ligand Exchange and Metal Transfer between Monolayer Protected Clusters. *J. Am. Chem. Soc.* **2003,** *125* (38), 11694-11701.
19. Dass, A.; Guo, R.; Tracy, J. B.; Balasubramanian, R.; Douglas, A. D.; Murray, R. W., Gold Nanoparticles with Perfluorothiolate Ligands. *Langmuir* **2008,** *24* (1), 310-315.
20. Kohlmann, O.; Steinmetz, W. E.; Mao, X.-A.; Wuelfing, W. P.; Templeton, A. C.; Murray, R. W.; Johnson, C. S., NMR Diffusion, Relaxation, and Spectroscopic Studies of Water Soluble, Monolayer-Protected Gold Nanoclusters†. *The Journal of Physical Chemistry B* **2001,** *105* (37), 8801-8809.
21. Shon, Y.-S.; Wuelfing, W. P.; Murray, R. W., Water-Soluble, Sulfonic Acid-Functionalized, Monolayer-Protected Nanoparticles and an Ionically Conductive Molten Salt Containing Them. *Langmuir* **2001,** *17* (4), 1255-1261.

22. Donkers, R. L.; Song, Y.; Murray, R. W., Substituent Effects on the Exchange Dynamics of Ligands on 1.6 nm Diameter Gold Nanoparticles. *Langmuir* **2004,** *20* (11), 4703-4707.
23. Bhattacharya, S.; Srivastava, A., Synthesis and Characterization of Novel Cationic Lipid and Cholesterol-Coated Gold Nanoparticles and Their Interactions with Dipalmitoylphosphatidylcholine Membranes. *Langmuir* **2003,** *19* (10), 4439-4447.
24. Dorris, A.; Rucareanu, S.; Reven, L.; Barrett, C. J.; Lennox, R. B., Preparation and Characterization of Polyelectrolyte-Coated Gold Nanoparticles. *Langmuir* **2008,** *24* (6), 2532-2538.
25. Jiang, J.; Conroy, C. V.; Kyetny, M. M.; Lake, G. J.; Padelford, J. W.; Ahuja, T.; Wang, G., Oxidation at the Core-Ligand Interface of Au Lipoic Acid Nanoclusters That Enhances the Near-IR Luminescence. *Journal of Physical Chemistry C* **2014,** *118* (35), 20680-20687.
26. Ahuja, T.; Wang, D.; Tang, Z.; Robinson, D. A.; Padelford, J. W.; Wang, G., Electronic coupling between ligand and core energy states in dithiolate-monothiolate stabilized Au clusters. *Physical Chemistry Chemical Physics* **2015,** *17* (29), 19342-19349.
27. Tang, Z.; Robinson, D. A.; Bokossa, N.; Xu, B.; Wang, S.; Wang, G., Mixed Dithiolate Durene-DT and Monothiolate Phenylethanethiolate Protected Au130 Nanoparticles with Discrete Core and Core-Ligand Energy States. *Journal of the American Chemical Society* **2011,** *133* (40), 16037-16044.
28. Jupally, V. R.; Thrasher, J. G.; Dass, A., Quantized double layer charging of Au130(SR)50 nanomolecules. *Analyst* **2014,** *139* (8), 1826-1829.
29. Kwak, K.; Lee, D., Electrochemical Characterization of Water-Soluble Au25 Nanoclusters Enabled by Phase-Transfer Reaction. *The Journal of Physical Chemistry Letters* **2012,** *3* (17), 2476-2481.
30. García-Raya, D.; Madueño, R.; Blázquez, M.; Pineda, T., Electrochemistry of Molecule-like Au25 Nanoclusters Protected by Hexanethiolate. *The Journal of Physical Chemistry C* **2009,** *113* (20), 8756-8761.
31. Lee, D.; Donkers, R. L.; Wang, G.; Harper, A. S.; Murray, R. W., Electrochemistry and Optical Absorbance and Luminescence of Molecule-like Au38 Nanoparticles. *Journal of the American Chemical Society* **2004,** *126* (19), 6193-6199.
32. Wang, D.; Padelford, J. W.; Ahuja, T.; Wang, G., Transitions in Discrete Absorption Bands of Au130 Clusters upon Stepwise Charging by Spectroelectrochemistry. *ACS Nano* **2015,** *9* (8), 8344-8351.
33. Padelford, J. W.; Zhou, M.; Chen, Y.; Jin, R.; Wang, G., Electronic Transitions in Highly Symmetric Au130 Nanoclusters by Spectroelectrochemistry and Ultrafast Spectroscopy. *The Journal of Physical Chemistry C* **2017,** *121* (39), 21217-21224.
34. Ruiz, V.; Colina, A.; Heras, M. A.; López-Palacios, J., Potential Regulation of the Spectroelectrochemical Response of Monolayer-Protected Gold Cluster Films by Electrolyte Composition. *The Journal of Physical Chemistry C* **2007,** *111* (11), 4277-4284.
35. Giersig, M.; Mulvaney, P., Preparation of ordered colloid monolayers by electrophoretic deposition. *Langmuir* **1993,** *9* (12), 3408-3413.
36. Knake, R.; Fahmi, A. W.; Tofail, S. A. M.; Clohessy, J.; Mihov, M.; Cunnane, V. J., Electrochemical Nucleation of Gold Nanoparticles in a Polymer Film at a Liquid−Liquid Interface. *Langmuir* **2005,** *21* (3), 1001-1008.
37. Azzam, T.; Eisenberg, A., Monolayer-Protected Gold Nanoparticles by the Self-Assembly of Micellar Poly(ethylene oxide)-b-Poly(ε-caprolactone) Block Copolymer. *Langmuir* **2007,** *23* (4), 2126-2132.

38. Wang, Y.; Neyman, A.; Arkhangelsky, E.; Gitis, V.; Meshi, L.; Weinstock, I. A., Self-Assembly and Structure of Directly Imaged Inorganic-Anion Monolayers on a Gold Nanoparticle. *Journal of the American Chemical Society* **2009,** *131* (47), 17412-17422.
39. Tanaka, A.; Takeda, Y.; Imamura, M.; Sato, S., Dynamic final-state effect on the Au $4f$ core-level photoemission of dodecanethiolate-passivated Au nanoparticles on graphite substrates. *Physical Review B* **2003,** *68* (19), 195415.
40. Shibu, E. S.; Muhammed, M. A. H.; Tsukuda, T.; Pradeep, T., Ligand Exchange of Au25SG18 Leading to Functionalized Gold Clusters: Spectroscopy, Kinetics, and Luminescence. *The Journal of Physical Chemistry C* **2008,** *112* (32), 12168-12176.
41. Zhu, M.; Eckenhoff, W. T.; Pintauer, T.; Jin, R., Conversion of Anionic [Au25(SCH2CH2Ph)18]− Cluster to Charge Neutral Cluster via Air Oxidation. *The Journal of Physical Chemistry C* **2008,** *112* (37), 14221-14224.
42. Jadzinsky, P. D.; Calero, G.; Ackerson, C. J.; Bushnell, D. A.; Kornberg, R. D., Structure of a Thiol Monolayer-Protected Gold Nanoparticle at 1.1 Å Resolution. *Science* **2007,** *318* (5849), 430-433.
43. Heaven, M. W.; Dass, A.; White, P. S.; Holt, K. M.; Murray, R. W., Crystal Structure of the Gold Nanoparticle [N(C8H17)4][Au25(SCH2CH2Ph)18]. *Journal of the American Chemical Society* **2008,** *130* (12), 3754-3755.
44. Zhu, M.; Eckenhoff, W. T.; Pintauer, T.; Jin, R., Conversion of Anionic [Au25(SCH2CH2Ph)18]鋆?Cluster to Charge Neutral Cluster via Air Oxidation. *The Journal of Physical Chemistry C* **2008,** *112* (37), 14221-14224.
45. Jiang, D.-e.; Luo, W.; Tiago, M. L.; Dai, S., In Search of a Structural Model for a Thiolate-protected Au38 Cluster. *The Journal of Physical Chemistry C* **2008,** *112* (36), 13905-13910.
46. Jiang, D.-e.; Tiago, M. L.; Luo, W.; Dai, S., The "Staple" Motif: A Key to Stability of Thiolate-Protected Gold Nanoclusters. *Journal of the American Chemical Society* **2008,** *130* (9), 2777-2779.
47. Qian, H.; Eckenhoff, W. T.; Zhu, Y.; Pintauer, T.; Jin, R., Total Structure Determination of Thiolate-Protected Au38 Nanoparticles. *Journal of the American Chemical Society* **2010,** *132* (24), 8280-8281.
48. Lopez-Acevedo, O.; Tsunoyama, H.; Tsukuda, T.; Häkkinen, H.; Aikens, C. M., Chirality and Electronic Structure of the Thiolate-Protected Au38 Nanocluster. *Journal of the American Chemical Society* **2010,** *132* (23), 8210-8218.
49. Pei, Y.; Gao, Y.; Zeng, X. C., Structural Prediction of Thiolate-Protected Au38: A Face-Fused Bi-icosahedral Au Core. *Journal of the American Chemical Society* **2008,** *130* (25), 7830-7832.
50. Shichibu, Y.; Konishi, K., HCl-Induced Nuclearity Convergence in Diphosphine-Protected Ultrasmall Gold Clusters: A Novel Synthetic Route to "Magic-Number" Au13 Clusters. *Small* **2010,** *6* (11), 1216-1220.
51. Wu, Z.; MacDonald, M. A.; Chen, J.; Zhang, P.; Jin, R., Kinetic Control and Thermodynamic Selection in the Synthesis of Atomically Precise Gold Nanoclusters. *Journal of the American Chemical Society* **2011,** *133* (25), 9670-9673.
52. Zhu, M.; Qian, H.; Jin, R., Thiolate-Protected Au20 Clusters with a Large Energy Gap of 2.1 eV. *Journal of the American Chemical Society* **2009,** *131* (21), 7220-7221.
53. Nimmala, P. R.; Dass, A., Au36(SPh)23 Nanomolecules. *Journal of the American Chemical Society* **2011,** *133* (24), 9175-9177.

54. Qian, H.; Zhu, Y.; Jin, R., Isolation of Ubiquitous Au40(SR)24 Clusters from the 8 kDa Gold Clusters. *Journal of the American Chemical Society* **2010,** *132* (13), 4583-4585.
55. Tsunoyama, H.; Negishi, Y.; Tsukuda, T., Chromatographic Isolation of "Missing" Au55 Clusters Protected by Alkanethiolates. *Journal of the American Chemical Society* **2006,** *128* (18), 6036-6037.
56. Dass, A., Mass Spectrometric Identification of Au68(SR)34 Molecular Gold Nanoclusters with 34-Electron Shell Closing. *Journal of the American Chemical Society* **2009,** *131* (33), 11666-11667.
57. Balasubramanian, R.; Guo, R.; Mills, A. J.; Murray, R. W., Reaction of Au55(PPh3)12Cl6 with Thiols Yields Thiolate Monolayer Protected Au75 Clusters. *Journal of the American Chemical Society* **2005,** *127* (22), 8126-8132.
58. Chen, S.; Ingram, R. S.; Hostetler, M. J.; Pietron, J. J.; Murray, R. W.; Schaaff, T. G.; Khoury, J. T.; Alvarez, M. M.; Whetten, R. L., Gold Nanoelectrodes of Varied Size: Transition to Molecule-Like Charging. *Science* **1998,** *280* (5372), 2098.
59. Schaaff, T. G.; Shafigullin, M. N.; Khoury, J. T.; Vezmar, I.; Whetten, R. L.; Cullen, W. G.; First, P. N.; Gutiérrez-Wing, C.; Ascensio, J.; Jose-Yacamán, M. J., Isolation of Smaller Nanocrystal Au Molecules: Robust Quantum Effects in Optical Spectra. *The Journal of Physical Chemistry B* **1997,** *101* (40), 7885-7891.
60. Yu, Y.; Luo, Z.; Chevrier, D. M.; Leong, D. T.; Zhang, P.; Jiang, D. E.; Xie, J., Identification of a highly luminescent Au22(SG)18 nanocluster. *J Am Chem Soc* **2014,** *136* (4), 1246-9.
61. Jiang, J. C., Cecil V.; Kvetny, Maksim M.; Lake, Gabriel J.; Padelford, Jonathan W.; Ahuja, Tarushee; Wang, Gangli, Oxidation at the Core-ligand Interface of Au Lipoic Acid Nanoclusters that Enhances the near IR Luminescence. *The Journal of Physical Chemistry C* **2014,** *Submitted*.
62. Wang, T.; Wang, D.; Padelford, J. W.; Jiang, J.; Wang, G., Near-Infrared Electrogenerated Chemiluminescence from Aqueous Soluble Lipoic Acid Au Nanoclusters. *Journal of the American Chemical Society* **2016,** *138* (20), 6380-6383.
63. Wang, T.; Padelford, J. W.; Ma, H.; Gubitosi-Raspino, M. F.; Wang, G., Near-Infrared Electrochemiluminescence from Au Nanoclusters Enhanced by EDTA and Modulated by Ions. *ChemElectroChem* **2017**, DOI: 10.1002/celc.201700547.
64. Pyo, K.; Thanthirige, V. D.; Kwak, K.; Pandurangan, P.; Ramakrishna, G.; Lee, D., Ultrabright Luminescence from Gold Nanoclusters: Rigidifying the Au(I)–Thiolate Shell. *Journal of the American Chemical Society* **2015,** *137* (25), 8244-8250.
65. Pradeep, M. A. H. M., Aqueous to Organic Phase Transfer of Au25ClustersM. *J Clust Sci* **2009,** (20), 365-373.
66. Kwak, K.; Kumar, S. S.; Lee, D., Selective determination of dopamine using quantum-sized gold nanoparticles protected with charge selective ligands. *Nanoscale* **2012,** *4* (14), 4240-4246.
67. Murray, R. W., Nanoelectrochemistry: Metal Nanoparticles, Nanoelectrodes, and Nanopores. *Chemical Reviews* **2008,** *108* (7), 2688-2720.
68. Kumar, S. S.; Kwak, K.; Lee, D., Amperometric Sensing Based on Glutathione Protected Au25 Nanoparticles and Their pH Dependent Electrocatalytic Activity. *Electroanalysis* **2011,** *23* (9), 2116-2124.

69. Hicks, J. F.; Miles, D. T.; Murray, R. W., Quantized Double-Layer Charging of Highly Monodisperse Metal Nanoparticles. *Journal of the American Chemical Society* **2002,** *124* (44), 13322-13328.
70. Chen, S.; Murray, R. W.; Feldberg, S. W., Quantized Capacitance Charging of Monolayer-Protected Au Clusters. *The Journal of Physical Chemistry B* **1998,** *102* (49), 9898-9907.
71. Qian, H.; Jin, R., Ambient Synthesis of Au144(SR)60 Nanoclusters in Methanol. *Chemistry of Materials* **2011,** *23* (8), 2209-2217.
72. Chen, Y.; Zeng, C.; Liu, C.; Kirschbaum, K.; Gayathri, C.; Gil, R. R.; Rosi, N. L.; Jin, R., Crystal Structure of Barrel-Shaped Chiral Au130(p-MBT)50 Nanocluster. *Journal of the American Chemical Society* **2015,** *137* (32), 10076-10079.
73. Wu, Z.; Gayathri, C.; Gil, R. R.; Jin, R., Probing the Structure and Charge State of Glutathione-Capped Au25(SG)18 Clusters by NMR and Mass Spectrometry. *Journal of the American Chemical Society* **2009,** *131* (18), 6535-6542.
74. Muhammed, M. A. H.; Verma, P. K.; Pal, S. K.; Kumar, R. C. A.; Paul, S.; Omkumar, R. V.; Pradeep, T., Bright, NIR-Emitting Au23 from Au25: Characterization and Applications Including Biolabeling. *Chemistry – A European Journal* **2009,** *15* (39), 10110-10120.
75. Kwak, K.; Kumar, S. S.; Pyo, K.; Lee, D., Ionic Liquid of a Gold Nanocluster: A Versatile Matrix for Electrochemical Biosensors. *ACS Nano* **2014,** *8* (1), 671-679.
76. Masatake, H.; Tetsuhiko, K.; Hiroshi, S.; Nobumasa, Y., Novel Gold Catalysts for the Oxidation of Carbon Monoxide at a Temperature far Below 0 °C. *Chemistry Letters* **1987,** *16* (2), 405-408.
77. Li, Y.; Chen, Y.; House, S. D.; Zhao, S.; Wahab, Z.; Yang, J. C.; Jin, R., Interface Engineering of Gold Nanoclusters for CO Oxidation Catalysis. *ACS Applied Materials & Interfaces* **2018,** *10* (35), 29425-29434.
78. Dreaden, E. C.; El-Sayed, M. A., Detecting and Destroying Cancer Cells in More than One Way with Noble Metals and Different Confinement Properties on the Nanoscale. *Accounts of Chemical Research* **2012,** *45* (11), 1854-1865.
79. Torchilin, V. P.; Rammohan, R.; Weissig, V.; Levchenko, T. S., TAT peptide on the surface of liposomes affords their efficient intracellular delivery even at low temperature and in the presence of metabolic inhibitors. *Proceedings of the National Academy of Sciences* **2001,** *98* (15), 8786.
80. Dickerson, E. B.; Dreaden, E. C.; Huang, X.; El-Sayed, I. H.; Chu, H.; Pushpanketh, S.; McDonald, J. F.; El-Sayed, M. A., Gold nanorod assisted near-infrared plasmonic photothermal therapy (PPTT) of squamous cell carcinoma in mice. *Cancer Letters* **2008,** *269* (1), 57-66.
81. Dreaden, E.; El-Sayed, M.; El-Sayed, I., *Nanotechnology and Nanostructures Applied in Head and Neck Cancer*. 2011; p 373-395.
82. Jain, P. K.; Lee, K. S.; El-Sayed, I. H.; El-Sayed, M. A., Calculated Absorption and Scattering Properties of Gold Nanoparticles of Different Size, Shape, and Composition: Applications in Biological Imaging and Biomedicine. *The Journal of Physical Chemistry B* **2006,** *110* (14), 7238-7248.
83. Wang, H.; Huff, T. B.; Zweifel, D. A.; He, W.; Low, P. S.; Wei, A.; Cheng, J.-X., In vitro and in vivo two-photon luminescence imaging of single gold nanorods. *Proceedings of the National Academy of Sciences of the United States of America* **2005,** *102* (44), 15752.

84. Jung, Y.; Reif, R.; Zeng, Y.; Wang, R. K., Three-Dimensional High-Resolution Imaging of Gold Nanorods Uptake in Sentinel Lymph Nodes. *Nano Letters* **2011,** *11* (7), 2938-2943.
85. Dreaden, E. C.; Near, R. D.; Abdallah, T.; Talaat, M. H.; El-Sayed, M. A., Multimodal plasmon coupling in low symmetry gold nanoparticle pairs detected in surface-enhanced Raman scattering. *Applied Physics Letters* **2011,** *98* (18), 183115.
86. Paciotti, G. F.; Myer, L.; Weinreich, D.; Goia, D.; Pavel, N.; McLaughlin, R. E.; Tamarkin, L., Colloidal Gold: A Novel Nanoparticle Vector for Tumor Directed Drug Delivery. *Drug Delivery* **2004,** *11* (3), 169-183.
87. Paciotti, G. M., LD & Kim, TH & Wang, S & Alexander, HR & Weinreich, D & Tamarkin, Lawrence, Colloidal gold: A novel colloidal nanoparticle vector for tumor-directed drug delivery. *Clinical Cancer Research* **2001,** *7*, 3673S-3674S.
88. Libutti, S. K.; Paciotti, G. F.; Byrnes, A. A.; Alexander, H. R.; Gannon, W. E.; Walker, M.; Seidel, G. D.; Yuldasheva, N.; Tamarkin, L., Phase I and Pharmacokinetic Studies of CYT-6091, a Novel PEGylated Colloidal Gold-rhTNF Nanomedicine. *Clinical Cancer Research* **2010,** *16* (24), 6139.
89. Giljohann, D. A.; Seferos, D. S.; Daniel, W. L.; Massich, M. D.; Patel, P. C.; Mirkin, C. A., Gold Nanoparticles for Biology and Medicine. *Angewandte Chemie International Edition* **2010,** *49* (19), 3280-3294.
90. Ghosh, P.; Han, G.; De, M.; Kim, C. K.; Rotello, V. M., Gold nanoparticles in delivery applications. *Advanced Drug Delivery Reviews* **2008,** *60* (11), 1307-1315.
91. Xia, Y.; Li, W.; Cobley, C. M.; Chen, J.; Xia, X.; Zhang, Q.; Yang, M.; Cho, E. C.; Brown, P. K., Gold Nanocages: From Synthesis to Theranostic Applications. *Accounts of Chemical Research* **2011,** *44* (10), 914-924.
92. Chakraborty, I.; Mahata, S.; Mitra, A.; De, G.; Pradeep, T., Controlled synthesis and characterization of the elusive thiolated Ag55 cluster. *Dalton Transactions* **2014,** *43* (48), 17904-17907.
93. Henglein, A.; Giersig, M., Formation of Colloidal Silver Nanoparticles: Capping Action of Citrate. *The Journal of Physical Chemistry B* **1999,** *103* (44), 9533-9539.
94. Peyser, L. A.; Vinson, A. E.; Bartko, A. P.; Dickson, R. M., Photoactivated Fluorescence from Individual Silver Nanoclusters. *Science* **2001,** *291* (5501), 103-106.
95. Zheng, K.; Yuan, X.; Xie, J., Effect of ligand structure on the size control of mono- and bi-thiolate-protected silver nanoclusters. *Chemical Communications* **2017,** *53* (70), 9697-9700.
96. Joshi, C. P.; Bootharaju, M. S.; Alhilaly, M. J.; Bakr, O. M., [Ag25(SR)18]−: The "Golden" Silver Nanoparticle. *Journal of the American Chemical Society* **2015,** *137* (36), 11578-11581.
97. Yang, H.; Yan, J.; Wang, Y.; Su, H.; Gell, L.; Zhao, X.; Xu, C.; Teo, B. K.; Häkkinen, H.; Zheng, N., Embryonic Growth of Face-Center-Cubic Silver Nanoclusters Shaped in Nearly Perfect Half-Cubes and Cubes. *Journal of the American Chemical Society* **2017,** *139* (1), 31-34.
98. Chernousova, S.; Epple, M., Silver as Antibacterial Agent: Ion, Nanoparticle, and Metal. *Angewandte Chemie International Edition* **2013,** *52* (6), 1636-1653.
99. Chaloupka, K.; Malam, Y.; Seifalian, A. M., Nanosilver as a new generation of nanoproduct in biomedical applications. *Trends in Biotechnology* **2010,** *28* (11), 580-588.
100. Quadros, M. E.; Marr, L. C., Silver Nanoparticles and Total Aerosols Emitted by Nanotechnology-Related Consumer Spray Products. *Environmental Science & Technology* **2011,** *45* (24), 10713-10719.

101. Ehdaie, B.; Krause, C.; Smith, J. A., Porous Ceramic Tablet Embedded with Silver Nanopatches for Low-Cost Point-of-Use Water Purification. *Environmental Science & Technology* **2014,** *48* (23), 13901-13908.
102. Zheng, K.; Yuan, X.; Goswami, N.; Zhang, Q.; Xie, J., Recent advances in the synthesis, characterization, and biomedical applications of ultrasmall thiolated silver nanoclusters. *RSC Advances* **2014,** *4* (105), 60581-60596.
103. Zheng, K.; Setyawati, M. I.; Lim, T.-P.; Leong, D. T.; Xie, J., Antimicrobial Cluster Bombs: Silver Nanoclusters Packed with Daptomycin. *ACS Nano* **2016,** *10* (8), 7934-7942.
104. Yang, S. W.; Vosch, T., Rapid Detection of MicroRNA by a Silver Nanocluster DNA Probe. *Analytical Chemistry* **2011,** *83* (18), 6935-6939.
105. Murray, R. W., Nanoelectrochemistry: Metal Nanoparticles, Nanoelectrodes, and Nanopores. *Chem. Rev.* **2008,** *108* (7), 2688-2720.
106. Antonello, S.; Perera, N. V.; Ruzzi, M.; Gascon, J. A.; Maran, F., Interplay of Charge State, Lability, and Magnetism in the Molecule-like Au-25(SR)(18) Cluster. *J. Am. Chem. Soc.* **2013,** *135* (41), 15585-15594.
107. Parker, J. F.; Fields-Zinna, C. A.; Murray, R. W., The Story of a Monodisperse Gold Nanoparticle: Au25L18. *Accounts of Chemical Research* **2010,** *43* (9), 1289-1296.
108. Jin, R., Quantum sized, thiolate-protected gold nanoclusters. *Nanoscale* **2010,** *2* (3), 343-62.
109. Zhou, C.; Yang, S.; Liu, J.; Yu, M.; Zheng, J., Luminescent gold nanoparticles: A new class of nanoprobes for biomedical imaging. *Experimental Biology and Medicine* **2013,** *238* (11), 1199-1209.
110. Walter, M.; Akola, J.; Lopez-Acevedo, O.; Jadzinsky, P. D.; Calero, G.; Ackerson, C. J.; Whetten, R. L.; Gronbeck, H.; Hakkinen, H., A unified view of ligand-protected gold clusters as superatom complexes. *Proceedings of the National Academy of Sciences of the United States of America* **2008,** *105* (27), 9157-62.
111. Crisostomo, D.; Greene, R. R.; Cliffel, D. E., Effect of Ligand Charge on Electron-Transfer Rates of Water-Soluble Gold Nanoparticles. *The Journal of Physical Chemistry C* **2015,** *119* (21), 11296-11300.
112. Brust, M.; Walker, M.; Bethell, D.; Schiffrin, D. J.; Whyman, R., Synthesis of Thiol-Derivatized Gold Nanoparticles in a 2-Phase Liquid-Liquid System. *Journal of the Chemical Society-Chemical Communications* **1994,** (7), 801-802.
113. Weber, W. P.; Gokel, G. W., Phase transfer catalysis. Part I: General principles. *Journal of Chemical Education* **1978,** *55* (6), 350.
114. Yuan, X.; Luo, Z.; Zhang, Q.; Zhang, X.; Zheng, Y.; Lee, J. Y.; Xie, J., Synthesis of Highly Fluorescent Metal (Ag, Au, Pt, and Cu) Nanoclusters by Electrostatically Induced Reversible Phase Transfer. *ACS Nano* **2011,** *5* (11), 8800-8808.
115. Lee, D.; Donkers, R. L.; Wang, G.; Harper, A. S.; Murray, R. W., Electrochemistry and Optical Absorbance and Luminescence of Molecule-like Au38 Nanoparticles. *J. Am. Chem. Soc.* **2004,** *126* (19), 6193-6199.
116. Wang, G.; Guo, R.; Kalyuzhny, G.; Choi, J.-P.; Murray, R. W., NIR Luminescence Intensities Increase Linearly with Proportion of Polar Thiolate Ligands in Protecting Monolayers of Au38 and Au140 Quantum Dots. *The Journal of Physical Chemistry B* **2006,** *110* (41), 20282-20289.
117. Wu, Z.; Suhan, J.; Jin, R., One-pot synthesis of atomically monodisperse, thiol-functionalized Au25 nanoclusters. *Journal of Materials Chemistry* **2009,** *19* (5), 622-626.

118. Zhu, M.; Lanni, E.; Garg, N.; Bier, M. E.; Jin, R., Kinetically Controlled, High-Yield Synthesis of Au25 Clusters. *Journal of the American Chemical Society* **2008,** *130* (4), 1138-1139.
119. Devadas, M. S.; Kim, J.; Sinn, E.; Lee, D.; Goodson, T.; Ramakrishna, G., Unique Ultrafast Visible Luminescence in Monolayer-Protected Au25 Clusters. *The Journal of Physical Chemistry C* **2010,** *114* (51), 22417-22423.
120. Zhu, M.; Aikens, C. M.; Hollander, F. J.; Schatz, G. C.; Jin, R., Correlating the Crystal Structure of A Thiol-Protected Au25 Cluster and Optical Properties. *J. Am. Chem. Soc.* **2008,** *130* (18), 5883-5885.
121. Huang, T.; Murray, R. W., Luminescence of Tiopronin Monolayer-Protected Silver Clusters Changes To That of Gold Clusters upon Galvanic Core Metal Exchange. *J. Phys. Chem. B* **2003,** *107* (30), 7434-7440.
122. Chakraborty, I.; Pradeep, T., Atomically Precise Clusters of Noble Metals: Emerging Link between Atoms and Nanoparticles. *Chem. Rev.* **2017,** *117* (12), 8208-8271.
123. Zheng, J.; Zhou, C.; Yu, M.; Liu, J., Different sized luminescent gold nanoparticles. *Nanoscale* **2012,** *4* (14), 4073-4083.
124. Liu, J.; Yu, M.; Zhou, C.; Yang, S.; Ning, X.; Zheng, J., Passive Tumor Targeting of Renal-Clearable Luminescent Gold Nanoparticles: Long Tumor Retention and Fast Normal Tissue Clearance. *Journal of the American Chemical Society* **2013,** *135* (13), 4978-4981.
125. Jupally, V. R.; Dass, A., Synthesis of Au130(SR)50 and Au130-xAgx(SR)50 nanomolecules through core size conversion of larger metal clusters. *PCCP* **2014,** *16* (22), 10473-10479.
126. Negishi, Y.; Sakamoto, C.; Ohyama, T.; Tsukuda, T., Synthesis and the Origin of the Stability of Thiolate-Protected Au130 and Au187 Clusters. *The Journal of Physical Chemistry Letters* **2012,** *3* (12), 1624-1628.
127. Tang, Z.; Robinson, D. A.; Bokossa, N.; Xu, B.; Wang, S.; Wang, G., Mixed Dithiolate Durene-DT and Monothiolate Phenylethanethiolate Protected Au-130 Nanoparticles with Discrete Core and Core-Ligand Energy States. *J. Am. Chem. Soc.* **2011,** *133* (40), 16037-16044.
128. Link, S.; Beeby, A.; FitzGerald, S.; El-Sayed, M. A.; Schaaff, T. G.; Whetten, R. L., Visible to Infrared Luminescence from a 28-Atom Gold Cluster. *J. Phys. Chem. B* **2002,** *106* (13), 3410-3415.
129. Huang, T.; Murray, R. W., Visible Luminescence of Water-Soluble Monolayer-Protected Gold Clusters. *J. Phys. Chem. B* **2001,** *105* (50), 12498-12502.
130. Hesari, M.; Workentin, M. S.; Ding, Z., Highly Efficient Electrogenerated Chemiluminescence of Au38 Nanoclusters. *ACS Nano* **2014,** *8* (8), 8543-8553.
131. Hesari, M.; Workentin, M. S.; Ding, Z., NIR electrochemiluminescence from Au25-nanoclusters facilitated by highly oxidizing and reducing co-reactant radicals. *Chem. Sci.* **2014,** *5* (10), 3814-3822.
132. Swanick, K. N.; Hesari, M.; Workentin, M. S.; Ding, Z., Interrogating near-infrared electrogenerated chemiluminescence of Au25(SC2H4Ph)18(+) clusters. *J. Am. Chem. Soc.* **2012,** *134* (37), 15205-8.
133. Mustalahti, S.; Myllyperkiö, P.; Lahtinen, T.; Malola, S.; Salorinne, K.; Tero, T.-R.; Koivisto, J.; Häkkinen, H.; Pettersson, M., Photodynamics of a Molecular Water-Soluble Nanocluster Identified as Au130(pMBA)50. *J. Phys. Chem. C* **2015,** *119* (34), 20224-20229.

134. Yi, C.; Zheng, H.; Tvedte, L. M.; Ackerson, C. J.; Knappenberger, K. L., Nanometals: Identifying the Onset of Metallic Relaxation Dynamics in Monolayer-Protected Gold Clusters Using Femtosecond Spectroscopy. *J. Phys. Chem. C* **2015,** *119* (11), 6307-6313.
135. Zhou, M.; Zeng, C.; Chen, Y.; Zhao, S.; Sfeir, M. Y.; Zhu, M.; Jin, R., Evolution from the plasmon to exciton state in ligand-protected atomically precise gold nanoparticles. *Nature Comunications* **2016,** *7*, 13240.
136. Venzo, A.; Antonello, S.; Gascon, J. A.; Guryanov, I.; Leapman, R. D.; Perera, N. V.; Sousa, A.; Zamuner, M.; Zanella, A.; Maran, F., Effect of the Charge State (z =-1, 0,+1) on the Nuclear Magnetic Resonance of Monodisperse Au-25 S(CH2)(2)Ph (18)(z) Clusters. *Anal. Chem.* **2011,** *83* (16), 6355-6362.
137. Green, T. D.; Knappenberger, K. L., Relaxation dynamics of Au25L18 nanoclusters studied by femtosecond time-resolved near infrared transient absorption spectroscopy. *Nanoscale* **2012,** *4* (14), 4111-4118.
138. Yi, C.; Tofanelli, M. A.; Ackerson, C. J.; Knappenberger, K. L., Optical Properties and Electronic Energy Relaxation of Metallic Au144(SR)60 Nanoclusters. *Journal of the American Chemical Society* **2013,** *135* (48), 18222-18228.
139. Zhou, M.; Qian, H.; Sfeir, M. Y.; Nobusada, K.; Jin, R., Effects of single atom doping on the ultrafast electron dynamics of M1Au24(SR)18 (M = Pd, Pt) nanoclusters. *Nanoscale* **2016,** *8* (13), 7163-71.
140. Hodak, J. H.; Henglein, A.; Hartland, G. V., Electron-phonon coupling dynamics in very small (between 2 and 8 nm diameter) Au nanoparticles. *The Journal of Chemical Physics* **2000,** *112* (13), 5942-5947.
141. Hartland, G. V., Optical Studies of Dynamics in Noble Metal Nanostructures. *Chemical Reviews* **2011,** *111* (6), 3858-3887.
142. Zeng, C.; Chen, Y.; Kirschbaum, K.; Appavoo, K.; Sfeir, M. Y.; Jin, R., Structural patterns at all scales in a nonmetallic chiral Au(133)(SR)(52) nanoparticle. *Sci Adv* **2015,** *1* (2).
143. Thanthirige, V. D.; Kim, M.; Choi, W.; Kwak, K.; Lee, D.; Ramakrishna, G., Temperature-Dependent Absorption and Ultrafast Exciton Relaxation Dynamics in MAu24(SR)18 Clusters (M = Pt, Hg): Role of the Central Metal Atom. *J. Phys. Chem. C* **2016,** *120* (40), 23180-23188.
144. Li, Y.; Zaluzhna, O.; Xu, B.; Gao, Y.; Modest, J. M.; Tong, Y. J., Mechanistic Insights into the Brust−Schiffrin Two-Phase Synthesis of Organo-chalcogenate-Protected Metal Nanoparticles. *Journal of the American Chemical Society* **2011,** *133* (7), 2092-2095.
145. Senanayake, R. D.; Akimov, A. V.; Aikens, C. M., Theoretical Investigation of Electron and Nuclear Dynamics in the [Au25(SH)18]−1 Thiolate-Protected Gold Nanocluster. *J. Phys. Chem. C* **2017,** *121* (20), 10653-10662.
146. Padelford, J. W.; Wang, T.; Wang, G., Enabling Better Electrochemical Activity Studies of H2O-Soluble Au Clusters by Phase Transfer and a Case Study of Lipoic-Acid-Stabilized Au22. *ChemElectroChem* **2016,** *3* (8), 1201-1205.
147. Anker, J. N.; Hall, W. P.; Lyandres, O.; Shah, N. C.; Zhao, J.; Van Duyne, R. P., Biosensing with plasmonic nanosensors. *Nature Materials* **2008,** *7*, 442.
148. Hu, M.; Chen, J.; Li, Z.-Y.; Au, L.; Hartland, G. V.; Li, X.; Marquez, M.; Xia, Y., Gold nanostructures: engineering their plasmonic properties for biomedical applications. *Chemical Society Reviews* **2006,** *35* (11), 1084-1094.

149. Lin, S.-Y.; Chen, N.-T.; Sum, S.-P.; Lo, L.-W.; Yang, C.-S., Ligand exchanged photoluminescentgold quantum dots functionalized with leading peptides for nuclear targeting and intracellular imaging. *Chemical Communications* **2008,** (39), 4762-4764.
150. Shang, L.; Yang, L.; Stockmar, F.; Popescu, R.; Trouillet, V.; Bruns, M.; Gerthsen, D.; Nienhaus, G. U., Microwave-assisted rapid synthesis of luminescent gold nanoclusters for sensing Hg2+ in living cells using fluorescence imaging. *Nanoscale* **2012,** *4* (14), 4155-4160.
151. Yu, M.; Zheng, J., Clearance Pathways and Tumor Targeting of Imaging Nanoparticles. *ACS Nano* **2015,** *9* (7), 6655-6674.
152. Zhu, M.; Aikens, C. M.; Hollander, F. J.; Schatz, G. C.; Jin, R., Correlating the Crystal Structure of A Thiol-Protected Au25 Cluster and Optical Properties. *Journal of the American Chemical Society* **2008,** *130* (18), 5883-5885.
153. Tsoli, M.; Kuhn, H.; Brandau, W.; Esche, H.; Schmid, G., Cellular Uptake and Toxicity of Au55 Clusters. *Small* **2005,** *1* (8-9), 841-844.
154. Wang, J.; Koo, Y.; Alexander, A.; Yang, Y.; Westerhof, S.; Zhang, Q.; Schnoor, J. L.; Colvin, V. L.; Braam, J.; Alvarez, P. J. J., Phytostimulation of Poplars and Arabidopsis Exposed to Silver Nanoparticles and Ag+ at Sublethal Concentrations. *Environmental Science & Technology* **2013,** *47* (10), 5442-5449.
155. Cathcart, N.; Kitaev, V., Silver Nanoclusters: Single-Stage Scaleable Synthesis of Monodisperse Species and Their Chirooptical Properties. *The Journal of Physical Chemistry C* **2010,** *114* (38), 16010-16017.
156. Osborne, O. J.; Lin, S.; Chang, C. H.; Ji, Z.; Yu, X.; Wang, X.; Lin, S.; Xia, T.; Nel, A. E., Organ-Specific and Size-Dependent Ag Nanoparticle Toxicity in Gills and Intestines of Adult Zebrafish. *ACS Nano* **2015,** *9* (10), 9573-9584.
157. Wang, J.; Wang, W.-X., Low Bioavailability of Silver Nanoparticles Presents Trophic Toxicity to Marine Medaka (Oryzias melastigma). *Environmental Science & Technology* **2014,** *48* (14), 8152-8161.
158. Bakr, O. M.; Amendola, V.; Aikens, C. M.; Wenseleers, W.; Li, R.; Dal Negro, L.; Schatz, G. C.; Stellacci, F., Silver Nanoparticles with Broad Multiband Linear Optical Absorption. *Angewandte Chemie International Edition* **2009,** *48* (32), 5921-5926.
159. Chakraborty, I.; Govindarajan, A.; Erusappan, J.; Ghosh, A.; Pradeep, T.; Yoon, B.; Whetten, R. L.; Landman, U., The Superstable 25 kDa Monolayer Protected Silver Nanoparticle: Measurements and Interpretation as an Icosahedral Ag152(SCH2CH2Ph)60 Cluster. *Nano Letters* **2012,** *12* (11), 5861-5866.
160. Harkness, K. M.; Tang, Y.; Dass, A.; Pan, J.; Kothalawala, N.; Reddy, V. J.; Cliffel, D. E.; Demeler, B.; Stellacci, F.; Bakr, O. M.; McLean, J. A., Ag44(SR)304−: a silver–thiolate superatom complex. *Nanoscale* **2012,** *4* (14), 4269-4274.
161. Desireddy, A.; Conn, B. E.; Guo, J.; Yoon, B.; Barnett, R. N.; Monahan, B. M.; Kirschbaum, K.; Griffith, W. P.; Whetten, R. L.; Landman, U.; Bigioni, T. P., Ultrastable silver nanoparticles. *Nature* **2013,** *501* (7467), 399-402.
162. Liu, C.; Li, T.; Abroshan, H.; Li, Z.; Zhang, C.; Kim, H. J.; Li, G.; Jin, R., Chiral Ag23 nanocluster with open shell electronic structure and helical face-centered cubic framework. *Nature Communications* **2018,** *9* (1), 744.
163. Song, Y.; Lambright, K.; Zhou, M.; Kirschbaum, K.; Xiang, J.; Xia, A.; Zhu, M.; Jin, R., Large-Scale Synthesis, Crystal Structure, and Optical Properties of the Ag146Br2(SR)80 Nanocluster. *ACS Nano* **2018,** *12* (9), 9318-9325.